UNIVERSIDADE DE LISBOA
FACULDADE DE CIÊNCIAS

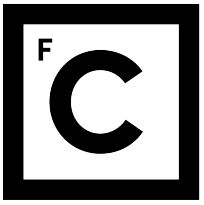

Ciências
ULisboa

Dynamics of mixtures under confinement

"Documento Definitivo"

Doutoramento em Física

André S. Nunes

Tese orientada por:
Nuno Araújo e Margarida Telo da Gama

Documento especialmente elaborado para a obtenção do grau de doutor

2019

UNIVERSIDADE DE LISBOA
FACULDADE DE CIÊNCIAS

Dynamics of mixtures under confinement

Doutoramento em Física

André S. Nunes

Tese orientada por:
Nuno Araújo e Margarida Telo da Gama

Júri:

Presidente: Doutor José Manuel de Nunes Vicente Rebordão, Investigador Coordenador e Presidente do Departamento de Física da Faculdade de Ciências da Universidade de Lisboa

Vogais: Doutor Holger Stark, Professor, Faculty II – Mathematics and Natural Sciences da Technische Universität Berlin (Alemanha)

Doutor Hartmut Löwen, Professor, Faculty of Mathematics and Natural Sciences da Heinrich Heine Universität Düsselfdorf (Alemanha)

Doutor Ana Maria Ribeiro Ferreira Nunes, Professora Associada com Agregação, Faculdade de Ciências da Universidade de Lisboa

Doutor Nuno Miguel Azevedo Machado de Araújo, Professor Auxiliar com Agregação, Faculdade de Ciências da Universidade de Lisboa (orientador)

Documento especialmente elaborado para a obtenção do grau de doutor

SFRH/BD/119240/2016, PTDC/FIS-MAC/28146/2017 (LISBOA-01-0145-FEDER-028146)
COST-ACTION-MP1305 and UID/FIS/00618/2019

2019

Acknowledgements

I would like to thank my supervisors Nuno Araújo and Margarida Telo da Gama for their energetic guidance and decisive support over the years. I would also like to thank Akshat Gupta and Vasco Braz for the work we did together. Some of the results presented here were only made possible because of their efforts. I also acknowledge Sabareesh Velu, Iryna Kasianiuk, Denys Kasyanyuk, Agnese Callegari, Giorgio Volpe and Giovanni Volpe, all outstanding researchers with whom I had the pleasure to collaborate with. The experimental results presented in this thesis are a product of their work.

Giovanni Volpe invited me to visit is group in Gothenburg University for which I am very grateful. It certainly helped decrease the gap between theory and experiments. I also acknowledge fruitful discussions with Daniel de las Heras during the visit to his group in Bayreuth University and other ocasions.

I would like to thank all the members of CFTC for the fruitful discussions during the weekly group meetings and long lunches that helped improve the content of this thesis (the first more than the latter).

I also acknowledge financial support from the Portuguese Foundation for Science and Technology (FCT) under Contracts nos. SFRH/BD/119240/2016, PTDC/FIS-MAC/28146/2017 (LISBOA-01-0145-FEDER-028146) and UID/FIS/00618/2019 and the COST Action MP1305.

Abstract

We study the self-organization of mixtures of colloidal particles in the presence of external fields and explore design strategies to obtain targeted structures. We consider two types of binary mixtures. In the first, the particles differ in their Stokes coefficient and in the second, the particles differ in their response to external fields. While for the first type the thermodynamic equilibrium state is completely mixed, for the second one, segregation is expected at equilibrium. Both types are characterized by having a complex energy landscape and, as a result, during the collective dynamics the systems get frequently trapped in local minima for long periods of time and so they rarely reach thermodynamic equilibrium within the timescale of relevance. The specific state in which the systems are kinetically arrested will depend strongly on the history. Thus, in order to properly simulate and characterize the dynamics of these systems, we need new methods and techniques. We employ particle based simulations such as Brownian Dynamics (BD) to probe the time evolution of the systems and Monte Carlo (MC) simulations to study the properties of the equilibrium states. We also use continuum models, including dynamical density functional theory of fluids (DDFT), to access long time scales that are not reachable with direct numerical simulations. We report the behavior in the presence of different spatially dependent external fields. We also show how mixtures of the first type can segregate while they are sedimenting under gravity. Finally, we propose a way to control the number of structural defects in crystals using random potentials in mixtures of the second type. Implications of our findings in the field of Soft Condensed Matter Physics are also discussed.

KEYWORDS:

Colloidal mixtures, Brownian dynamics, Dynamical demixing, Field-driven self-organization.

Resumo

Nesta tese estudamos a dinâmica da auto-organização em misturas binárias de partículas coloidais na presença de campos externos e exploramos estratégias para obter as estruturas com as características pretendidas. Ao identificarmos mecanismos chave, somos capazes de desenvolver modelos que não dependem dos detalhes particulares das interações e obter métodos robustos que permitem controlar a formação de estruturas com as propriedades desejadas. Estamos particularmente interessados na segregação das espécies e na capacidade de formar estruturas em que o número de defeitos estruturais pode ser controlado.

Os nossos modelos são construídos com princípios gerais e simples mas são capazes de descrever a física relevante. Tomando partido de colaborações com grupos que realizam experiências, fomos capazes de validar os modelos e testar as nossas previsões. Os modelos teóricos podem ser utilizados em experiências de duas formas diferentes: por um lado, estes modelos são convenientes para explorar o espaço de parâmetros de uma forma rápida e pouco dispendiosa, por outro lado, podem ser usados para descrever os graus de liberdade mesoscópicos, que raramente são acessíveis no laboratório.

É conhecido que sistemas com muitos corpos têm um comportamento emergente que tem origem nas interações entre os seus constituintes. Diferentes estudos teóricos e experimentais sugerem que os fenómenos observados a diferentes escalas dependem muito mais do arranjo espacial dos constituintes do que dos detalhes das interações. Isto introduz correlações que não estão presentes em gases ideais, o que representa um grande desafio do ponto de vista do tratamento numérico e analítico. Não é possível fazer simulações com todos os graus de liberdade presentes no sistema físico e torna-se necessário desenvolver modelos "coarse grained" para se conseguir estudar a física relevante no sistema.

Uma vantagem do estudo de sistemas coloidais é o facto de, em condições ideais, os colóides poderem rearranjar-se colectivamente de uma forma espontânea, dando origem a estruturas mesoscópicas. Em vez da obtenção de estruturas do modo em que tradicionalmente se constrói uma casa, com a manipulação cuidada de cada um dos elementos (top-down), grupos

de partículas são arranjados colectivamente (bottom-up). Este processo é referido como self-assembly e tem atraído muita atenção ao longo dos anos. Em particular a segregação espontânea de misturas pode ocorrer em diferentes cenários. Este efeito é importante, por exemplo, no fabrico de filtros, em que o objectivo é isolar componentes da mistura, em separação de amostras em aparelhos de microfluídica ou em métodos de diagnóstico de doenças. Outras vezes, é importante compreender os mecanismos por de trás da segregação para que se consiga diminuir a sua presença na amostra tanto quanto possível. Tal é o caso da indústria farmacêuta, onde é importante produzir grandes quantidades de fluidos ou pós com composição química uniforme.

Enquanto sistemas monodispersos já exibem diagramas de fases em equilíbrio bastante ricos, ao introduzir vários tipos de partículas, aumentamos significativamente o número de fases de equilíbrio. Mais importante ainda, como veremos mais adiante, o estado final do sistema torna-se mais dependente dos processos cinéticos. A paisagem energética é complexa, com muitas configurações de energia muito semelhante e, de facto, o sistema pode ficar preso em mínimos locais que não correspondem ao estado de equilíbrio. O tempo de equilibração diverge e o sistema diz-se estar cineticamente preso. Por este motivo, modelos focados em propriedades de equilíbrio não são suficientes para fornecer uma descrição completa e precisamos ter em conta a dinâmica.

A rica dinâmica dirigida por campos externos envolve vários mecanismos em diferentes escalas de comprimento. Por um lado, temos as interações partícula/fluido, partícula/partícula e partícula/campo, que dependem das propriedades coloidais, como forma e carga. Por outro lado, correlações de muitos corpos levam à formação de estruturas mesoscópicas, muito maiores que o tamanho da partícula individual, e tornam-se as unidades relevantes para a dinâmica. Diferentes mecanismos à microescala podem levar a diferentes resultados à mesoescala. Nesta tese, consideramos dois tipos de misturas binárias em que a assimetria entre as espécies é consequência de diferentes mecanismos à microescala. No primeiro tipo de sistema, as interações partícula/fluido são diferentes para as duas espécies. Isso reflete-se num coeficiente de atrito de Stokes que é distinto para cada espécie, levando a diferentes raios hidrodinâmicos. Esta assimetria leva a diferentes (hidro)dinâmicas, mas o estado de equilíbrio é o mesmo para ambas as espécies e, portanto, chamamos as espécies "fast" e "slow" se elas tiverem um coeficiente de atrito de Stokes menor ou maior, respectivamente. No segundo tipo de sistema, as interações partícula/campo diferem para cada espécie. Neste caso, a dinâmica é diferente e as propriedades de equilíbrio também são diferentes. Chamamos-lhes de "strong" e "weak" se as partículas tiverem forte ou fraca força de interação com o campo externo, respectivamente.

Além das assimetrias entre as espécies que acabamos de descrever, as partículas são idênticas (por exemplo, tamanho, forma, ...). Estamos interessados em estudar como a dinâmica depende dos coeficientes de Stokes e da intensidade da resposta a um campo externo.

No capítulo 1 desta tese, fazemos uma introdução ao trabalho e declaramos os nossos objectivos, o impacto dos nossos resultados e a motivação deste estudo. No capítulo 2, apresentamos alguns dos métodos numéricos e analíticos usados nesta tese. Começamos com a Brownian Dynamics (BD), usada para simular a dinâmica dos sistemas coloidais, seguida de uma breve explicação dos métodos de Monte Carlo (MC) que foram usados para encontrar estados de equilíbrio. Também utilizamos a Dynamic Density Functional Theory of fluids (DDFT) para comparar os resultados das simulações com uma descrição analítica e identificar o papel dos vários mecanismos em jogo. Finalmente, propomos um algoritmo para produzir paisagens aleatórias de energia com base no Fourier filtering method (FFM).

Nos capítulos seguintes, apresentamos o nosso trabalho de pesquisa. Nos capítulos 3 e 4, estudamos o sistema no qual as partículas têm diferentes coeficientes de Stokes. Quando as partículas se estão a mover devido à ação de potenciais externos, viajam com velocidades diferentes. No capítulo 3, estudamos estratégias para obter segregação dinâmica num sistema que está misturado em equilíbrio. No capítulo 4, estudamos a sedimentação de partículas coloidais num campo gravitacional e medimos a segregação no sistema e os aglomerados de partículas encontrados no depósito. A assimetria entre os coeficientes de Stokes implica que as interações com o fluido são diferentes para ambas as espécies. Além desse coeficiente, não consideramos outras interações hidrodinâmicas, o que torna este modelo bastante irrealista. Contudo, percebemos que o papel da hidrodinâmica não é o principal mecanismo que distingue espécies diferentes. Num esforço para avançar na direção de um cenário mais realista que pode ser realizado em experiências, propomos, nos capítulos 5 e 6, um sistema em que as partículas respondem com diferentes intensidades ao potencial externo. O custo é que, nesses sistemas, a segregação das espécies é o estado de equilíbrio e deixa de ser um efeito puramente dinâmico. No capítulo 5, estudamos um sistema completamente segregado em equilíbrio, mas a dinâmica leva consistentemente a estados cineticamente presos, com defeitos de composição e, em menor grau, defeitos estruturais. Desenvolvemos ainda um protocolo capaz de conduzir o sistema ao estado de equilíbrio.

Um dos objetivos desta tese é fazer previsões teóricas que possam ser testadas em experiências. No capítulo 5, apresentamos experiências preliminares que mostram uma boa concordância

qualitativa com a teoria, mas devido a desafios no desenvolvimento da configuração experimental, não fomos capazes de fazer uma comparação detalhada até ao momento da redação. Uma colaboração bem sucedida entre teoria e experiência é mostrada no capítulo 6, onde usamos campos aleatórios em vez dos campos bem definidos, como os que foram considerados nos capítulos anteriores.

PALAVRAS-CHAVE:

Misturas de coloides, Dinâmica Browniana, Segregação dinâmica, Auto-organização dirigida por campos externos.

Contents

List of Figures

List of Tables

List of acronyms

BD	Brownian Dynamics
MC	Monte Carlo
DFT	Density Functional Theory
DDFT	Dynamical Density Functional Theory
FFM	Fourier Filtering Method
LDA	Local Density Approximation

Chapter 1

Introduction

1.1 Objectives

We aim to study non-equilibrium self-organized patterns emerging from the *collective dynamics of colloidal mixtures in the presence of external fields*. By identifying the *key mechanisms* we are able to *develop models* that do not depend on the fine details of the interactions and obtain robust methods to control the formation of structures with the desired properties. We are specially interested in the demixing of species and the ability to assemble structures with a controlled number of structural defects.

1.2 Impact

Our models are built on *general (simple) features and are able to grasp the relevant physics*. Profiting from ongoing collaborations with groups performing experiments, we managed to successfully validate the models and test predictions. The theoretical models can be used to guide the experiments in two ways: on one hand, they are convenient to explore the parameter space in a quick and inexpensive fashion, on the other hand, they can be used to describe mesoscopic degrees of freedom, that are rarely accessible in the lab.

1.3 Motivation

Many body systems are known to display emergent behavior that stems from the collective interplay between their interacting constituents [1, 2]. This is manifested at different scales such as, e.g., turbulence in fluids [3, 4], where the fluid particles interact at the atomic/molecular

scale, and crowd turbulence of pedestrians where the relevant interactions occur at a length and time scales that are several orders of magnitude larger [5]. Different theoretical and experimental studies suggest that, the observed phenomena at different scales depend much more on the spatial arrangement of the different constituents rather than on the details of the interactions. This introduces non-linear processes that are not present in ideal gases and are a big challenge to treat both analytically and numerically [6, 7]. It is not possible to perform detailed simulations describing all the degrees of freedom present in the physical system and the development of coarse grained models that are able to grasp the relevant physics is a necessity and a challenge. An advantage for practitioners in colloidal systems is that, given the right conditions, colloids can collectively rearrange in a spontaneous way to form structures and patterns. Instead of obtaining structures in the way we would traditionally build a house, with careful manipulation of individual elements (top-down approach), groups of particles are assembled spontaneously (bottom-up). This process is referred to as self-assembly and it has been attracting much attention over the years. The main goal is to engineer structures at small scales efficiently [8–13]. In particular, spontaneous segregation in mixtures of particles can occur in different scenarios. For instance, if the energy of interaction with a particle from different species is higher than with one of the same species the system is expected to segregate at low temperatures, and the final equilibrium state is completely demixed [14, 15]. Another case where we find segregation at equilibrium is when the particles have different responses to a space dependent external field and there are regions to which they are selectively attracted [16]. However, external fields can also be used to drive the system far-from-equilibrium and cause, under the right conditions, dynamical demixing in the stationary state. Such is the case of laning that occurs in systems of particles traveling in opposite directions [17, 18]. The fields that drive the system to segregate can be made to change in time by using, for example, periodically vibrating fields [19]. There are also systems where the segregation is induced by the hydrodynamics of the fluid [20].
The topic of segregation in mixtures has many important applications. For example, segregation is used in filters where the goal is to isolate one or more components from the mixture [21–23] and in sample separation in microfluidic devices that can be used as a methods for diagnosis of diseases [24, 25]. In other cases, it is important to understand the mechanisms behind segregation to hinder the demixing of the sample. Such is the case in the pharmaceutical industry where it is important to produce large amounts of fluids or powders with uniformly distributed chemical composition [26, 27]. At the biological level, it was found that the red cells flow close to the axis of blood vessels while the other microparticles are transported near the walls [28, 29]. While monodispersed systems already display rich phase diagrams at equilibrium [30, 31], by

introducing several particle types we increase the number of equilibrium phases quite significantly [32, 33]. More importantly, as we will see later, the final state of the system becomes more dependent on the kinetic processes. The energy landscape is complex, with many configurations of very similar energy and, in fact, the system may get trapped in a local minimum instead of exploring the configurational space as expected for equilibrium. The equilibration time diverges and the system is said to be kinetically trapped. For this reason, models focused on equilibrium properties are not sufficient to provide a complete description and we need to account for the dynamics.

Colloidal systems are ideal models to study collective phenomena. They are composed by a solvent that we take to be a fluid (e.g. water) and a solute that we consider to be solid particles that are several orders of magnitude greater than the molecules of the fluid (10^4) which means they are at the micrometer scale. These length-scales are above the optical diffraction limit which allows the direct observation of particles under an optical microscope. In addition, this scale is large enough to render quantum effects unimportant, which simplifies the problem. Another important scale is the energy-scale. In the colloidal range, thermal fluctuations of the particles due to the interactions with the molecules of the solvent are relevant and particles are diffusing. Thus, the temperature is an important parameter that determines the thermodynamic equilibrium state. These fluctuations represent a challenge that we need to face while developing our models. Colloids are also highly responsive to external perturbations and we can tune them to assemble different phases or alter the dynamics. Finally, the time-scale a particle takes to diffuse in the region equivalent to its volume (also referred to as Brownian time) is of the order of one second and the time it takes to form mesoscopic structures is of the order of minutes or even hours [34]. This is a consequence from the fact that colloidal systems are usually in the overdamped regime. They are in the limit of low Reynolds number where the viscosity of the fluid is high and the product between the Stokes friction coefficient and the Brownian time is larger than the mass of the particles. It is then safe to neglect the inertial forces at time-scales larger than the Brownian time and the motion of the particles is highly dissipative due to the drag imposed by the fluid. Thus, we are able to track the trajectories of individual particles in the laboratory, which is very useful as the dynamics is a topic of interest.

The field driven dynamics involves several mechanisms at different length scales. On one hand, one has the particle/fluid, particle/particle, and particle/field interactions, which depend on the colloidal properties such as shape and charge. On the other hand, many-body correlations lead to the formation of mesoscopic structures, much larger than the individual particle size, which become the relevant units for the dynamics. Different mechanisms at the microscale can lead

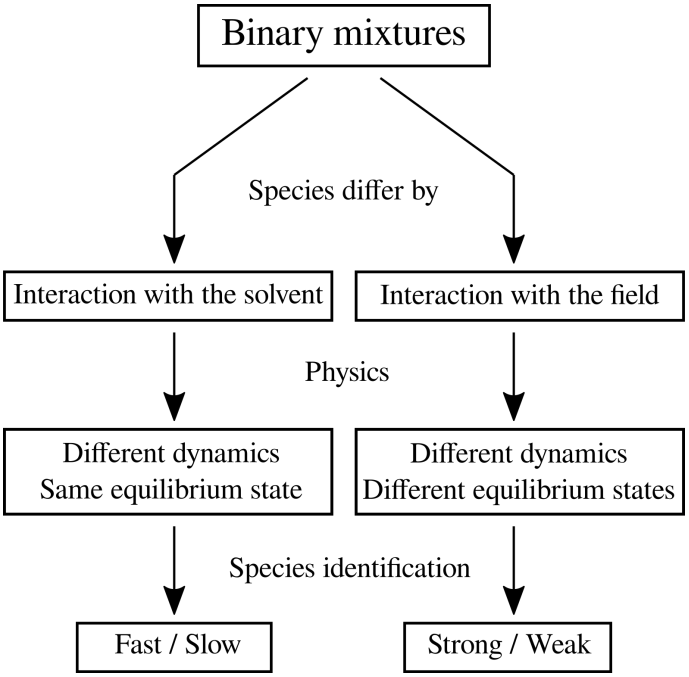

FIGURE 1.1: Scheme displaying the differences between the two types of systems considered in this thesis.

to different outcomes at the mesoscale. In this thesis, we consider two types of binary mixtures where the asymmetry between the species stems from different mechanisms at the microscale (see Fig. 1.1). In the first type of system, the particle/fluid interactions are different for the two species. This is reflected in their Stokes friction coefficient that is distinct for each species, leading to different hydrodynamic radii. This asymmetry leads to different (hydro)dynamics but the equilibrium state is the same for both species, and thus we name them fast and slow if they have a lower or higher Stokes friction coefficient, respectively. In the second type of system, the particle/field interactions differ for each species. In this case, they have different dynamics and different equilibrium properties. We name them strong and weak if they have a high or low strength of interaction with the external field, respectively. Other than the asymmetries between the species that were just described, the particles are identical (e.g. size, shape...). We are interested in studying how the dynamics depend on the Stokes coefficients and on the strength of the response to an external field.

In chapter 2, we introduce some of the numerical and analytical methods used in this thesis. We start with Brownian Dynamics (BD) used to simulate the dynamics of colloidal systems, followed by a brief explanation of Monte Carlo methods (MC) that were used to find equilibrium states. We also used Dynamic-Density Functional Theory of fluids (DDFT) to compare the results from simulations with an analytical description and identify the role of the various

mechanisms at play. Finally, we introduce the algorithm that we proposed to produce random energy landscapes based on the Fourier Filtering Method (FFM), which was used successfully in the experiments that followed, described in detail in chapter 6.

In the following chapters we present our research work. In chapters 3 and 4, we study the system in which particles have different Stokes coefficients [13, 35]. When particles are moving due to the action of external potentials, they travel at different speeds. In chapter 3, we study strategies to achieve dynamical segregation in a system that is mixed at equilibrium. In chapter 4, we study the sedimentation of colloidal particles in a gravity field and measure the segregation in the system and the composition of the clusters of particles found in the deposit. The asymmetry between Stokes coefficients implies that the interactions with the fluid are different for both species. Apart from this coefficient, we do not consider any further hydrodynamic interactions which renders this model somewhat unrealistic. However, we realize that the role of the hydrodynamics is not the principal mechanism for the demixing of the species. In an effort to advance towards more realistic systems that can be easily realized in experiments, we propose, in chapters 5 and 6, a system where particles respond with different intensities to the external potential. The cost is that, in these systems, the segregation of species is the equilibrium state and it is not a purely dynamical effect anymore. In chapter 5, we study a system that is completely demixed in equilibrium, but the dynamics lead consistently to kinetically arrested states populated with compositional defects as well as, to a lesser degree, structural defects. We further devise a protocol that is able to drive the system to the equilibrium state.

One of the goals of this thesis is to make theoretical predictions that can be tested in experiments. In chapter 5, we report preliminary experiments in good qualitative agreement with the theory but due to challenges in the development of the experimental setup we were not able to make a detailed comparison up to the time of the writing. A successful collaboration between theory and experiments is reported in chapter 6 where we use random fields instead of the spatially well defined fields considered in the previous chapters.

Colloids can also be used to fabricate photonic materials when they are arranged in a periodic manner [36]. These materials mirror many of the properties of their atomic counterparts [37]. However, in an atomic crystal it is not possible to systematically control the density of structural defects. In chapter 6, we take advantage of the characteristics of colloidal systems and propose a way to control the density of structural defects in binary colloidal mixtures by random potentials [38]. We compare our theoretical results with the experiments preformed by our collaborators. Our method can be used in the future to study the way defects can affect the properties of the materials such as rigidity or electric conductivity.

1.4 List of publications from the thesis

1. André S. Nunes, Akshat Gupta, Nuno A. M. Araújo, Margarida M. Telo da Gama, *Field-driven dynamical demixing of binary mixtures*, Molecular Physics 116, 3224-3230, (2018).

   I am the first author and main contributor. The results from this paper are presented in chapter 3.

2. André S. Nunes, Sabareesh K. P. Velu, Iryna Kasianiuk, Denys Kasyanyuk, Agnese Callegari, Giorgio Volpe, Margarida M. Telo da Gama, Giovanni Volpe, Nuno A. M. Araújo, *Ordering of Binary Colloidal Crystals by Random Potentials*, submitted.

   I am the first author and main writer of the manuscript. I played the role of managing the collaboration between groups, contributed with the theoretical results and the analysis and interpretation of the data. I also helped with the treatment of the experimental data. The results are presented in chapter 6.

3. André S. Nunes, Vasco C Braz, Margarida M. Telo da Gama, Nuno A. M. Araújo, *Dynamical demixing of a binary mixture under sedimentation*, submitted.

   I am the first author and main writer. The results from this paper are presented in chapter 5.

1.5 Other publications related with the thesis

1. André S. Nunes, Nuno A. M. Araújo, Margarida M. Telo da Gama, *Self-assembly of colloidal bands driven by a periodic external field*, The Journal of chemical physics 144, 034902, (2016).

   This was a study done on monodispersed systems of coloidal particles interacting with external fields. The results from this work served as preparation and motivation to study binary mixtures, discussed in this thesis.

2. Sunita Kumari, André S. Nunes, Nuno A. M. Araújo, Margarida M. Telo da Gama, *Demixing of active particles in the presence of external fields*, The Journal of chemical physics 147, 174702, (2017).

   In this paper, we study the dynamics of active particles in external fields. These differ from passive systems since the particles have self propulsion. I contributed by developing

all numerical tools and assisted in the analysis of the results and in the writing of the manuscript.

3. Darshana Joshi, Dylan Bargteil, Alessio Caciagli, Jerome Burelbach, Zhongyang Xing, André S. Nunes, Diogo E. P. Pinto, Nuno A. M. Araújo, Jasna Brujic, Erika Eiser, *Kinetic control of the coverage of oil droplets by DNA-functionalized colloids*, Science advances 2, e1600881, (2016).

   This work on the dynamics of colloidal particles on the surface of spherical droplets was done in collaboration with experimental groups. My contribution was on developing a method to preform Brownian dynamics on curved surfaces to validate theoretically the results from the experiments.

4. Lara Carvalho, Pedro Patricio, Susana Ponte, Carl-Philipp Heisenberg, Luis Almeida, André S. Nunes, Nuno A. M. Araújo, Antonio Jacinto, *Occluding junctions as novel regulators of tissue mechanics during wound repair*, Journal of Cell Biology 217, 4267-4283, (2018).

   This paper is on wound-healing of cellular tissues and it was also done in collaboration with experimental groups. The experience I gained working with experimental data during the progress of my thesis, allowed me to have a critical contribution in this paper where I developed a new method of image processing that was used to identify individual cells in the pictures of the tissue obtained experimentally, that allowed the treatment of the data in a systematic way.

The full list of my publications can be found in the CV.

Chapter 2

Numerical and analytical models

One of the great advantages of working with colloids is that, with the computational capacities currently at our disposal, we are able to develop numerical models that simulate systems of many particles with high accuracy. The degree of control we have in these simulations goes beyond what can be achieved in the laboratory, as we are able to add and remove physical mechanisms and identify their role and impact in the overall dynamics. However, it is not without challenges due to the number of degrees of freedom involved. For our purposes, we can approximate the molecules of the fluid by individual particles that are interacting with the colloids. We still have to manage a number of the order of 10^{23} particles, which is beyond the reach of current numerical treatments since there are always computational and time constraints. To address this issue, we need to resort to additional approximations where a large fraction of the degrees of freedom are coarse grained.

Throughout the research work developed for this thesis, we used several numerical and analytical techniques that we implemented from scratch and will be described in this chapter. Our results rely heavily upon these tools and we estimate that the total computational time we used surpasses two hundred years.

2.1 Brownian Dynamics

Brownian Dynamics (BD) is widely used to simulate the time evolution of colloids in a fluid where thermal fluctuations are important [39]. We start by considering the Langevin equation

$$m\frac{d\vec{v}}{dt} = -\gamma\vec{v} + \vec{\xi}, \tag{2.1}$$

that describes the motion of a single particle in such an environment. Here, m is the mass of the particle, $\vec{v}$ is its velocity. Throughout the text we use $\frac{d}{dt}$ to represent the time derivative.
The two terms on the right hand side describe the interaction between the particle and the fluid. The first term, is the well known Stokes term which states that the drag force on a particle moving through a viscous fluid is proportional to its velocity [40]. The drag coefficient, γ, is a function of the geometry of the particle. In this work we consider spherical particles only and it can be written as

$$\gamma = 3\pi\eta d_p, \tag{2.2}$$

where η is the viscosity of the fluid and d_p is the diameter of the particle. Note that with this description, we are coarse-graining the fluid so that we will not need to integrate the equation of motion of each individual molecule and the properties of the fluid are embedded in the mesoscopic parameter γ. This approach is only sound in the limit where the size of the particles of the fluid (e.g. a water molecule is $\sim 10^{-4}\mu m$) is much smaller than the size of the colloids ($\sim 1\mu m$) [11].
The second term in Eq. 2.1 describes the thermal fluctuations as a consequence of the momentum transfer occurring at the microscale between the molecules and the colloids. We assume that the fluid is in thermal equilibrium at a given temperature T and the particles are subjected to multiple collisions from all directions with the fluid molecules that are in the vicinity and have different velocities. The collective effect of the collisions occurring in a large enough time interval ($\Delta t \gg \frac{m}{\gamma}$) can be described by a random force $\vec{\xi}$ that has zero mean, $\langle\vec{\xi}\rangle = 0$, and a second moment that is uncorrelated in space and time [41]

$$\left\langle \xi_i^n(t)\xi_i^l(t')\right\rangle = 2k_{\mathrm{B}}T\gamma\delta_{nl}\delta(t-t'), \tag{2.3}$$

where i identifies the particle, n and l are indices that run over the space dimensions and k_{B} is the Boltzmann constant. For numerical purposes, the stochastic force is commonly generated from a Gaussian distribution with such statistical properties.
We can use Eq. 2.3 to establish the Stokes-Einstein relation [41]

$$D = \frac{k_B T}{\gamma}, \tag{2.4}$$

that defines the diffusion coefficient, D, of the colloidal particles.
The type of systems we consider are in the limit of low Reynolds number, as both the particle size and velocities are small and the viscosity of the fluid is typically high enough to render

the inertial forces negligible when compared with the drag force (e.g. a common fluid that is used is water with viscosity $\eta \sim 1$ mPa s). It is therefore, a good approximation to work in the overdamped regime where the left hand side of Eq. 2.1 is taken to be zero for $\Delta t \gg \frac{m}{\gamma}$ which are the time-scales of interest. The equation of motion of a particle in a viscous fluid is

$$\gamma \frac{d\vec{r}}{dt} = \vec{\xi}, \tag{2.5}$$

where r is the particle position. Note that in this limit, the equation of motion becomes a first order differential equation, which simplifies the numerical integration.

Until now we have not yet considered particle-particle interactions. It is currently possible to have a great deal of control over the particle-particle interactions in an experimental setting. For example, the range of the interaction can be controlled by changing the pH of the fluid and the anisotropy can be controlled by shaping particles with different geometries.

In many-body systems the exact interaction potential has contributions from the interaction between all pairs, triplets, quadruplets... The pair potential is expected to be the leading term, the triplet term should be relevant at high densities and the higher order terms can be safely neglected since it is expected that they are much smaller than the previous two [42]. In practice, it is common to also neglect the triplet term, which is a good approximation in systems with short range interactions and it is also convenient since, to do otherwise, would be computationally prohibitive in a system of N particles. We use in the simulations standard empirical potentials that describe the effective interactions.

The pairwise potential for spherical particles with an isotropic charge surface distribution should be radial and depend on the distance between particles i and j, $r_{ij} = |r_i - r_j|$. In general, it can depend also on other parameters such as density and temperature, but we do not consider such cases in this text. The charge at the surface of the colloids polarizes the molecules of the fluid which induces a dipole moment that screens on the otherwise Coulomb interactions between two spherical charges. The effective electromagnetic interactions between particles and mediated by the fluid is usually described by the Yukawa potential [43, 44]

$$V_{\text{Yukawa}}(r_{ij}) = V_0 \frac{\exp\left(-\alpha r_{ij}\right)}{r_{ij}}, \tag{2.6}$$

where V_0 sets the energy scale and α is the inverse screening length that sets the range.

In some experimental settings the screening effect is so strong that the range of the interaction decreases considerably and the particles behave as hard spheres, as we will show further in

the text. Such interactions can be suitably described by the repulsive part of a Lennard-Jones potential:

$$V_{\text{Lennard-Jones}}(r_{ij}) = \varepsilon \left[\left(\frac{d_p}{r_{ij}} \right)^{12} - \left(\frac{d_p}{r_{ij}} \right)^{6} \right], \tag{2.7}$$

where ε sets the energy scale. This is a very steep and short-ranged potential that only affects neighbouring particles within a cut-off distance $r_{\text{cut}} = 2^{-1/6} d_p$.

The interactions due to the presence of external fields can be easily introduced in the form of a potential that acts on single particles. They can be of different kinds: space-dependent and/or time-dependent. Examples of both types are going to be given in the text. External interactions have a central role in determining the final state of the system. They can be used to control equilibrium configurations but they can also be used to keep the system far from equilibrium.

When we take all the interactions into consideration the motion of a particle i is described by the overdamped Langevin equation

$$\gamma \frac{d\vec{r}_i}{dt} = -\vec{\nabla}_i \left[\sum_j V_{ij}(r) + V_{\text{ext}}(\vec{r}_i) \right] + \vec{\xi}_i, \quad j \neq i, \tag{2.8}$$

We study a system of spherical particles with the movement confined to a two dimensional plane and do not consider hydrodynamic effects other than the drag on the colloidal particles. The characteristic time is defined as $\tau = d_p^2 \gamma / k_{\text{B}} T$, which is the Brownian time and it can be understood as the average time a particle takes to diffuse in a region of the size of its volume. Equation (2.8) is integrated following the algorithm developed by Branka and Heyes [45], i.e. a second-order stochastic Runge-Kutta scheme, with a time step of $\Delta t = 10^{-4} \tau$.

2.2 Monte Carlo

While BD is ideal to study the dynamics of many particles, it is often the case that these systems get trapped in states that do not correspond to the equilibrium configuration where the Helmholtz free energy is at the global minimum. These are often referred to as kinetically trapped states and they depend heavily on the history of the system. We are interested in comparing kinetically trapped states with the equilibrium configuration and for that purpose we need appropriate numerical tools.

Monte Carlo methods (MC) can be used to find thermodynamic equilibrium states. We use here the Metropolis algorithm. Starting with an initial configuration we can make successive random perturbations to the system to gradually move towards the equilibrium (e.g. changing

the position of a particle by a fraction of its size). The connection with the physical mechanisms at play is ensured by the fact that a new state after the perturbation is only accepted if:

1. the total energy of the system is decreased in the process,
2. if 1. is not satisfied the perturbation is accepted with a probability $exp(-\frac{\Delta E}{k_B T})$, where ΔE is the energy difference of the states before and after the perturbation.

The energy is computed by calculating the interactions between particles with a pairwise potential such as Eq. 2.6 or 2.7 as well as any external potentials. Condition 1. moves the system towards the minimal energy while condition 2. accounts for the thermal fluctuations present in a fluid at temperature T. It is important to note that this process does not guarantee that the global minimum is found in a finite number of iterations. In fact, in many-body problems it is quite possible for the system to get trapped in local minima with a potential barrier that is many orders of magnitude greater than $k_B T$. This issue can be mitigated to some extent, by choosing types of perturbations appropriate to the nature of the problem at hand.
Note also that the iteration process in an MC simulation does not translate into an integration in time. It is instead, to be interpreted as a minimization algorithm.

2.3 Dynamic density-functional theory

The previous sections were dedicated to methods that have a discrete approach, i.e. we consider individual particles and compute the interactions to which they are subject to. With density-functional theory (DFT), we treat the problem from the continuous point of view where we derive the space dependence of the particle density, $\rho(\vec{r})$, at equilibrium. We start by writing an approximation for the Helmholtz free energy functional [46–48]

$$\begin{aligned}\mathscr{F}[\rho] &= \int k_B T \rho(\vec{r}) \left[\log\left(\rho(\vec{r})\Lambda^3\right) - 1\right] d\vec{r} \\ &+ \frac{1}{2}\int\int \rho(\vec{r})\rho(\vec{r}\,')V_{ij}(\vec{r}-\vec{r}\,')d\vec{r}\,'d\vec{r} \\ &+ \int \rho(\vec{r})V_{ext}(\vec{r})d\vec{r}.\end{aligned} \tag{2.9}$$

On the right-hand side, the first term is the free energy of the ideal gas where Λ is the thermal de Broglie wavelength, the second term is the mean-field approximation to the contribution from the particle-particle interactions, where V_{ij} is the pairwise potential, and the last term is the external potential contribution, which is a function of space. The second term is non-local and

it can be simplified using the local density approximation (LDA) by setting $\rho(\vec{r}\,') \simeq \rho(\vec{r})$, which is adequate as long as the density is a smooth function of space [47].
The chemical potential of the system is the functional derivative of the free energy

$$\begin{aligned} \mu &= \frac{\delta \mathscr{F}}{\delta \rho(\vec{r})} \\ &= \frac{\partial L}{\partial \rho(\vec{r})} - \frac{d}{d\vec{r}}\left(\frac{\partial L}{\partial \nabla \rho(\vec{r})}\right), \end{aligned} \tag{2.10}$$

where L is defined as

$$\mathscr{F} = \int L[\vec{r}, \rho(\vec{r}), \nabla\rho(\vec{r})]d\vec{r}. \tag{2.11}$$

Using the LDA we can then write

$$\mu = k_B T \log\left(\rho(\vec{r})\Lambda^3\right) + A\rho(\vec{r}) + V_{ext}(\vec{r}), \tag{2.12}$$

where A is defined as

$$A = \int V_{ij}(\vec{r})d\vec{r} \tag{2.13}$$

and is the parameter that sets the strength of the interactions expressed in units of $k_B T r_p^2$. Rearranging Eq. 2.12, we find an expression for the density profile at equilibrium

$$\rho(\vec{r}) = Z\exp[-\beta\left(V_{ext} + A\rho(\vec{r})\right)], \tag{2.14}$$

where $\beta = (k_B T)^{-1}$ and $Z = \Lambda^{-3}e^{\beta\mu}$ is a normalization constant that represents the density of an ideal gas with chemical potential μ.
Based on this theory, there is a convenient method to derive the equation of motion of the density profile known as dynamic density-functional theory (DDFT). If we consider that the system evolves adiabatically, the evolution equation of the local density can be derived from the equilibrium Helmholtz free energy functional [49, 50],

$$\gamma\frac{\partial\rho(\vec{r},t)}{\partial t} = \vec{\nabla}.\left[\rho(\vec{r},t)\vec{\nabla}\frac{\delta\mathscr{F}[\rho(\vec{r},t)]}{\delta\rho(\vec{r},t)}\right]. \tag{2.15}$$

Using the functional in Eq. (2.9), we obtain the evolution equation for the density,

$$\gamma\frac{\partial\rho}{\partial t} = \vec{\nabla}.\left[A\rho\vec{\nabla}\rho + \vec{\nabla}V_{ext}\rho\right] + k_B T\nabla^2\rho \quad . \tag{2.16}$$

This equation expresses the way the density evolves in a system with interacting particles in a bath at temperature T, subject to an external potential that varies in space.

2.4 Fourier Filtering Method

Lasers can be used to drive colloidal particles in the laboratory. When a beam is shone trough a complex medium, such as a tissue, the interference pattern that is formed is a random landscape of intensities that we call a speckle. The particles are attracted to the points of higher intensity. The speckle has two important statistical properties. The first is that the intensities are exponentially distributed, and the second is that the points in space are correlated with a Gaussian distribution [51].

We are interested in using optical fields of this nature as the external drive in the simulations of chapter 6. It is a great challenge to produce such a random surface numerically. A common approach is to distribute several sources with different intensities randomly in space and solve Maxwell's equations to generate the resulting interference patterns. However, this method has the disadvantage of being heavily dependent on the system size. More importantly, the auto-correlations of the surface cannot be controlled directly, instead, we need to adjust indirect parameters such as the density and intensity of light sources to tune the auto-correlations.

We developed a different approach based on the Fourier filtering method (FFM) to generate the speckle numerically [52, 53]. With our method, we can chose precisely the shape of the auto-correlations of the surface.

The FFM takes advantage of the Wiener-Khinchin theorem [54]. The auto-correlation function, $C(r)$, of a given function $E(r)$ is

$$C(r) = \int_{-\infty}^{+\infty} \bar{E}(r')E(r+r')dr'. \tag{2.17}$$

The function $E(r)$ can also be expressed in terms of its Fourier coefficients as

$$E(r) = \int_{-\infty}^{+\infty} E_k \exp(2\pi ikr)dk, \tag{2.18}$$

and its complex conjugate

$$\bar{E}(r) = \int_{-\infty}^{+\infty} \bar{E}_k \exp(-2\pi ikr)dk. \tag{2.19}$$

We now substitute Eqs. 2.18 and 2.19 in the auto-correlation function Eq. 2.17

$$\begin{aligned} C(r) &= \int_{-\infty}^{+\infty}\int_{-\infty}^{+\infty}\int_{-\infty}^{+\infty} \bar{E}_k E_k \exp(2\pi i[k-k']r') \exp(2\pi i k' r) dr' dk' dk \\ &= \int_{-\infty}^{+\infty}\int_{-\infty}^{+\infty} \bar{E}_k E_k \delta(k-k') \exp(2\pi i k' r) dk' dk, \end{aligned} \tag{2.20}$$

where $\delta(k-k')$ in the second line is the Dirac-delta function. By integrating in dk', we are left with

$$\begin{aligned} C(r) &= \int_{-\infty}^{+\infty} \bar{E}_k E_k \exp(2\pi i k r) dk \\ &= \int_{-\infty}^{+\infty} |E_k|^2 \exp(2\pi i k r) dk. \end{aligned} \tag{2.21}$$

The auto-correlation function is the inverse Fourier transform of the absolute value of its Fourier coefficients, $|E_k|^2$. This relation allows us to sample random Fourier coefficients that when transformed back into real space describe a random landscape with the desired spatial correlations, $C(r)$. In our case Gaussian,

$$C(r) \propto \exp\left(-\frac{r^2}{2\sigma^2}\right), \tag{2.22}$$

where σ is the standard deviation. Note that one of the main advantages of this method is that we can control the type of correlations in the random landscape since this is one of the inputs. For example, we can change the average width of the intensity peaks by tuning σ.

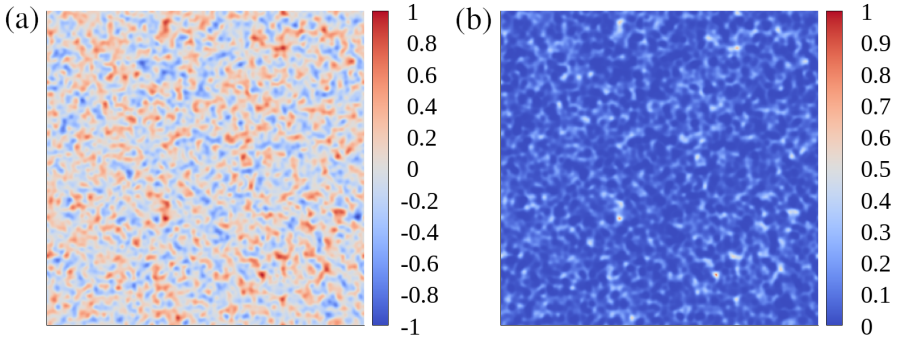

FIGURE 2.1: (a) Random landscape with a Gaussian intensity distribution that is obtained with the FFM. (b) The same landscape after the substitution procedure to obtain an exponential distribution of intensities to form a speckle. Note that in (a) there are negative intensities while in (b) they are all positive.

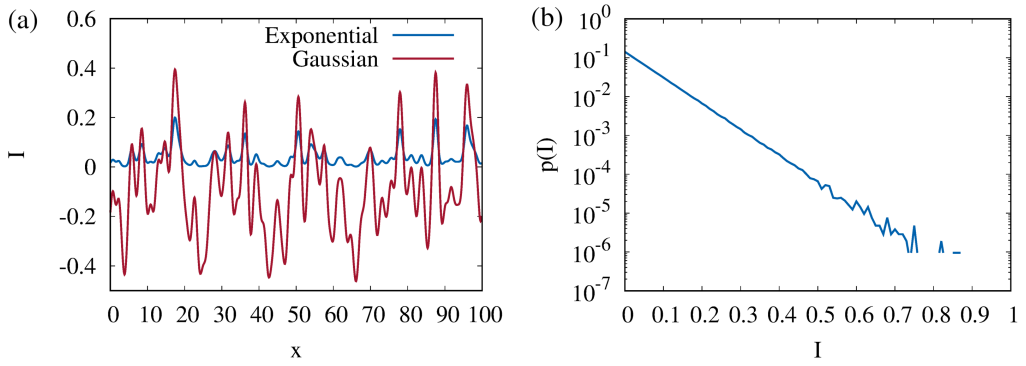

FIGURE 2.2: (a) Intensity profiles in the Gaussian surface (red line) and in the exponential surface (blue line). (b) Intensity distribution of the final random landscape.

However, the intensities produced with FFM, have a Gaussian distribution instead of the exponential one exhibited by the speckle. To overcome this issue, we used the following procedure: the random surface is discretized in a matrix with 1024×1024 cells, which we sort by the value of the intensity. Then, we produce a sorted list of intensities drawn from an exponential distribution and substitute each cell intensity by the corresponding entry on the ranked list of intensities. An example of a surface with Gaussian distribution of intensities is shown in Fig. 2.1(a) and the same landscape after the substitution procedure is shown in Fig. 2.1(b), where the distribution of intensities is exponential.

The effects of the substitution procedure on the intensity distribution is clearly shown in Fig. 2.2(a) where we show an intensity profile of the random landscapes from Fig. 2.1. The positive peaks in the Gaussian surface correspond to positive peaks in the exponential surface as well (albeit smaller). However, the negative values of the Gaussian surface are transformed to near zero intensity regions in the speckle. We confirm in Fig. 2.2(b) that the distribution of intensities in the final landscape is in fact exponential.

In Fig. 2.3 we show that the spatial auto-correlations of both the Gaussian and exponential landscapes are the same and very similar to the correlation function used as input.

We tested the above procedure with power-law correlation functions also and confirmed that it does lead to the desired distribution of intensities, without affecting the nature of the correlation function.

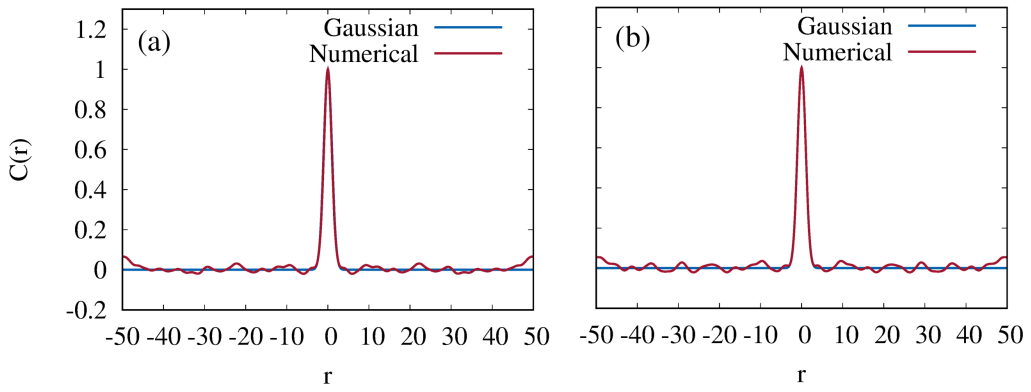

FIGURE 2.3: Auto-correlation functions of the intensities in the speckle. The blue line shows the function we use as input to form the speckle and the red line is the numerical value calculated from the speckle matrix. (a) shows the auto-correlation in the Gaussian surface after the FFM and (b) shows the auto-correlation after the substitution procedure.

Chapter 3

Field-driven dynamical demixing of binary mixtures

In this chapter, we consider mixtures of two species of spherical colloidal particles that differ in their Stokes coefficients, but are otherwise identical, in the presence of an external field. Since the particle-particle and particle-field interactions are the same for both species, they are completely mixed in the thermodynamic limit in the presence of any static field. Here, we combine Brownian Dynamics (BD) and Dynamic Density Functional theory (DDFT) of fluids to show that for sufficiently large differences in the Stokes coefficients (and corresponding differences in mobilities) dynamical demixing is observed. These demixed states are transient but, under certain conditions, packing effects compromise the relaxation towards the thermodynamic states and the lifetime of the demixed phases increases significantly.

The ability to grow colloidal structures from their spontaneous self-organization is among the most critical challenges of the Physics of Soft Condensed Matter [55, 56]. Successful strategies include induced crystallization [57–60], the use of surfaces and interfaces, with and without templates [61–64], particle functionalization [65–67] and external fields [51, 68]. For single component systems, the feasibility of the targeted structures may be controlled through the response of the colloidal system to external perturbations, e.g., changes in temperature, interaction with the surface, or with the external fields [69, 70]. For multi-component systems, asymmetries in the dynamical response are expected to lead to richer dynamics, paving the way to new routes for the assembly of the target structures [71–73].

As a step in this direction, we investigate the dynamics of field-driven self-organization of binary mixtures. Spatially dependent fields are used in experiments as virtual molds to drive colloidal suspensions into structures that exhibit the symmetries of the field [74]. The final structure of

each species will depend on the particle-field and particle-particle interactions. In order to focus on the role of the dynamics, we consider binary mixtures of particles that differ solely in their Stokes friction coefficients, but have identical particle-field and particle-particle interactions. Thus, in the corresponding thermodynamic phases, both species are completely mixed and the spatial arrangement of the particles corresponds to that of a single component system with the same (total) density, as the species are indistinguishable from the thermodynamic point of view. We use BD and DDFT, to study the dynamics of such mixtures in the presence of an external field. We consider a field corresponding to a sinusoidal potential with a minimum at the center of the simulation box. We show that when the field is switched on, albeit both species tend to move towards the minimum, dynamical demixing is observed for sufficiently different Stokes coefficients, since the species respond differently to the field. We also find that, as the field leads to an increase in the density at the minimum of the potential, at sufficiently high densities packing effects may compromise the access to the thermodynamic (mixed) phases.

3.1 Model and Simulations

We consider a binary mixture of colloidal particles in a two-dimensional square domain of lateral size L and periodic boundary conditions in both directions. The equation of motion of a particle i in the overdamped regime is very similar to Eq. 2.8

$$\gamma_i \frac{d\vec{r}_i}{dt} = -\vec{\nabla}_i \left[\sum_j V_{pp}(r_{ij}) + V_{ext}(\vec{r}_i) \right] + \vec{\xi}_i, \quad j \neq i \tag{3.1}$$

but here, we consider two species of spherical particles that differ in their Stokes coefficients, i.e., they have different γ_i, namely, γ_f and γ_s, with $\gamma_f < \gamma_s$. We denote the species by fast and slow, γ_f and γ_s, respectively. From the Stokes-Einstein relation, $D_i = k_B T/\gamma_i$, fast particles have a higher diffusion coefficient than slow ones.

We model the interparticle pairwise interaction with a Yukawa potential,

$$V_{pp}(r_{ij}) = V_0 \frac{\exp\left(-\alpha r_{ij}\right)}{r_{ij}}, \tag{3.2}$$

where V_0 sets the energy scale of the interaction and $\alpha = (2r_p)^{-1}$ its range. r_p is the characteristic particle radius (both for fast and slow particles) which we set as the unit of length in this

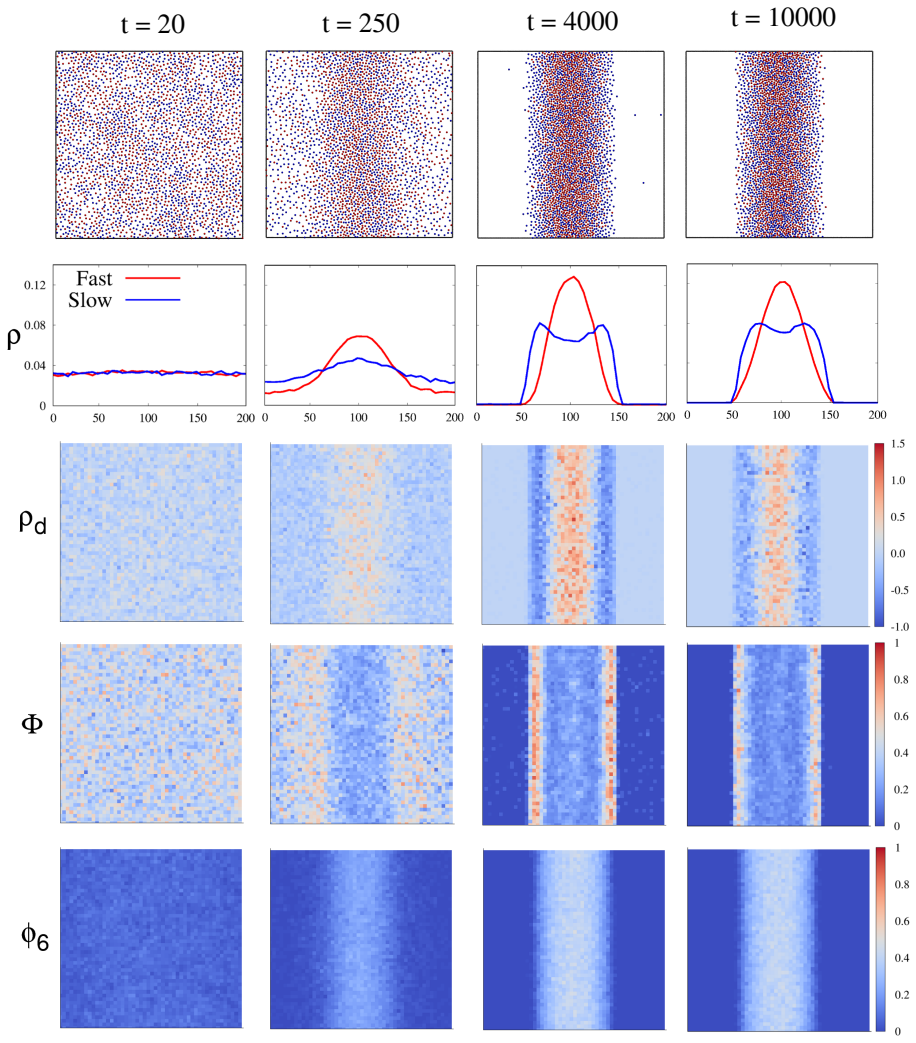

FIGURE 3.1: In the first row are snapshots at $t = 20, 250, 4000, 10000$. Blue and red particles are slow and fast, respectively. The ratio between the friction coefficients is $\Gamma = 6$ and the energy scales are $V_E = 70$ and $V_0 = 50$, respectively. The second row shows the density profiles along the x-direction. In the third row we depict the difference in the local densities in each region of the simulation box obtained by discretizing the simulation space using a mesh of squares with lateral size $4r_p$. The fourth row depicts the local segregation parameter and the fifth row the local 6-fold bond order parameters, obtained from the same discretization. The results shown in the 2^{nd} to 5^{th} rows are averages over 20 samples.

chapter. For simplicity, we consider only repulsive interactions ($V_0 > 0$). Note that the potential is independent of the type of the particles and only depends on the distance $r_{ij} = |\vec{r}_i - \vec{r}_j|$ between particles i and j.

The external potential is sinusoidal in the x-direction with a minimum at the center of the simulation box

$$V_{ext}(x) = V_E \cos\left(\frac{2\pi}{L}x\right), \tag{3.3}$$

where V_E sets the strength of the interaction between the field and the particles. Note that the potential only varies in the x-direction. The initial configuration is random with the particles uniformly distributed. When the external field is switched on, particles of both species are driven towards the center of the simulation box (along the x-direction). Since the interparticle and particle-field interaction potentials are independent of the particle species, the particles in the thermodynamic phases are completely mixed.

The potential is expressed in units of k_BT and time is defined in units of the Brownian time $\tau = r_p^2\gamma(k_BT)^{-1}$. The simulations ran for a time up to $t = 10^4$. The box linear size is $L = 200$ and the mixture is equimolar with a total number of particles $N = 2600$. The energy scales are $V_E = 70$ and $V_0 = 50$, unless stated otherwise.

3.2 Results

Fast particles have higher diffusivity and mobility than slow ones. We define the relevant control parameter $\Gamma = \gamma_f/\gamma_s$, which is adimensional. Particles are identical in the limit $\Gamma = 1$, with the relaxation dynamics and equilibrium properties of single component systems, as discussed in Ref. [68]. Below, we consider the case $\Gamma \neq 1$, when fast and slow particles differ in their Stokes coefficients.

3.2.1 High temperatures

First we consider the case where the temperature is high enough to avoid crystallization. Figure 3.1 (first row) shows snapshots at different instants in time (increasing from left to right) and $\Gamma = 6$. When the field is switched on, particles are dragged towards the center of the simulation box, forming a band along the y-direction, reproducing the symmetry of the potential.

The asymmetry between the particles Stokes coefficients leads to distinct responses to the external potential. Fast particles move faster than slow ones, triggering dynamical demixing. Note that, at all times, there is a higher concentration of fast particles along the center than of slow ones. This is also observed in the evolution of the density profiles in the x-direction shown in the second row of Fig. 3.1, where the red and the blue lines are for fast and slow particles, respectively. The third row in the same figure shows the difference between the fast and

slow particle densities in each region of the simulation box, normalized by the total density, $\rho_d = (\rho_f - \rho_s)/\rho_t$, where the positive regions (in red) are where the density of fast particles is higher. We see that, starting from a uniform distribution of both species, segregation is observed, with the fast particles in the center and the slow particles accumulated at the boundaries of the band.

For a more quantitative analysis, we divide the simulation box using a square mesh and define the local segregation parameter inside a mesh-cell as

$$\Phi = \frac{1}{N_c} \sum_{i}^{N_c} \frac{(n_{il} - n_{iu})^2}{(n_{il} + n_{iu})^2}, \tag{3.4}$$

where N_c is the number of particles inside the cell, n_{il} and n_{iu} are the number of like or unlike particles surrounding particle i within a cut-off distance $r_{cut} = 3$. This parameter is one if there is a single species inside the cell and zero when the number of particles of each species is the same. The time evolution of Φ is shown in the fourth row of Fig. 3.1. The spatial dependence of the particle segregation is clear at $t = 4000$. The boundaries of the band consist mainly of slow particles, while in the center, although there is a higher density of fast particles, the segregation is not complete, since slow particles that are initially near that region are trapped inside the band. At later times, Φ decreases at the boundaries of the band due to the expected thermodynamic mixing.

We also measured the bond order parameter, ϕ_6, for a particle i defined as

$$\phi_6 = \frac{1}{6} \left| \sum_{j}^{N_b} e^{i6\theta_{ij}} \right|, \tag{3.5}$$

where N_b is the number of neighbors surrounding a particle within the cut-off radius, r_{cut}, and θ_{ij} is the angle between a line connecting particles i and j and the x-direction. The bond order parameter is one when the particles are organized in a hexagonal structure. As shown in the last row of Fig. 3.1, for the considered model parameters, there is no six-fold symmetry inside the band and the particles are in a fluid-like state.

3.2.2 Continuum model

Particles from both species are identical from the thermodynamic point of view and should be completely mixed in the thermodynamic limit. That is why we see some degree of mixing at later times in Fig. 3.1. However, the dynamics of mixing is very slow and to observe complete

mixing much longer simulations are needed. To achieve much longer timescales and analyze the dynamics of mixing, we considered here a simple, coarse-grained continuum model based on Dynamic Density Functional Theory (DDFT) of fluids.

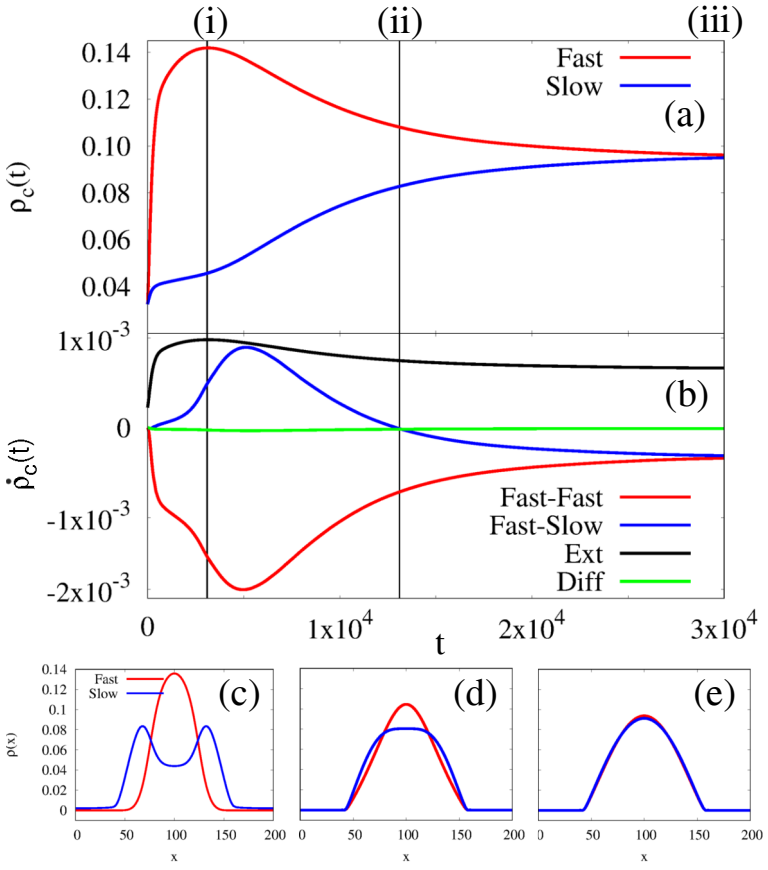

FIGURE 3.2: (a) Density evolution in the center of the band obtained from DDFT, with the red line depicting the fast particle density and the blue line the slow particle density. (b) Evolution of the individual terms of Eqs. 4.13. The red line represents the interaction between the fast particles, the blue line the interaction between different particles, the black line the interaction with the external potential and the green line the diffusion. The black vertical lines separate the three different regimes. (c), (d) and (e) show the density profiles at the boundaries between the three regimes (i), (ii) and (iii), respectively.

For the system under consideration, the free energy functional is written in terms of the fast and slow densities as

$$\begin{aligned}
&\mathscr{F}[\rho_f,\rho_s] = \\
&\sum_{i=f,s}\int k_B T\rho_i(\vec{r})\left[\log\left(\rho_i(\vec{r})\Lambda^2\right)-1\right]d\vec{r}+ \\
&\sum_{i=f,s}\sum_{j=f,s}\frac{1}{2}\int\int \rho_i(\vec{r})\rho_j(\vec{r}')V_{pp}(\vec{r}-\vec{r}')d\vec{r}'d\vec{r}+ \\
&\sum_{i=f,s}\int \rho_i(\vec{r})V_{ext}(\vec{r})d\vec{r},
\end{aligned} \tag{3.6}$$

where the indices f and s stand for fast and slow. The first term is the ideal gas contribution to the free energy, the second describes the interaction between the particles, and the third is the contribution from the interaction with the external potential. We derived the equation for the time evolution of the densities as [49]

$$\gamma_i\frac{\partial\rho_i(\vec{r},t)}{\partial t} = \nabla.\left[\rho_i(\vec{r},t)\vec{\nabla}\frac{\delta\mathscr{F}[\rho_f(\vec{r},t),\rho_s(\vec{r},t)]}{\delta\rho_i(\vec{r},t)}\right], \tag{3.7}$$

obtaining two non-linear diffusion equations,

$$\gamma_f\frac{\partial\rho_f}{\partial t} = \nabla.\left[A\rho_f\vec{\nabla}\rho_f + A\rho_f\vec{\nabla}\rho_s + \vec{\nabla}V_{\text{ext}}\rho_f\right] + k_BT\nabla^2\rho_f \tag{3.8}$$

and

$$\gamma_s\frac{\partial\rho_s}{\partial t} = \nabla.\left[A\rho_s\vec{\nabla}\rho_s + A\rho_s\vec{\nabla}\rho_f + \vec{\nabla}V_{\text{ext}}\rho_s\right] + k_BT\nabla^2\rho_s, \tag{3.9}$$

where $A = \int V_{pp}(\vec{r})d\vec{r}$ is the interaction parameter in the local density approximation, see Ref. [68] for further details. In this approximation, the densities are considered smooth functions of the position, $\rho(\vec{r}') \approx \rho(\vec{r})$, where $\vec{r}'$ is a point in the vicinity of $\vec{r}$. With this approximation, we reduce the computational effort by avoiding the evaluation of a convolution at each iteration, allowing us to access much longer time scales. As shown here, the model still captures the relevant dynamics.

We solved Eqs. 3.8 and 3.9 using the finite elements method [75] and the evolution of the densities in the center of the band is shown in Fig. 3.2 (top). Both densities increase until the point where the density of fast particles reaches a maximum and then starts to decrease. In the asymptotic limit both densities tend to the same value that corresponds to a completely mixed state, as expected in the thermodynamic limit. We can also analyze how each term in Eqs. 3.8

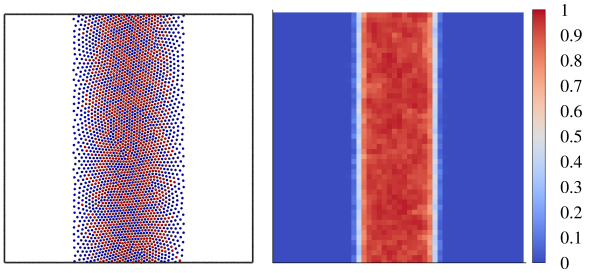

FIGURE 3.3: Asymptotic state obtained at $t = 10000$ (left) at low temperatures showing crystallization. Red particles are fast and blue are slow. The ratio between diffusion coefficients is $\Gamma = 6$ and the external and particle-particle potential scales are $V_E = 7000$ and $V_0 = 5000$, respectively. On the right-hand side we show the local 6-fold bond order parameter at the end of the simulation, averaged over 20 samples.

and 3.9 contributes to the dynamics. The middle plot in Fig. 3.2 shows the detailed evolution of Eq. 3.8 with the contribution from the fast-fast particle interaction (first term in the square brackets, red line in the plot), from the fast-slow particle interaction (second term in the square brackets, blue line in the plot), from the fast particles with the external potential (third term in the square brackets, black line in the plot) and finally from the diffusion term (last term of the equation, green line in the plot). These results show that there are three dynamical regimes, delimited by the black vertical lines in the plot. In the first regime, there is dynamical demixing caused by the difference in mobility of the two species that culminates with the peak density of the fast particles. At the maximum, the density profile of the slow particles is bimodal, as shown in Fig. 3.2(c). In the second regime, there is mixing as the fast particles density profile decreases due to diffusion and interaction with particles of the same species. Also, the slow particles density profile in the center increases at a fast rate. At the end of this regime the density profile of the slow particles is no longer bimodal, Fig. 3.2(d). In the third regime, the density profiles slowly converge to the completely mixed state.

3.2.3 Low temperatures

As discussed above, the demixing is dynamic and therefore transient. For long enough times, the system is expected to reach an equilibrium configuration, where both particle species have the same density profile. However, if the mixing time of the third regime is larger than the experimental time scale, the dynamical demixed states are the observed ones. The symmetry of the external potential favors the accumulation of particles along the y-direction, in the center of the simulation box. At high enough densities (and low temperatures), due to the local increase

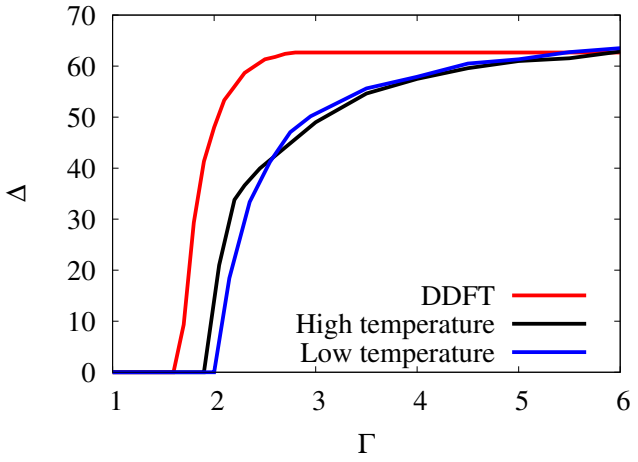

FIGURE 3.4: The distance, Δ, between the two peaks in the density profile of slow particles at high temperatures (black), low temperatures (blue) and DDFT (red). Segregation only occurs for high Γ's.

of the density, the particles rearrange in a crystalline-like structure. Mixing becomes much slower in such regimes, due to packing effects.

Figure 3.3 shows the final state when the temperature is decreased by two orders of magnitude. From the system snapshot (left) at late times as well as from the bond order parameter (right) it is clear that, the entire band crystallizes and we can, therefore, effectively freeze the system in the demixed state.

3.2.4 Dynamical demixing

The demixing occurs because the two particle species have different mobilities. Since the dynamical demixing is caused by the difference in the Stokes coefficients, we now study its dependence on Γ. We define a parameter, Δ, that measures the distance between both peaks in the slow density profile at the time when the density of fast particles in the center is maximal (at the end of the first regime). The results from Fig. 3.4 show that there is a threshold Γ^* below which no demixing is observed, corresponding to $\Gamma^* \sim 1.6$ from DDFT and $\Gamma^* \sim 2$ in the simulations. At high enough Γ the value of Δ saturates since the simulation box is finite, imposing an upper limit to the width of the band.

Note that there are little differences between the curves at high and low temperatures, which is to be expected since Δ is measured at the end of the first regime before the mixing starts at high temperatures and the density profiles are similar to those in the frozen state. The differences

between the thresholds in the DDFT and the simulations is due to the local density approximation, which neglects short and long distance correlations between the particles. Also, if we were to increase the number of particles in the system, keeping the density constant, the simulation density profiles (and Δ) would be less sensitive to finite size effects and, we would expect to find a sharper Δ curve, as that obtained from DDFT.

3.3 Remarks

We studied binary systems where the particle species are distinguished only by their Stokes coefficients. In the presence of space dependent external fields, the species are driven to the equilibrium regions faster or slower according to their mobilities, driving a transient demixing as the system evolves towards the thermodynamic equilibrium state. The final configuration is characterized by a completely mixed state since the energy landscape is the same for both species.

The amount of demixing can be controlled by tuning the ratio between the friction coefficients of the two species. This state is a transient and mixing will eventually occur. However, it is possible to increase the mixing time-scale by lowering the temperature and inducing crystallization in the high density region, in which case, the demixed state is effectively frozen.

Previous approaches to self-assembled mixtures of colloidal particles considered structures in thermodynamic equilibrium that replicate the symmetries of the virtual molds produced by external fields. However, we have shown that the dynamical properties play a critical role in this self-assembly, as the evolution of the system may be trapped in arrested states for long periods of time. This represents an obstacle that needs to be suppressed if the goal is to reach the equilibrium state.

Our results also show that the dynamics can be explored as a new method to control the self-assembly in any system where the particles have different mobilities. Adjusting the time-scales for relaxation and arresting, one can take advantage of the different dynamical properties to assemble structures that, albeit not in thermodynamic equilibrium, are reproducible and robust over long periods of time.

Chapter 4

Dynamical demixing of a binary mixture under sedimentation

We investigate the sedimentation dynamics of a binary mixture, the species of which differ by their Stokes coefficients but are identical otherwise. We analyze the sedimentation dynamics and the morphology of the final deposits using Brownian Dynamics simulations for mixtures with a range of sedimentation velocities of both species. We found a threshold in the sedimentation velocities difference above which the species in the final deposit are segregated. The degree of segregation increases with the difference in the Stokes coefficients or the sedimentation velocities above the threshold. We propose a simple analytical model that captures the main features of the simulated deposits.

The process of sedimentation, where particles in suspension settle in the presence of a gravitational field, is ubiquitous over a wide range of length scales [76–80]. For example, sedimentation plays a relevant role in natural water transport, affecting the chemical composition of the seabed [81] and the water quality in reservoirs [82, 83]. At the other end of the scale, sedimentation by ultracentrifugation is used as an analytical tool in medical, biological and pharmaceutical applications, where the constituents of a suspension are separated by molecular weight [84, 85]. At the fundamental level, sedimentation experiments were developed and used extensively in statistical physics and colloidal science to evaluate the equation of state of hard spheres [86] and to study the phase diagram of colloidal particles [87].

Studies of the sedimentation of mixtures of particles that differ in their buoyant mass revealed a rich phase stacking diagram under thermodynamic equilibrium conditions [88, 89]. The structure of the final deposit depends not only on the difference in buoyant masses but also on the particle-particle interactions [67, 90–93]. The roughness of the particle surface is known to

affect the hydrodynamics of the surrounding fluid, e.g., alters the lubrication film thickness [94, 95]. Such conditions could potentially be realized in an experiment with particles composed by a rigid core and covered by an elastic surface layer, which would affect the hydrodynamics while the pairwise interactions remain dominated by identical rigid cores. Here, to shed light on the role of the hydrodynamic radius on the sedimentation dynamics, we consider a binary mixture of particles that differ only through their Stokes coefficient. Thus, we neglect hydrodynamic interactions which are known to be relevant in different limits triggering, for example, a number of different instabilities [96, 97], following a methodology developed previously [13]. Thus, their thermodynamic phases are perfectly mixed, any demixing being dynamically induced.

When thermal fluctuations are negligible, colloidal particles in solution are expected to sediment at a sedimentation velocity that depends only on the strength of the gravitational field and their Stokes coefficient. Thus, distinct Stokes coefficients imply different sedimentation velocities. In what follows, we show that the morphology of the final deposit depends crucially on the ratio of the sedimentation velocities. Above a certain threshold, which will be quantified below, the particles are segregated in the final deposit, as they arrive at the substrate at different rates and do not have the time to relax to the thermodynamic equilibrium mixed state. We investigate this segregation and discuss how it depends on the different model parameters.

4.1 Model and Simulations

We consider a binary mixture of identical spherical particles where the two species are characterized by distinct Stokes coefficients. The particles are in a uniform gravitational field along the vertical direction (y-direction) and inside a rectangular two-dimensional box of width L_x and height L_y. We assume boundary conditions periodic in the x-direction and rigid walls in the y-direction. The trajectory of each particle i is obtained by solving the Langevin equation, in the overdamped regime,

$$\gamma_i \frac{d\vec{r}_i}{dt} = -\nabla_i \left[\sum_j^{N_t} V_{ij}(r) \right] + m\vec{g} + \vec{\xi}_i, \quad j \neq i \tag{4.1}$$

where, N_t is the total number of particles, m is a parameter that takes into account the effects of mass and buoyancy of the particles and $\vec{g} = -g\vec{e}_y$ the gravitational field. The two species differ through their values of γ_i: γ_f for fast particles and γ_s for slow ones, such that $\gamma_f < \gamma_s$, as in the

previous chapter. As a result, the two species have different sedimentation velocities, $\vec{v}_i = \frac{m}{\gamma_i}\vec{g}$ since the the particles have the same mass.

To focus on purely dynamical effects, we consider that the particle-particle interactions are identical for all the particles. We describe this interaction through a (repulsive) Lennard-Jones potential, truncated at a cut-off distance $r_{cut} = 2^{\frac{1}{6}} d_p$,

$$V_{ij}(r) = \varepsilon \left[\left(\frac{d_p}{r} \right)^{12} - \left(\frac{d_p}{r} \right)^{6} \right], \tag{4.2}$$

where ε sets the energy scale and d_p the diameter of the particles. Thus, the potential depends only on the distance $r = |\vec{r}_i - \vec{r}_j|$ between the particles i and j.

Hereafter, d_p sets the unit of length. The energy is expressed in units of $k_B T$, time is defined in units of the Brownian time $\tau = d_p^2 \gamma (k_B T)^{-1}$ and the strength of the external field, g, is given in units of $k_B T/(m d_p)$. Equation 4.1 is integrated using a second-order stochastic Runge-Kutta numerical scheme, proposed by Brańka and Heyes [45], with a time-step of $\Delta t = 10^{-4}\tau$. Initially, the particles are distributed uniformly at random (without overlapping) in the simulation box. Unless stated otherwise, we set $\varepsilon = 1$ and $g = 12$. The box size is $L_y = 200$ and $L_x = 37.5$ and the binary mixture consists of $N = 3000$ particles, with $N/2$ of each species. The initial number density is $\rho_0 = 0.4$.

4.2 Results

In the overdamped regime and neglecting thermal fluctuations, one expects that isolated particles move with a constant sedimentation velocity given by $v_i = \frac{mg}{\gamma_i}$. The rate of particle accumulation at the bottom depends on the flux density of each species at the growing front of the deposit, $\mathscr{J}_i = \rho_i v_i$, where ρ_i is the particle number density of species i. Differences in the flux density of each species result in demixing along the vertical direction as particles accumulate at different rates on the bottom and thermal fluctuations are not strong enough to promote mixing. In what follows, we set the particle densities to be the same (equimolar mixture) and vary their velocities only. The demixing that occurs during sedimentation is, therefore, purely dynamical in nature. The relevant control parameter is the ratio between the sedimentation velocity of both species, $v = \frac{v_s}{v_f} = \frac{\gamma_f}{\gamma_s}$. To study the dependence on this parameter, in the results that follow, we fix γ_f and vary v by changing γ_s, i.e., changing v_s, with v_f constant. The degree of demixing depends on v as can be seen from the final deposit density profiles $\rho_f(y)$ and $\rho_s(y)$ in Fig. 4.1. When $v = 1$ the density profiles are identical as the particles are indistinguishable. When $v \neq 1$,

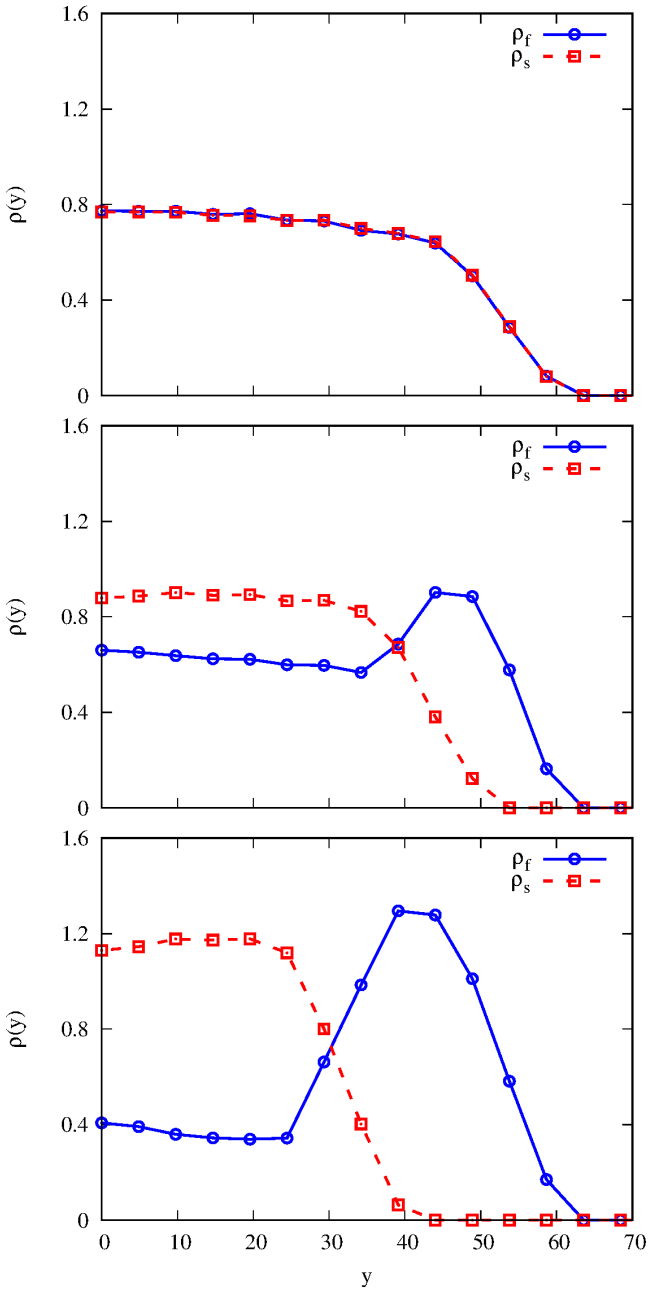

FIGURE 4.1: Density profiles as function of the height in the final deposit for fast (red lines) and slow (blue lines) particles averaged over 10^2 samples for (a) $v = \frac{v_s}{v_f} = 1$, (b) $v = 0.5$ and (c) $v = 0.1$, and $g = 12$.

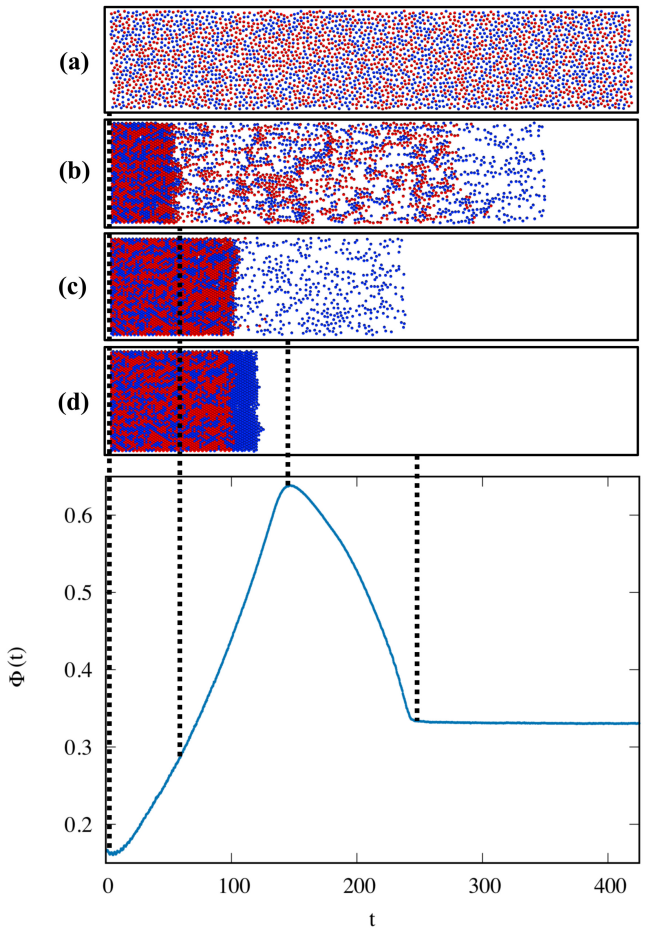

FIGURE 4.2: Time evolution of the parameter Φ averaged over 10^2 samples for $v = \frac{v_s}{v_f} = 0.5$, $g = 12$ and $\rho_0 = 0.4$. The snapshots are for four different values of t, namely, (a) 0,(b) 70,(c) 150, (d) 275.

the final deposit can be divided into two regions: one, at the bottom, where the density of the fast particles is higher than the density of the slow ones and another region, at the top of the deposit, composed essentially of slow particles. The difference between densities in the first region and the thickness of the second region increase as v decreases (see Figs. 4.1 (b) and (c)). In order to characterize the segregation along the vertical direction, we define a parameter

$$\Phi = \frac{1}{L'_y} \int_0^{L'_y} \frac{|\rho_f - \rho_s|}{\rho_f + \rho_s} dy, \tag{4.3}$$

where L'_y corresponds to the height at which the last moving (slow) particle is located, given by $L'_y = L_y - v_s t$.

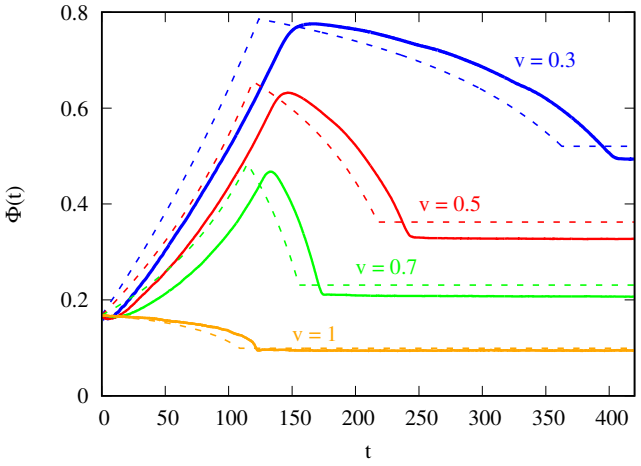

FIGURE 4.3: Time dependence of the parameter $\Phi(t)$ as a function of the ratio of the particle velocities, v. The solid lines are results of the BD simulations and the dashed lines are obtained from the analytical model (Eq. 4.17).

4.2.1 Numerical results

In order to evaluate numerically the integral in Eq. (3), we divided the simulation domain into horizontal slices of height $\Delta y = 1.5$ and width L_x. The integral is then converted into a sum,

$$\Phi(t) = \frac{1}{N_b} \sum_{i}^{N_b} \frac{|N_f - N_s|}{N_f + N_s}, \tag{4.4}$$

where N_b is the number of slices and, N_f and N_s are the number of fast and slow particles in each slice, respectively. This parameter is one if the species are completely segregated and zero if they are perfectly mixed.

The time evolution of Φ is shown in Fig. 4.2 (bottom plot). Φ grows initially until it reaches a maximum, Φ_{max}, at a time defined as t^*. For $t > t^*$, this parameter decreases until it saturates asymptotically. Note that Φ is not zero at $t = 0$. Since the particles are initially distributed uniformly at random, the average absolute difference $|N_f - N_s|$ for a given slice can be estimated from a binomial distribution. This difference follows a half-normal distribution with mean $\mu = \sqrt{\frac{2N_t}{\pi}}$, where $N_t = N_f + N_s$ is the total number of particles in the slice. Therefore, the value of Φ at the starting configuration is $\Phi(0) = \Phi_0 = \sqrt{\frac{2}{\rho_0 L_x \Delta y \pi}}$, where ρ_0 is the initial total density of particles and it vanishes only in the thermodynamic limit. The initial increase in Φ corresponds to the dynamical demixing regime where there is a rapid accumulation of the fast particles in the deposit with a fraction of the slow particles dragged along while the remaining slow particles lag behind. The peak is reached when all the fast particles deposit at $t = t^*$ (see

Fig. 4.2(c)). For $t > t^*$, Φ decreases until the remaining slow particles deposit, on a top layer consisting (almost) exclusively of slow particles, if the difference in the velocities is sufficiently large (see Fig. 4.2(d)). We define this instant as the saturation time, t_{final}. Note that, the level of segregation of the particles remains almost the same from t^* to t_{final}, as seen by comparing the snapshots (c) and (d). This parameter depends on the level of segregation and on $L'_y(t)$ that decreases with time. The region where only slow particles are present occupies a larger area at t^* than at t_{final} and the same number of particles contribute to the integral.

To characterize the structure of the deposit we measured the six-fold bond order parameter, $\langle \phi_6 \rangle$, defined as

$$\langle \phi_6 \rangle = \frac{1}{N} \sum_{l}^{N} \frac{1}{6} \left| \sum_{j}^{N_b} e^{i6\theta_{lj}} \right|, \tag{4.5}$$

where N is the total number of particles, N_b is the number of neighbors (within a cutoff of 2.5) and θ_{lj} is the angle between the line that connects the particles j and l with the x-axis. This is a continuous order parameter that is one when particles are arranged in a perfect hexagonal structure and it decreases when the order decreases. At the low temperatures considered, the particles in the deposit form an almost perfect hexagonal structure with $\langle \phi_6 \rangle = 0.9$ and the level of segregation remains the same until the end of the simulation (Φ is constant). This does not correspond to the mixed configuration expected in thermodynamic equilibrium where the particles should form a completely mixed deposit, as they are indistinguishable from the thermodynamic point of view [13]. Obviously, the deposits observed at the end of the simulations are transient but their relaxation towards equilibrium occurs on much longer timescales than the observation time.

The solid lines with open symbols in Fig. 4.3 show the time dependence of Φ obtained numerically for different values of the velocity ratio v. As expected, Φ_{max} increases as the ratio v departs from unity, showing that, as the difference between the sedimentation velocities increases, higher levels of segregation are attained in the deposit.

Reducing v, decreases the sedimentation velocity of the slow particles (keeping the velocity of the fast particles constant). However, the effective velocity of the fast particles also decreases due to the interactions with the slow ones (acting as obstacles) and, as a consequence, the time when the peak in Φ is reached, t^*, increases. The saturation time, t_{final}, is also affected by changing v since the difference between t^* and t_{final} is the time taken, by the remaining slow particles to deposit and this depends only on their sedimentation velocities.

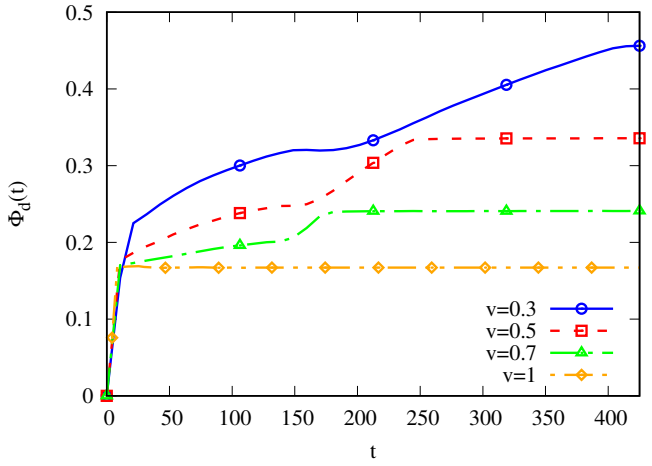

FIGURE 4.4: Time evolution of the segregation in the deposit.

The parameter Φ measures the segregation in the entire system but we can also measure the segregation only in the deposit using the following definition [17]

$$\Phi_d = \frac{1}{N_d} \sum_{i}^{N_d} \frac{\left(N_f - N_s\right)^2}{\left(N_f + N_s\right)^2}, \tag{4.6}$$

where N_d is the total number of particles with $\phi_6 > 0.9$. N_f and N_s are the number of fast and slow particles within the cutoff distance 2.5 of particle i. The segregation in the deposit increases monotonically in time (see Fig. 4.4). At t^*, the slope of the curves change indicating the phase in which only slow particles arrive and at t_{final} the value saturates at its maximum.

4.2.2 Analytical model

We consider now a simple analytical model. We assume that the particles move with a constant sedimentation velocity $v_i = \frac{mg}{\gamma_i}$ that depends only on the particle species, and we neglect particle-particle interactions and thermal fluctuations. We define the thickness of the packed deposit as $l^*(t)$. The number of particles of a species in the region $y < l^*(t)$ at a given time is the number of particles initially located at $y < l^*(t)$ plus those of that species that entered into that region. The latter can be estimated by considering that the fraction of particles of species i that entered into the region is $\frac{v_i}{v_f + v_s}$. Despite the fact that particle interactions are soft, we assume an upper bound for the density, given by the packing fraction of disks with diameter $d_p = 1$, i.e., $\rho_{max} = \frac{2\sqrt{3}}{3}$.

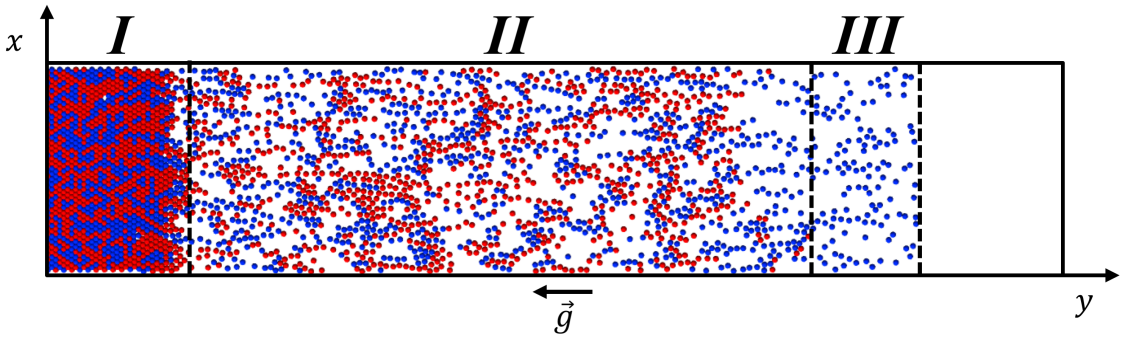

FIGURE 4.5: To evaluate the integral in Eq. 4.3 the space is divided into three regions: region *I* in the interval $[0, l^*(t)]$, region *II* in the interval $[l^*, L_y - v_f t]$ and *III* in $[L_y - v_f t, L_y - v_s t]$. In region *I* the integrand is given by Eq. 4.7, in region *II* the integrand is Φ_0 and we consider that the number of fast and slow particles entering this region is approximately the same as the number of particles leaving the region, and in region *III* the integrand is one, as there are only slow particles.

We can then estimate the density of particles by

$$\rho_i(y < l^*, t) = \frac{\rho_0}{2} + (\rho_{max} - \rho_0)\frac{v_i}{v_f + v_s}, \tag{4.7}$$

where $(\rho_{max} - \rho_0)$ is an estimate of the increase in the local density, with ρ_0 being the initial particle density.

The integral in Eq. 4.3 for $t < t^*$ can be replaced by the sum of three terms, corresponding to the contribution of three different regions, as shown in Fig. 4.5. Region *I* corresponds to the deposit, where the density of each species is given by Eq. 4.7 and we also account for the non-zero segregation factor, Φ_0, in the deposit that results from the discrete nature of the numerical integration. Region *II*, where the two types of particles are perfectly mixed, is delimited by the surface of the deposit, $y \approx l^*(t)$ and $y \approx L_y - v_f t$, the height of the last fast particle. Here, we assume that the number of particles of both species that leave region *II* is approximately the same as the number that enters and, therefore, the integrand is the constant Φ_0. The region *III* contains only one type of particles and is delimited by $y \approx L_y - v_s t \equiv L'_y$, the position of the last slow particle. In this region, the argument of the integral is one as only slow particles are present. The number of fast, N_f, and slow particles, N_s, in regions *I* and *II* can then be regarded as the number of successes and failures in a binomial distribution of N_t trials. The probability that a particle in each one of these regions is a fast particle is

$$p_{f,\alpha} = \frac{\frac{\rho_0}{2} + (\rho_\alpha - \rho_0)\frac{1}{1+v}}{\rho_\alpha}, \tag{4.8}$$

and the probability that it is a slow particle is

$$p_{s,\alpha} = \frac{\frac{\rho_0}{2} + (\rho_\alpha - \rho_0)\frac{v}{1+v}}{\rho_\alpha}, \tag{4.9}$$

where ρ_α is the the total density of each region (ρ_{max} in region I and ρ_0 in region II). The term $|N_f - N_s|$ corresponds to the absolute difference between success and failures of N_t trials that follows a folded normal distribution whose expectation value is given by:

$$\mu'_\alpha = \sigma_\alpha \sqrt{\frac{2}{\pi}} \exp\left(\frac{-\mu_\alpha^2}{2\sigma_\alpha^2}\right) + \mu_\alpha \mathrm{erf}\left(\frac{\mu_\alpha}{\sqrt{2\sigma_\alpha}}\right). \tag{4.10}$$

Here, $\mu_\alpha = N_t(p_{f,\alpha} - p_{s,\alpha})$ and $\sigma_\alpha^2 = 4N_t p_{f,\alpha} p_{s,\alpha}$ correspond respectively to the expectation and variance of the Gaussian distribution (not "folded") of the difference between successes and failures considering the values of $p_{f,\alpha}$ and $p_{s,\alpha}$. The integral for $t \leq t^*$ is then approximated by

$$\Phi(t \leq t^*) = \frac{1}{L'_y}\left[\int_0^{l^*(t)} \frac{\mu'_I}{\rho_{max}\Delta_y L_x}\, dy + \int_{l^*}^{L_y - v_f t} \frac{\mu'_{II}}{\rho_0 \Delta_y L_x} dy + \int_{L_y - v_f t}^{L'_y} dy\right]. \tag{4.11}$$

For $t^* < t < t_{final}$ region II has zero thickness and thus

$$\Phi(t > t^*) = \frac{1}{L'_y}\left[\int_0^{L^*} \frac{\mu'_I}{\rho_{max}\Delta_y L_x} dy + \int_{L^*}^{L'_y} dy\right], \tag{4.12}$$

where $L^* = l^*(t^*)$ is the length of the structure at $t = t^*$.
We estimate $l^*(t)$ in the following way. The number of deposited particles is given by the flux of particles through the line defined by $y = l^*(t)$ plus the number of particles that is initially present in the region below this height. We consider that particles travel with constant velocity, v_i, for $y > l^*(t)$ and that the flux through that line for each species can be written as $j_i(t) = \frac{\rho_0}{2} v_i L_x$. The number of particles in the deposit, N_s, is

$$N_s = \rho_{max} L_x l^*(t) = L_x l^*(t)\rho_0 + \left(\frac{\rho_0}{2} v_f + \frac{\rho_0}{2} v_s\right) t L_x. \tag{4.13}$$

We can now rearrange the terms and the expression for l^*, obtaining

$$l^*(t) = \frac{\frac{\rho_0}{2}(1+v)}{\rho_{max} - \rho_0} v_f t. \tag{4.14}$$

For $t > t^*$, all the fast particles are deposited and

$$L^* = \frac{\rho_0 L_y (1+v)}{2\left[\rho_{max} - \rho_0 + \frac{\rho_0}{2}(1+v)\right]}. \tag{4.15}$$

Since $L^* = l^*(t^*)$,

$$t^* = \frac{(\rho_{max} - \rho_0) L_y}{v_f \left[\frac{1}{2}\rho_0 (1+v) + (\rho_{max} - \rho_0)\right]}. \tag{4.16}$$

The height of the final deposit is $l^*(t_{final}) = \frac{N}{\rho_{max} L_x}$, where t_{final} is the time when the last slow particle deposits which can be estimated as $t_{final} = (L_y - \frac{N}{\rho_{max} L_x})/v_s$. At later times the parameter Φ remains constant as no more particles are added to the deposit.
Thus, the parameter Φ is

$$\Phi(t) = \begin{cases} \frac{1}{L_y - v_s t}\left[\frac{\rho_0(1+v)}{2(\rho_{max}-\rho_0)}\left(\frac{\mu_I'\rho_0 - \mu_{II}'\rho_{max}}{\rho_{max}\rho_0 \Delta y L_x} - \frac{\mu_{II}'}{\rho_0 \Delta y L_x} + 1 - v\right) v_f t + \frac{L_y \mu_{II}'}{\rho_0 \Delta t L_x}\right], & t \le t^* \\ 1 + \frac{L^*}{L_y - v_s t}\left[\frac{\mu_I'}{\rho_{max}\Delta y L_x} - 1\right], & t^* \le t \le t_{final} \\ 1 + \frac{L^*}{L_y - v_s t_{final}}\left[\frac{\mu_I'}{\rho_{max}\Delta y L_x} - 1\right], & t \ge t_{final}. \end{cases} \tag{4.17}$$

The dashed lines in Fig. 4.3 show the time dependence of Φ obtained from Eq. 4.17 for different values of the ratio v. The comparison with the numerical results reveals that the analytical calculation reproduces the main features of the simulations. The highest levels of segregation are achieved for the lowest v, when the difference between the velocities is largest. In this limit, the slow particles travel much slower than the fast ones and are, on average, the last to deposit forming a thick layer on the top consisting of slow particles only. For $v = 1$, the particles are indistinguishable and the maximum value of Φ is the (finite-size) initial value.
So far, we discussed segregation along the y-direction of the deposit. However, from the snapshot in Fig. 4.2(d) it appears that at the bottom of the deposit there are linear-like clusters of particles that form structures along the y-direction, which may promote segregation along the x-direction as well. To further investigate this question, we identified all the clusters of particles in the final deposit below the top layer of slow particles and calculated their inertia tensor. We defined the parameter $r_I = \frac{1}{N_c}\sum r_c$, where r_c is the ratio between the smallest and the largest (non-zero) eigenvalues of the inertia tensor of the cluster c and the sum is over all clusters of

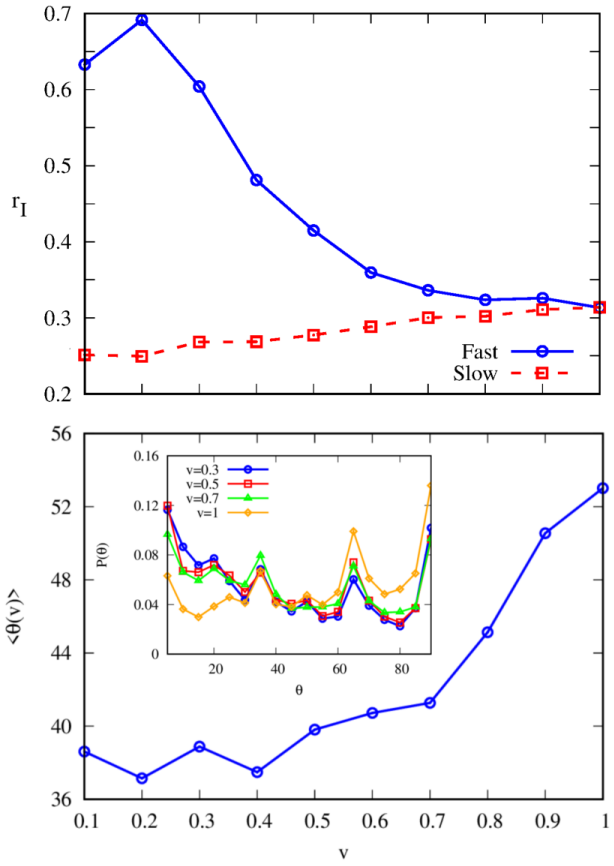

FIGURE 4.6: Top panel: ratio between the lowest and highest (non-zero) eigenvalues of the inertia tensor of the clusters of particles in the final deposit. Bottom panel: average angle between the principal eigenvector of the slow cluster with the y-direction. The inset shows the angle distribution for different velocity ratios.

the same species with N_c the number of such clusters. This parameter is one when all the clusters are symmetric and falls below one as the clusters deviate from the symmetric shape. We measure r_I for clusters larger than two particles excluding the largest cluster, where finite size effects may be significant. A deposit with randomly distributed particles is equivalent to the case with $v = 1$, where the particles are indistinguishable. In this limit, r_I is low, which suggests the prevalence of symmetrical clusters. In the limit of low v, the number of fast particles is much larger than the number of slow ones in the region under consideration and they form a single large cluster. Accordingly, as shown in Fig. 4.6 (top panel), r_I increases for fast particles as v decreases. The opposite occurs for the slow particles where r_I decreases, showing that, as the ratio of velocities decreases, the clusters of slow particles tend to lose symmetry. In the bottom panel of Fig. 4.6, we plot the average angle, $\langle\theta\rangle$, with the y-direction of the eigenvector

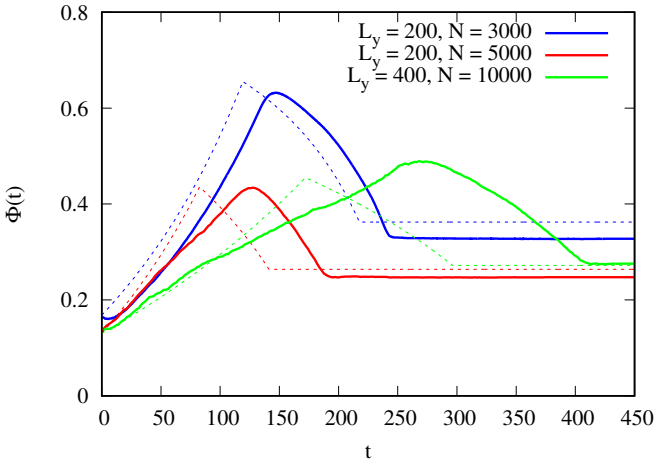

FIGURE 4.7: Order parameter in simulations (solid line) and analytical model (dashed line). The blue lines are systems with $v = 0.5$ shown in Fig. 4.3. The red and green lines show the evolution of Φ in a system with 60% higher density. The red lines are calculated for a system with the same size as the blue, while the green lines are calculated for a system twice as large.

corresponding to the largest eigenvalue of the inertia tensor for each cluster of slow particles. As v decreases, $\langle\theta\rangle$ also decreases showing that the clusters in the deposit tend to extend along the y-direction as the velocity difference between particle species increases. The distribution of the angles (inset of Fig. 6) suggests that the number of clusters with small angles increases as v decreases. This is very likely a consequence of the laning phenomenon observed in binary mixtures of species moving at different velocities in region *II* [17].

Although we have not included the effect of particle-particle collisions in the analytical model, the simulation and analytic results are in good agreement for intermediate and low densities. In the limit of high densities, however, the simulation and analytic results differ, as the role of particle-particle interactions is no longer negligible. In Fig. 4.7 we plot the time-dependence of the order parameter for $v = 0.5$ for the system depicted in Fig. 4.3 (in blue) and for a system with a density 60% higher, and two system sizes (red and green). At higher densities the time dependence of the order parameter obtained from Eq. 4.17 is no longer in quantitative agreement with the numerical simulations, and in particular, the maximum is quite different for the green curve.

4.3 Remarks

We investigated the dynamics of sedimentation of a simple binary mixture, and observed purely dynamical demixing.

Hydrodynamic effects are known to have a relevant role in such systems causing, for example, Rayleigh-Taylor like instabilities [6, 98, 99]. However, in our system the two species differ in their Stokes coefficients only, i.e., they have different sedimentation velocities. Since the species travel at different velocities, they demix dynamically as they move towards the bottom of the container in a gravitational field. We measured the degree of demixing using Brownian dynamics simulations for different ratios of the velocities and proposed a simple analytical description in the low density limit. We found that our analytical model captures the dynamics and the degree of segregation in the system even though particle-particle interactions are not considered.

We focused on equimolar binary mixtures but the same demixing mechanism will occur for mixtures with any other composition. In fact, the composition of the deposit is determined by the ratio of the sedimenting fluxes of the two species and, as a result, the initial composition of the mixture will affect the composition of the final deposit. The mechanism described here could also be used to obtain fully mixed deposits, since by tuning v an equimolar deposit may be formed from mixtures poor in one of the two components.

As a final note, we focused on colloidal suspensions but our conclusions can be extended to systems with larger particles, as we considered the limit of high Péclet number, where the dominant mechanism of mass transport is advection and thermal fluctuations are negligible. Since in this limit the relevant mechanisms depend only on the ratio of sedimentation velocities, we expect the same behavior for particles with the same shape but different buoyant masses. The nature of the field is also irrelevant, and thus similar results are to be expected for other (constant) external fields (e.g., electromagnetic field).

Chapter 5

Kinetically controlled structures in multi-component colloidal suspensions

The system studied in the last two chapters is somewhat unrealistic since the species differ in their Stokes coefficients, which implies different hydrodynamic radii, but we do not consider other hydrodynamic interactions. We now move towards a system that can be more easily realized in experiments where different species have different responses to external fields. The segregation found in these types of systems is not a purely dynamical effect anymore since the equilibrium state also favors demixing.

A balance between many-body interactions and external confinement can be exploited to obtain colloidal structures, through self-organization, in a controlled manner. The results that follow show that the structures resulting from the collective dynamics in these systems are usually different from the thermodynamic ones, and thus strongly depend on the kinetics. In this chapter, we consider a binary mixture of particles with distinct mobilities induced by different responses to a inverted Gaussian external potential. Monte Carlo simulations show that the equilibrium state is characterized by particle segregation, with a central region richer on particles with the higher mobility. However, relaxation to the equilibrium state is not always complete since low mobility particles can get trapped in the central cluster if crystallization occurs, what compromises the relaxation equilibrium. We use Brownian Dynamics to investigate the dynamics dependence on the temperature and the field-particle and particle-particle interactions. We use these mechanisms to devise a protocol to avoid kinetically trapped structures and synthesize the thermodynamic ones.

Colloids are very susceptible to external perturbations and, under the right conditions, particles self-assemble into a variety of structures. This makes them very convenient to understand the

mechanisms of collective behavior [97, 100]. By increasing the density crystal-like structures can be formed [101] but several other approaches have been developed to control the assembly of colloids. Among such techniques, patterned templates can be used to grow materials on a surface [102], specific particle shapes or functionalization of the particle surface [70, 103] and using liquid crystals as solvents introduces new interactions that may be taylored to obtain desired structures [104]. External fields are particularly convenient to control the final structure [68] as they do not require detailed manufacturing of other components. In fact, electromagnetic periodic fields have been successfully employed as virtual molds to control the assembly of nano-scale structures with different types of geometries [74]. Here, we aim to control the dynamics to produce new structures that would be unaccessible otherwise.

Suspensions of monodisperse spherical colloidal particles are considered the most elementary system in soft matter since their interactions can be tailored and described by theoretical models with a limited number of free parameters. With a typical size of the order of the micron, they can be observed experimentally using standard optical techniques, what provides the essential ingredients needed to use them as prototypical systems to study the dynamics of many-body systems [105, 106].

We use two different numerical methods to study the system: Monte Carlo (MC) to determine the equilibrium state and Brownian Dynamics (BD) to study the kinetic paths towards the final state. We show that even in such a simple system, the equilibrium state is not accessible in finite times by a straightforward relaxation as the evolution is effectively trapped into a non equilibrium configuration in which crystallization compromises the motion of particles. Experimental results by our collaborators at the University of Gothenburg are in qualitative agreement with the theory. We later devise a protocol that uses dynamically-controlled thermal activation to show that it is possible to control the system kinetics in order to reach the equilibrium state.

5.1 Model and Simulations

We simulate a two-dimensional system with $N = 800$ colloidal particles suspended in a solvent. Particles interact with each other and with an external Gaussian potential. They are equally divided into two species that have different coupling strengths to the external potential but are otherwise identical.

We preformed BD to track the evolution of the system from an initially uniform particle distribution and used MC to calculate the equilibrium configuration. This allows us to compare the final state obtain by BD with the equilibrium state obtained by MC.

5.1.1 Dynamics

Our simulation box is a two-dimensional square domain with side L where the dynamics is overdamped. The pairwise interactions are considered short ranged and described by the repulsive part of a Lennard-Jones potential,

$$V_{pp}(r) = \varepsilon \left[\left(\frac{d_p}{r} \right)^{12} - \left(\frac{d_p}{r} \right)^{6} \right], \tag{5.1}$$

for $r < r_{cut} = 2^{-1/6} d_p$ and $V_{pp}(r) = 0$, otherwise. This potential simulates very strong repulsion at short distances, similar to a hard-sphere interaction without introducing discontinuities in the model.

Particles are coupled to an inverted Gaussian external potential that attracts them to the center of the box

$$V_{ext}(r) = -V_{Ek} e^{-\frac{r^2}{2\sigma^2}}, \tag{5.2}$$

where r is the distance to the center of the box and V_{Ek} is the interaction strength that depends on the particle type k. This is the only parameter that distinguishes the particles that are otherwise identical. We consider two species, strong and weak. The prefactor of strong particles is higher than the weak ($V_{\text{Estrong}} > V_{\text{Eweak}}$) and therefore they have higher mobility. We define the charge ratio (in analogy to a charged system) $R = V_{\text{Estrong}}/V_{\text{Eweak}}$ and we change it by varying V_{Estrong} and fixing $V_{\text{Eweak}} = 1$, which we will use as the units of energy. The width of the potential is given by σ.

The equation of motion of a colloidal particle i in BD is

$$\gamma \frac{d\vec{r}_i}{dt} = -\vec{\nabla}_i \left[\sum_j V_{ij}(r) + V_{ext}(\vec{r}_i) \right] + \vec{\xi}_i, \quad j \neq i \tag{5.3}$$

With T' the thermostat temperature, we define $T = k_B T'$ as the rescaled temperature with units of energy. The characteristic time is defined as $\tau = r_p^2 \gamma / V_{Eweak}$, where $r_p = d_p/2$ is the particle radius. The unit of length is set by r_p.

The initial configuration is a random uniform distribution of particles in the square domain. The simulations stop at $t = 38160\tau$ at which point the system properties do not change significantly with time for the range of parameters studied.

The simulation box side is $L = 150$, the interaction parameter is set to $\varepsilon = 0.15$ and the width of the potential is fixed at $\sigma = 20$ unless stated otherwise.

5.1.2 Equilibrium properties

We performed a Monte Carlo study of the equilibrium configurations and compare it with the results obtained from the BD simulations. We consider two types of MC moves: an increment with a random direction, $\delta\vec{r}$, of the position of a randomly chosen particle with absolute value chosen at random in the interval $|\delta\vec{r}| \in [0, 0.5]r_p$ and a swap of the positions of a pair of particles. These moves are performed on particles chosen randomly and they were repeated $10^4 N$ times. We use the final state provided by BD as the initial configuration of the MC iteration scheme, the reasoning being that this state is, in principle, closer to equilibrium than a uniform distribution of particles over the domain, taking fewer iterations to converge.

5.1.3 Density functional theory of hard disks

We also employed DDFT calculations to study the equilibrium state of the system. We start by writing the Helmholtz free-energy

$$\mathscr{F}[\rho_s, \rho_w] = \mathscr{F}_{id} + \mathscr{F}_{ex}, \tag{5.4}$$

which is divided in two parts, the ideal that takes into account the entropy in the system

$$\mathscr{F}_{id} = \int k_B T \rho_i(\vec{r}) \left[\log\left(\rho_i(\vec{r})\Lambda^2\right) - 1\right] d\vec{r}, \tag{5.5}$$

and the excess, $\mathscr{F}_{ex} = \mathscr{F}_{ext} + \mathscr{F}_{int}$, which includes the interaction with the external potential

$$\mathscr{F}_{ext} = \sum_{i=s,w} \int \rho_i(\vec{r}) V_{ext,i}(\vec{r}) d\vec{r}, \tag{5.6}$$

where

$$V_{ext,i}(r) = -V_{Ei} e^{-\frac{r^2}{2\sigma^2}} \tag{5.7}$$

is an inverted Gaussian potential with the minimum at the center of the domain and r is the distance to this point. V_{Ei} is the parameter that sets the energy scale of the interaction which is different for each particle type i and σ is the width of the potential.

We are interested in the properties of the system as it crystallizes and as such it is not appropriate to use the LDA approximation for the interaction term (see chapter 2) because it neglects fluctuations in the density at the particle scale. The Lennard-Jones potential we used in the particle simulations implies very strong repulsion at short distances which allow us to treat the

particles as hard disks. An approximate expression for the interaction free energy per particle in a system of hard disks is [107]

$$\beta\phi_{int}(\eta) = (c+1)\frac{\eta}{1-\eta} + (c-1)\ln(1-\eta), \tag{5.8}$$

where the constant $c = 7/3 - 4\sqrt{3}/\pi$ and η is the packing fraction $\eta(r) = \rho(r)v_0$ with $v_0 = \pi(d_p/2)^2$ the volume of the particle and d_p the diameter. We note that since the external potential has radial symmetry we can conveniently express the problem in radial coordinates. The interaction term of the free energy becomes

$$\mathscr{F}_{int} = \frac{2}{d_p^2}\sum_{i=s,w}\int r dr \phi_{int}(\eta_i(r))\int_0^{2\pi} d\theta \int_0^{d_p} dr' r' \rho_i(r''), \tag{5.9}$$

where $\vec{r''} = \vec{r} + \vec{r'}$ and hence $r'' = \sqrt{r^2 + r'^2 + 2rr'\cos\theta}$. Finally, the equations of motion for the densities are computed from [49, 50]

$$\gamma\frac{\partial\rho_i(r,t)}{\partial t} = \vec{\nabla}.\left[\rho_i(r,t)\vec{\nabla}\frac{\delta\mathscr{F}[\rho_s,\rho_w]}{\delta\rho_i(r,t)}\right]. \tag{5.10}$$

To solve these equations numerically we use finite differences to calculate the spatial derivatives and the Euler method to integrate in time. To capture the crystallization we need to discretize the space in a fine mesh (of the order of one hundred nodes per particle diameter) [108]. This is a computational heavy operation considering we are working in two dimensions. However, we can take advantage of the fact that the external potential is radial to make an additional approximation and consider that the density is not a function of the angle θ (which is not the case of a crystal periodic structure). We effectively decrease the number of dimensions, to integrate numerically only the radial one. While implementing this algorithm, we found that the calculations were very sensitive to numerical errors at $r = 0$ which renders the solutions numerically unstable before equilibrium is reached.

To circumvent this we considered the purely one dimensional case in a system with hard rods. Under these conditions the free-energy functional becomes [109]

$$\begin{aligned}
&\mathscr{F}[\rho_s,\rho_w] = \\
&\sum_{i=s,w}\int k_B T\rho_i(r)\left[\log\left(\rho_i(r)\Lambda\right)-1\right]dr+ \\
&\sum_{i=s,w}\sum_{j=s,w}\frac{1}{2}\int\left[\rho_i(r-r_p)+\rho_i(r+r_p)\right]\log(1-\eta_j(r))dr+ \\
&\sum_{i=s,w}\int\rho_i(r)V_{ext,i}(r)dr.
\end{aligned} \tag{5.11}$$

We use the exact solution for hard rods in 1D expressed in the second term on the right hand side of Eq. 5.11 where $\eta_j(r)$ is the local packing fraction that is now defined as [109]

$$\eta_j(r) = \int_{r-r_p}^{r+r_p}\rho_j(r)dr. \tag{5.12}$$

Using this functional and Eq.5.10, we were able to describe the evolution of the densities until a crystalline structure is formed. These results are in qualitative agreement with our MC simulations (see appendix A). However, since we had to reduce the equations to 1D we restrict our analysis of the 2D equilibrium state to MC simulations in this chapter.

5.2 Results

Figure 5.1 shows snapshots obtained for different values of the ratio R and thermostat temperature T using MC simulations. The strong particles are colored in red and the weak ones in blue. The properties of the equilibrium state are very much dependent on the set of parameters. For $R = 1$, particles are indistinguishable and the system is completely mixed. For larger R, the equilibrium states demix with the increase of the asymmetry. The configurations are characterized by a central cluster of strong particles surrounded by a ring of weak ones. The increase of temperature induces mixing of the species but it also affects the order of the system. At low temperatures, both the central cluster and ring are in a crystal-like arrangement with hexagonal symmetry, but there are temperatures at which the particles in the ring form a liquid-like state while those in the central cluster keep the crystalline order. At higher temperatures it is possible to prevent crystallization entirely.

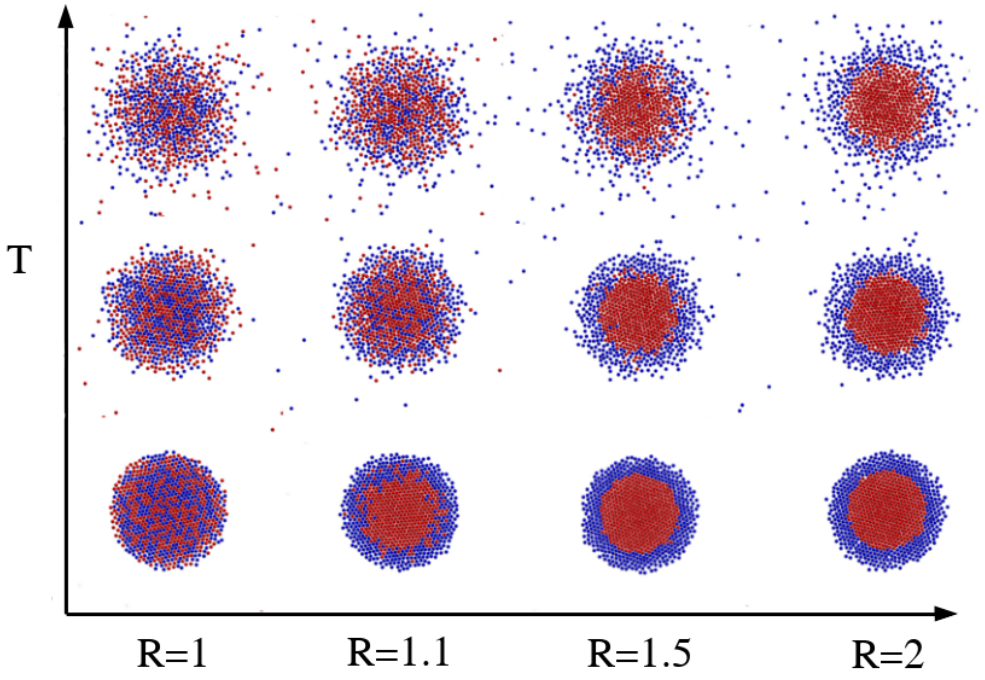

FIGURE 5.1: Equilibrium states obtained from MC simulations for different ratios R and temperatures. Red represents the strong particles and blue the weak.

5.2.1 Effects of the dynamics

We will now discuss the effects of the dynamics on the final state using BD simulations. The starting configuration is a mixed state where particles are uniformly distributed in space around the center. There are two competing mechanisms at play, the short-range repulsive interaction between particles and the interaction with the external potential that has radial symmetry and favors the accumulation of particles in the center of the simulation box. Furthermore, different species respond differently to the external potential. The particles with stronger response to the external potential have higher mobility and therefore, on average, arrive first at the central region. The evolution is divided in two regimes: the accumulation, where particles driven by the external potential form the central cluster, followed by the annealing of the cluster in which thermal diffusion processes play a relevant role.

Figure 5.2 shows snapshots of the system for different times of the BD simulation (first three columns) and for the equilibrium MC (last column). The third column, $t2$, shows the final time of the BD simulations and it is evident that the properties in this state do not correspond to those for thermal equilibrium from the MC simulations. These differences suggest that, the system is trapped in a local energy minimum. The first row shows the local density difference of strong

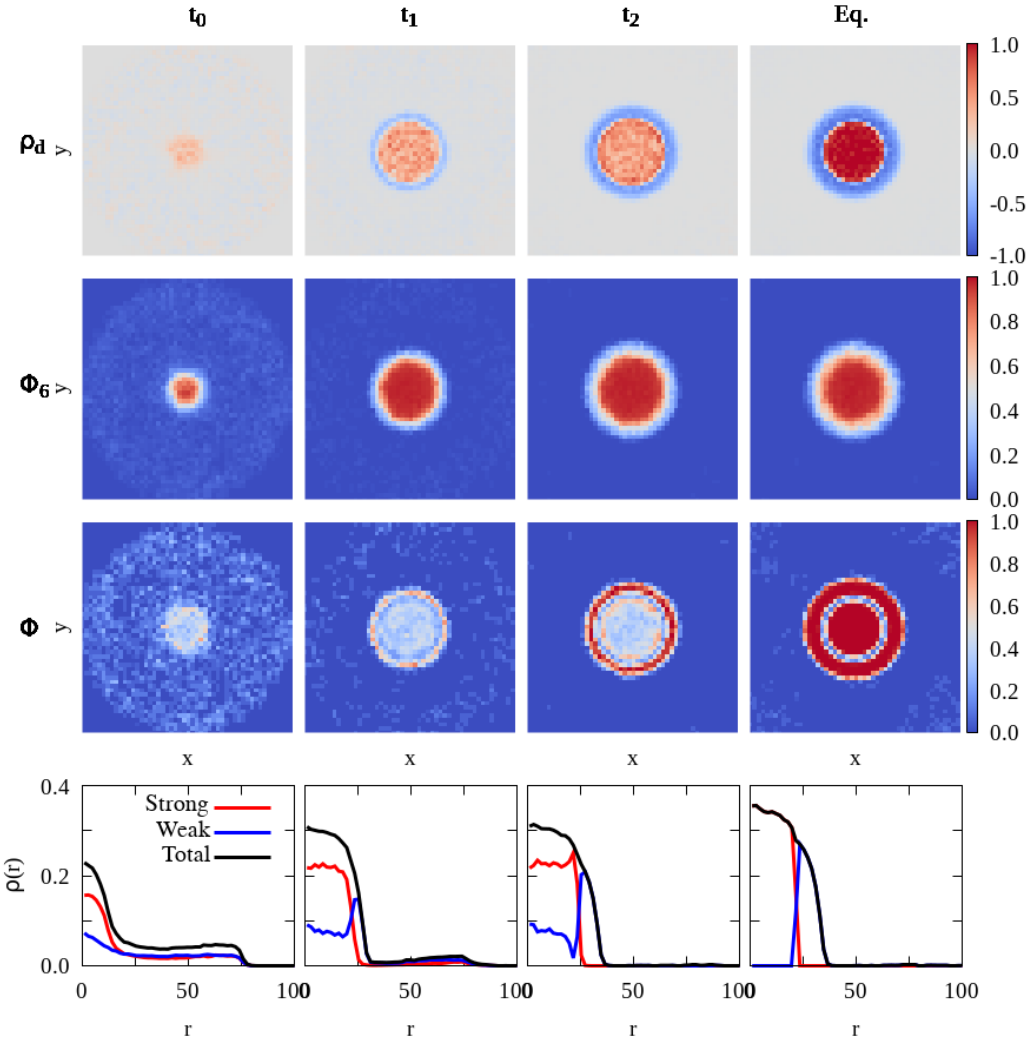

FIGURE 5.2: First three columns show the state of the system given by Brownian Dynamics at different times: $t_0 = 130\tau$, $t_1 = 1600\tau$ and the longest time considered $t_2 = 38160\tau$. The last column shows the equilibrium state obtained from Monte Carlo. First row shows the difference of density particle types, ρ_d at each point in the box. Areas that have an excess of weak particles are represented in blue while the reverse is in red. The second row shows the bond order parameter, ϕ_6, the third is the segregation parameter, ϕ, and the last row shows the density profile, $\rho(r)$. The parameters are: $R = 4$ and $T = 0.013$. The results are averages over twenty samples.

and weak particles

$$\rho_d = \frac{\rho_{\text{strong}} - \rho_{weak}}{\rho_{crystal}}, \tag{5.13}$$

where $\rho_{crystal}$ is the density of the crystal structure. We discretize the box and calculate this parameter locally. In red are the regions with higher density of strong particles and in blue the opposite. We see that from early times there is compositional segregation since the density of

strong particles increases in the center and subsequently there is the formation of a ring of weak particles. At t_2 the center density is not composed by strong particles only, showing that there are weak particles trapped in that region. The second row shows the local bond order parameter

$$\phi_6 = \frac{1}{N_b}\sum_{j}^{N_b} e^{i6\theta_{lj}}, \tag{5.14}$$

defined in the range $[0,1]$. This is unity when there is hexagonal crystal order, the stable crystal configuration in two dimensions. N_b is the number of neighbors within a radius $r = 3$ and θ_{lj} is the angle between $\vec{r}_{lj}$ and a given reference orientation. The red region is the area where there is an hexagonal crystal-like structure, showing that crystallization starts at early times and there are no significant differences between the final BD state and MC results: the central region is crystallized with an outer ring, corresponding to the area with mostly weak particles are present, where the bond order parameter is lower. The third row shows the segregation parameter defined as

$$\phi = \frac{1}{N_b}\sum_{i}^{N_b} \frac{(n_{oi} - n_{li})^2}{(n_{oi} + n_{li})^2}, \tag{5.15}$$

that measures the local segregation. Here, N_b is the number of neighbors within the radius $r = 4$ and n_{li} (n_{oi}) is the number of like (unlike) particles to i within the same radius. Here the differences are significant. The final state provided by the BD shows an irregular area in the center surrounded by a thin ring with large segregation whereas in the equilibrium state there are two separate regions completely segregated. At equilibrium the particles almost completely demix except for a thin interfacial region. The equilibrium configuration is expected to be demixed. The minimum of the external potential for strong particles is lower than for weak particles and since there is a repulsive particle-particle interaction, the weak particles are pushed to the boundary. This is also evident in the last row that shows the density profiles, $\rho(r)$. Although the total density profiles (in black) are very similar in BD and MC, there is a high density of weak particles (in blue) in the central cluster that simply does not exist at equilibrium. While the system is relaxing, weak particles are irreversibly trapped inside the central cluster of strong particles.

Weak particles that are trapped in the crystal-like cluster of strong particles are considered compositional defects since these are only present in the BD and are not observed at equilibrium. However, for $T < 0.026$ some weak particles are crystallized even at equilibrium, see dashed lines in Fig. 5.3 where we define crystallized particles as those with $\phi_6 > 0.95$. These are located in the inner part of the weak ring and should not be considered compositional defects.

We also note from Fig. 5.3 that the number of crystallized particles at equilibrium does not depend on R. The situation is completely different for the BD results. When we consider the entire evolution the percentage of crystallized weak particles has a non-trivial dependence on R that depends on the temperature.

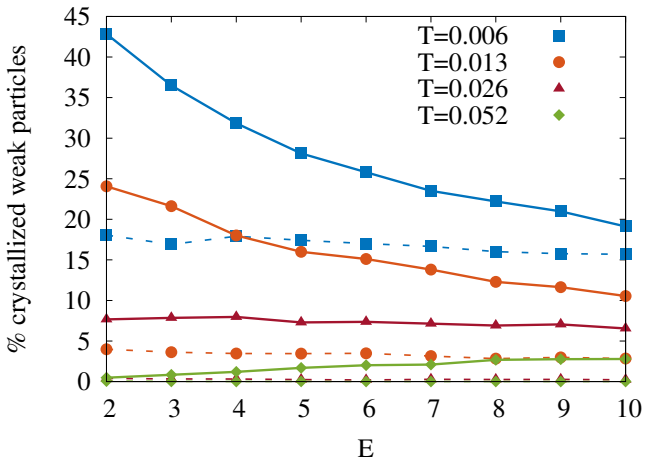

FIGURE 5.3: Percentage of weak particles with $\phi_6 > 0.95$. Dashed lines are the results at equilibrium while solid lines are those obtained from BD.

There is a transition temperature $T \sim 0.026$ below which the number of compositional defects decreases with R and above which it increases. The relaxation exhibits two regimes. In the first, particles accumulate in the center due to the interaction with the external potential causing compositional segregation that is driven by the species different mobilities. A second regime is characterized by the annealing of the cluster where particles are thermally diffuse and strong particles can still make their way towards the center by pushing the weak outwards. If the accumulation time-scale is smaller than the time it takes for weak particles to diffuse in the outwards direction they will get trapped and crystallize. This explains why there is an increase of the number of defects with R at high temperatures. As R increases so does the mobility of strong particles and the accumulation time-scale decreases. At low temperatures, the thermal diffusion decreases and segregation ensues during the accumulation, which increases with R, and there are less compositional defects in the center. At the transition $T \sim 0.026$ the number of defects is not affected by R.

Other than the presence of compositional defects, another factor that characterizes the final state is their distribution in the crystal cluster, which can be measured by the density profile of weak

particles seen in Fig. 5.2. We quantify the distance from equilibrium with the parameter

$$\delta = \frac{\int \left(\rho(r) - \rho_{eq}(r)\right)^2 dr}{\int \rho_{eq}^2(r) dr}, \tag{5.16}$$

where r is the distance to the minimum of the external potential, $\rho(r)$ is the density profile of weak particles and $\rho_{eq}(r)$ is the corresponding density profile at equilibrium. Figure 5.4 shows the deviation from the equilibrium as measured by δ. For $R = 1$, the single component case, δ is zero at all temperatures. In this case, the particles are indistinguishable and there are no compositional defects. In general, δ decreases with the charge ratio and temperature. At higher temperatures, there are only a few particles in the crystal-like cluster as they are dispersed in the liquid-like state over a larger area, decreasing the number of compositional defects and δ. At low temperatures there is a larger cluster where weak particles can be trapped and the increase of R causes a more drastic decrease of δ.

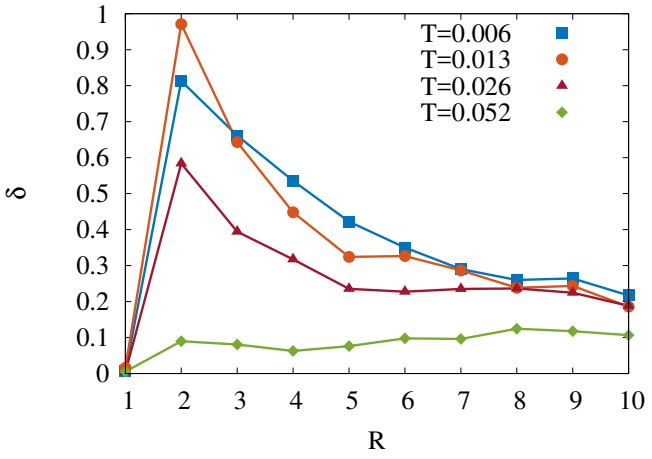

FIGURE 5.4: Deviation from the equilibrium configuration at the end of the BD simulations.

5.3 Comparison with experiments

Figure 5.5 shows the time evolution of some preliminary experiments obtained by our collaborators. The mixture is composed by polystyrene (dark) and silica (light) particles, strong and weak, respectively. The particles are spherical with a radius of $2\mu m$ and are driven by optical tweezers that generates a Gaussian envelope centered with the pictures. There is a mismatch between the index of refraction of the particles and that of the medium (water) that induces a force towards the higher intensity of the optical field. The charge ratio between the colloids is

estimated to be $R \sim 2$. Particles that are initially uniformly distributed start moving towards the center of the Gaussian envelope with different velocities depending on the species. The temperature is low enough for crystallization to occur. As the cluster grows in time weak particles get trapped inside the crystal-like cluster. In the last picture, a ring of weak particles at the boundary of the cluster is starting to form but experiments that are longer in time are needed to check if a full ring develops.

The experiments seem to reveal an excess of compositional defects when compared with the equilibrium states from the MC simulations for $R = 2$ where the particles form a crystal-like structure. This indicates that the kinetic pathways lead to trapped non-equilibrium states where weak particles form compositional defects in the central cluster, as predicted by our BD simulations. Since there is crystallization the system will not be able to relax towards equilibrium in finite times and the defects are effectively frozen.

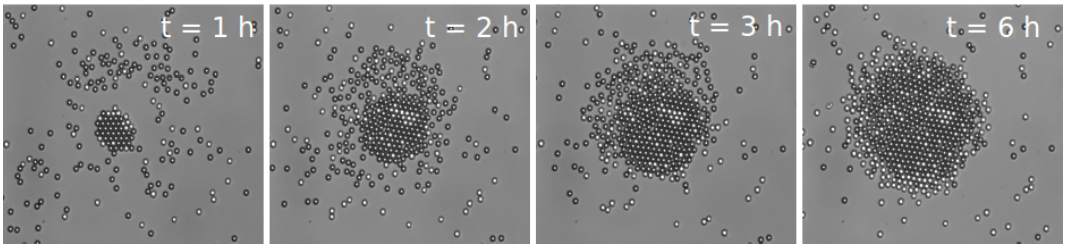

FIGURE 5.5: Experiment with a mixture of colloidal particles driven by an optical field. The pictures show the evolution (from left to right) of a binary system of polystyrene (dark) and silica (light) particles under a Gaussian potential.

5.4 Protocol

In the previous sections, we have shown that the final state achieved by relaxation under an external potential does not correspond to the equilibrium state but that a high ratio of responses favors a final state with fewer compositional defects and lower δ. We also saw that thermal fluctuations help to reduce the number of defects in the crystalline structure. In this section, we propose a protocol to decrease the number of defects in an efficient way by changing the shape of the external potential with time. The density induced crystallization starts in the center of the cluster and the crystal grows radially. Annealing is only observed at the cluster boundary as it expands. Complete segregation is obtained if the crystallization time-scale is longer than the time it takes weak particles to diffuse away from the central region. A way to promote this is by tuning the width of the Gaussian external potential with time. We start with a narrow potential

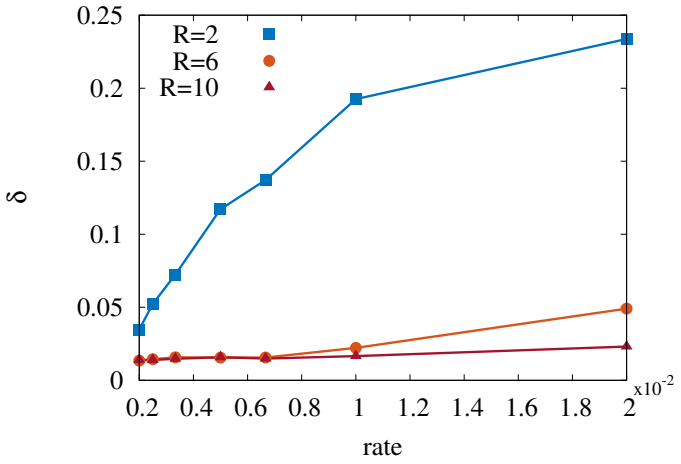

FIGURE 5.6: δ measures the difference between the equilibrium density profile (obtained by MC) and the one reached through the time evolution (obtained by BD). The proposed protocol preforms better for small rates of change of the potential for which the final state is close to equilibrium. Results are shown for $T = 0.026$.

with width $\sigma = 5$ and increase it after $t = 636$ with different rates, $\frac{\Delta\sigma}{\Delta t}$, until $\sigma = 20$. The results in Fig.5.6 are for $T = 0.026$, a temperature high enough to observe thermal fluctuations at the boundaries of the cluster but sufficiently low to form a crystal in the center. Overall, δ is much smaller (it can decrease up to 90%) with the dynamic potential than with the static one (Fig.5.4). Lower rates of width increase achieve the best results but for high R, δ does not change significantly with the rate. Figure 5.7 shows that the percentage of weak particles trapped in the cluster decreases significantly by using the protocol and that the results are better for lower rates. The proposed protocol may reduce up to 99% the number of compositional defects in the cluster.

5.5 Remarks

We showed that binary mixtures get easily trapped in non-equilibrium configurations where compositional defects are present. This needs to be taken into consideration when assembling many body structures driven by external potentials, where it is often assumed that the relaxation reaches equilibrium. Moreover, in a system where particles have different mobilities, we quantified the presence of defects for different charge ratios and temperatures and compared those results with the completely segregated equilibrium state to find that, in general, higher charge ratios and temperatures favor final states that have fewer compositional defects and lower δ.

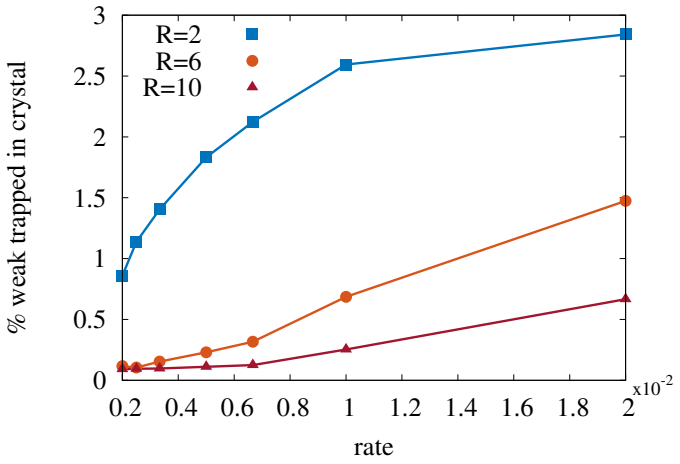

FIGURE 5.7: Percentage of weak particles trapped in the crystal cluster of strong particles. The proposed protocol decreases the number of compositional defects in the system for every ratio R. Results are shown for $T = 0.026$.

We identified two mechanisms for segregation. The first happens when particles are accumulating around the minimum of the external potential and a compositional segregation occurs because strong particles arrive first on average followed by the weak ones. The second mechanism happens at the boundaries of the cluster where thermal fluctuations are higher and annealing takes place. It is energetically favorable for strong particles to be closer to the center and this can only occur when their movement is not constrained by neighboring particles.

Finally, we devised a protocol to prevent the formation of trapped states. We have shown that it is possible to increase the annealing time-scale by dynamically changing the shape of the external potential. In this way, particles slowly anneal before they crystallize through the increase of the density. This is a simple protocol that is a proof of concept to fabricate dynamically controlled structures.

Chapter 6

Ordering of Binary Colloidal Crystals by Random Potentials

Structural defects are ubiquitous in condensed matter, and not always a nuisance. For example, they underlie phenomena such as Anderson localization and hyperuniformity, and they are now being exploited to engineer novel materials. Here, we show that the density of structural defects in a 2D binary colloidal crystal can be engineered with a random potential. We generate the random potential, whose forces act strongly on one species of particles (strong particles) and weakly on the other (weak particles). Thus, the strong particles are more attracted to the randomly distributed local minima of the potential, leaving a trail of defects in the crystalline structure of the colloidal crystal. While, as expected, the crystalline ordering initially decreases with increasing fraction of strong particles, the crystalline order is surprisingly recovered for sufficiently large fractions. We combine particle-based simulations and experimental results, which permit us to elucidate how this non-monotonic behavior results from the competition between the particle-potential and particle-particle interactions.

Perfect crystalline structures are not commonly found in Nature, because, even in the absence of impurities, structural defects occur spontaneously and disrupt the periodicity of the crystalline lattice [110]. For example, when a melt is cooled down, multiple crystallites grow with degenerate orientations [111]. Since the coarsening time of these crystallites diverges with size, structural defects appear and prevent the emergence of global order [112, 113]. While the existence of these defects is a challenge when growing single crystals, it can also be an opportunity when engineering the properties of materials; indeed, control over defects enables the development of solid-state devices with fine-tuned mechanical resilience, optical properties, and heat and electrical conductivity [114–118]. In atomic crystals, engineering structural defects is

an experimental challenge for two reasons [119]: first, current visualization techniques at the atomic scale do not provide a high spatial or time resolution [120, 121]; second, no current technique can control the density of defects in a systematic manner [122]. The first challenge can be overcome studying colloidal crystals as models for atomic systems [123, 124], where colloidal particles can be individually tracked using standard digital video microscopy techniques [68, 125, 126], and have in fact also been used to study crystallisation and melting of colloidal crystals in the presence of extended laser fields [127, 128]. Here, we demonstrate that the second challenge can be solved combining a binary colloidal mixture and a random potential that can be generated in experiments with an optical laser. This permits us to control the density of structural defects in the resulting 2D colloidal crystal and to explore a surprising non-monotonic behavior of their ordering and stability.

6.1 Simulations

We performed BD simulations of a binary mixture of $N = 800$ particles with several compositions, on a two-dimensional square box with linear size L. The particle species differ in the strength of their response to the potential. The interaction potential between a pair of particles i and j with diameter d_p is independent of the species and is given by the repulsive part of a Lennard-Jones potential:

$$V_{ij}(r) = \varepsilon \left[\left(\frac{d_p}{r} \right)^{12} - \left(\frac{d_p}{r} \right)^{6} \right], \tag{6.1}$$

where ε sets the energy scale. This is a very steep and short-ranged potential that only affects neighbouring particles within a cut-off distance of $r_{\text{cut}} = 2^{-1/6} d_p$.

The external potential has two contributions. The first contribution is a Gaussian potential that attracts the particles towards the centre of the simulation box, given by

$$V_{\text{Gaussian}}(r) = \begin{cases} -V_{\text{G}_k} e^{-\frac{(r-7.5)^2}{\sigma_{\text{G}}^2}} & \text{if } r > 7.5 \\ 0 & \text{if } r \leq 7.5 \end{cases} \tag{6.2}$$

where σ_{G} is the width of the Gaussian and V_{G_k} sets the scale of this interaction, which depends on the particle type k; the interaction V_{G_k} with the most responsive (strong) particles is $2\times$ that with the least responsive (weak) ones; r is the distance to the centre of the simulation box. By definition, we ensure that the Gaussian potential is zero in the central region of the box, of radius

7.5, where we carried out the statistical analysis of the system. This potential is used to confine the particles in the centre of the box at sufficiently high densities.
The second contribution, V, to the external potential reproduces the potential that, in experiments, can be generated by a speckle pattern produced by lasers [51]. We used the Fourier filtering method (FFM) to generate numerically random potentials with Gaussian spatial correlations [52, 53]. The FFM takes advantage of the fact that the correlation function of a field $E(\vec{r})$, is the inverse Fourier transform of the absolute value of its Fourier coefficients, $|E_{\vec{k}}|^2$, as stated by the Wiener-Khinchin theorem [54]. This relation allows us to sample random Fourier coefficients that when transformed back into real space describe a random potential with the desired spatial correlations. The depths of those potentials have a Gaussian distribution. To convert this into an exponential distribution, as measured for the speckle, we proposed the procedure described in chapter 2. The forces due to this potential are then calculated using finite differences. In all simulations, we considered Gaussian correlations with a dispersion σ. When $\sigma < d_{\mathrm{p}}$ (where d_{p} is the diameter of the particles) the speckle features vary on distances shorter than the particle size and we need to consider an effective speckle pattern that is the result of the integration of the speckle intensities over the particle volume (see below the section "Effective speckle properties"). The results presented in Figs. 1 and 2 were achieved with $\sigma = 0.4$. The potentials strength ratio is $V_{\mathrm{G}}/V = 1$ in the simulations presented in Figs. 6.4, 6.12, 6.13, 6.10.
The motion of a particle i in the surrounding medium is described by the overdamped Langevin equation

$$\gamma \frac{d\vec{r}_i}{dt} = -\vec{\nabla}_i \left[\sum_j V_{ij}(r) + V_{\mathrm{ext}}(\vec{r}_i) \right] + \vec{\xi}_i. \quad j \neq i, \tag{6.3}$$

The characteristic time is defined as $\tau = d_p^2 \gamma / k_{\mathrm{B}} T$. We set the diameter of the particle, d_{p}, as the unit length, the simulation box has linear size $L = 50$ and the width of the external Gaussian potential is $\sigma_{\mathrm{G}} = L/2$. The energy is given in units of $k_{\mathrm{B}}T$ with $\varepsilon = 10$ and $V_{\mathrm{G}} = 200$. The simulations were run for $2 \times 10^4 \tau$ and the data used in the calculations was taken in the last $1.5 \times 10^3 \tau$, when the evolution was found to be in the stationary state in the centre of the box. For all data points, we used 100 samples to average the relevant quantities.

6.2 Speckle properties

The speckle can be regarded as a two dimensional random landscape of intensities with two different statistical properties. Namely, the values of the intensity are exponentially distributed

and the spatial correlations are Gaussian distributed. The speckle intensity peaks correspond to the minima of the potential and these are the points to which the particles are attracted.
We are interested in the limit where the dispersion in the speckle correlation function, σ, is of the same order as the particle size or smaller. Thus, to calculate the speckle-induced forces acting on a particle, we need to consider all the intensities over the particle's cross-section. We can determine an effective speckle that, at each point, is the average intensity of the original speckle over a particle cross-section. This operation, smooths out the roughness of the original surface and the optical forces decrease. This effect can be seen in Fig. 6.1, where it is clearly shown that the integration over the particle cross-section decreases the height of the intensity maxima and increases the intensity minima.

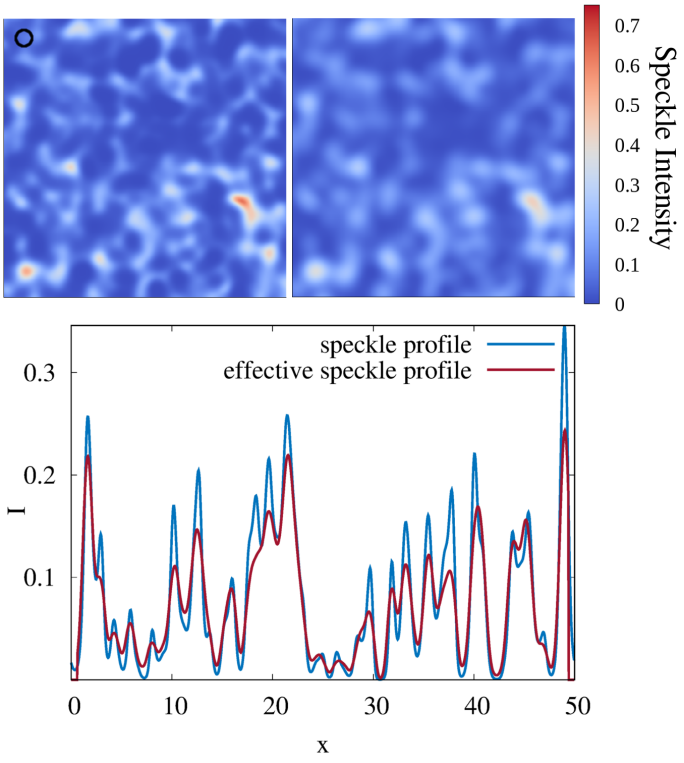

FIGURE 6.1: Top left, the original speckle intensity surface; the black circle indicates the particle size. Top right, the effective speckle where each intensity point is an average of the intensities of the original one. Bottom, profile of the intensity surface of the original (blue) and the effective speckle (red) for $\sigma = 0.5$. The maximum speckle intensity is defined as the unit of intensity.

The statistical properties of the effective speckle are different from those of the original one. Figure 6.2 shows a comparison between the intensity distributions for different σ (histograms) and the original one (dashed line). For high σ, the averaging eliminates the highest intensities but hardly affects the distribution otherwise, as it remains approximately exponential. However,

for lower σ, both high and low intensities are eliminated and the distribution is considerably affected. For the lowest σ, the intensities are narrowly distributed around a well-defined value.

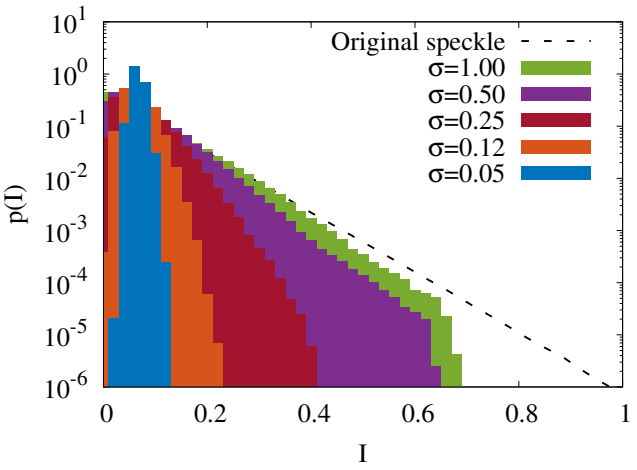

FIGURE 6.2: Distribution of the speckle intensities of the effective speckles. 100 samples were used for each distribution. The dashed line corresponds to the original intensity distribution, for reference. The maximum speckle intensity is defined as the unit of intensity.

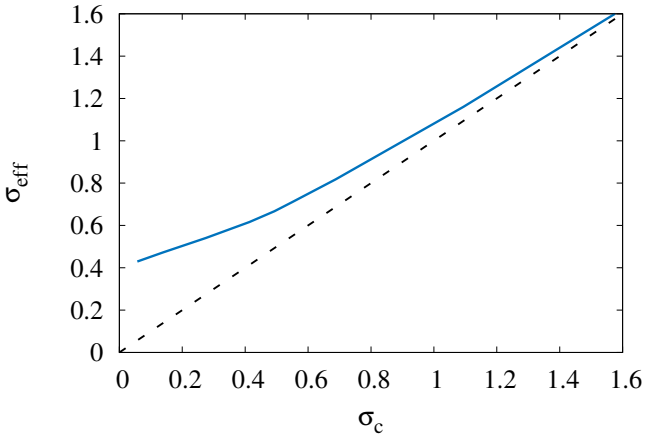

FIGURE 6.3: Relation between the dispersion of the speckle correlation function in the original speckle and the corresponding dispersion measured in the effective speckle.

The shape of the Gaussian intensity correlations also changes with the averaging. In particular, their dispersions increase. Figure 6.3 shows the dispersion of the correlations in the effective speckle, σ_{eff}, as a function of the standard deviation of the original speckle, σ. The dashed line corresponds to $\sigma_{\text{eff}} = \sigma$. For higher σ, the averaging does not change the dispersion significantly, because in this limit the features of the surface are, on average, larger than the particle size. For decreasing σ, σ_{eff} increases with respect to the original value, the speckle minima

become wider and shallower, which leads to a lower effective force induced by the speckle on the particles.

6.3 Structure deformation

We start with a low concentration of particles and switch on the optical potential. The particles are attracted towards its center by the Gaussian envelope. Strong particles $2\times$ more responsive to the external potential than the weak ones. It then becomes possible for them to be pinned by the speckle while weak particles are weakly coupled. When only weak particles are present ($\chi = 0$), they eventually form a compact structure with hexagonal order, as shown in Fig. 6.4 (i). When we introduce strong particles, these get trapped in the local minima of the disordered potential and introduce defects that reduce the hexagonal order. Already with only 20% of strong particles ($\chi = 0.2$), the presence of structural defects is clearly visible (see Fig. 6.4 (ii)). The impact is even more pronounced when 50% of the particles ($\chi = 0.5$) are strongly interacting with the potential (Fig. 6.4 (iii)). Thus, strong particles act as defects in the crystalline structure of the weak ones, compromising global order. As we will see in more detail below, we can control the density of defects by adjusting χ as well as the intensity and grain size of the pattern. To quantify the order of the crystalline structure, we measure the six-fold bond-order parameter, $\langle\phi_6\rangle$, defined as [13]

$$\langle\phi_6\rangle = \frac{1}{6N_c}\sum_{l}^{N_\mathrm{c}}\left|\sum_{j}^{N_\mathrm{b}} e^{i6\theta_{lj}}\right|, \tag{6.4}$$

where the outer sum is over the N_c particles within 7.5 particle diameters from the center of the potential (which is the area shown in Fig. 6.4 where the aggregate is formed), the inner sum is over the N_b neighbors of a particle in the Voronoi tessellation, and θ_{lj} is the angle between the x-axis and the line connecting the centers of particles j and l. $\langle\phi_6\rangle = 1$ for perfect hexagonal crystals (in practice, it is never exactly one, because of thermal fluctuations and other transient perturbations to the periodic order) and it decreases with the number of structural defects.
The bottom panel of Fig. 6.4 shows $\langle\phi_6\rangle$ obtained numerically as a function of the molar fraction χ. For $\chi = 0$, $\langle\phi_6\rangle \approx 1$, consistent with the formation of an hexagonal periodic structure. As expected, as χ increases, the value of $\langle\phi_6\rangle$ decreases due to the formation of structural defects. The data shows that, surprisingly, $\langle\phi_6\rangle$ reaches a minimum value for $\chi_{\min} \approx 0.6$, and then the global order increases for $\chi > \chi_{\min}$. In particular, for $\chi = 1$, the bond order parameter approaches unity despite the presence of the random potential. This observations suggests a

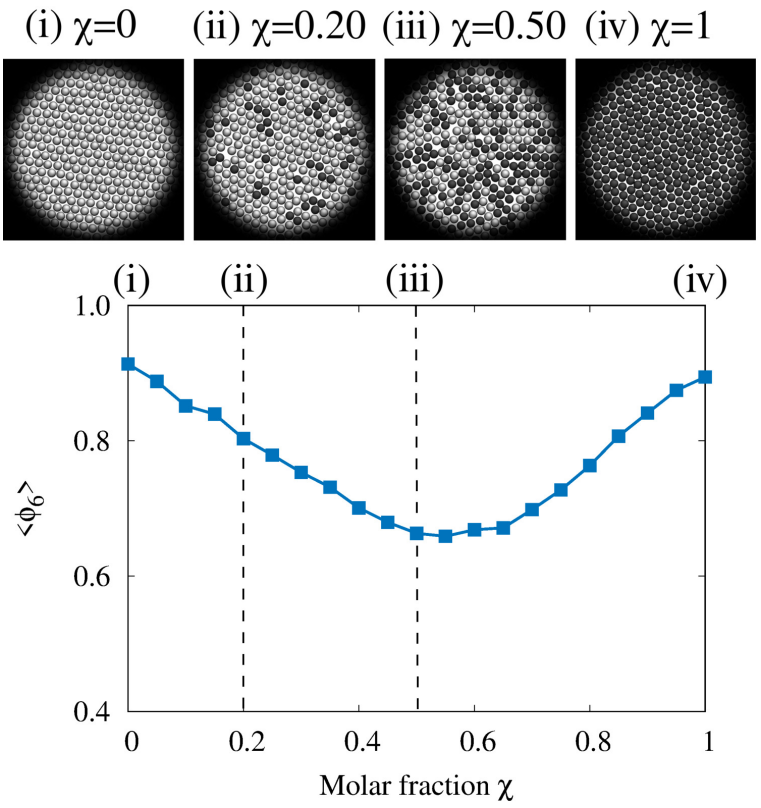

FIGURE 6.4: Crystalline order for different molar fractions of strong particles. Six-fold bond order parameter $\langle\phi_6\rangle$ as a function of the molar fraction χ (squares; the blue line connects the symbols for visual guidance). These numerical results are averages over 100 samples. The top snapshots show the final configurations in the simulations for $\chi = 0$, 0.2, 0.5, and 1.

change in the effective interaction between the strong particles and the random potential: from one that favors disorder at a low χ to one favoring order at larger χ.

A non-monotonic dependence of the six-fold bond order parameter as a function of χ is also observed at higher densities. In Fig. 6.5 we show the bond order parameter in a system with 25% more particles than the simulations shown in the rest of the paper. Even at higher densities the curve displays a clear minimum and the rearrangement of the structure for higher molar fractions also occurs, showing that this phenomenon is robust to considerable changes in the total density.

In colloidal suspensions the particle-particle interactions can also have longer ranges. A charged particle in suspension interacts with the free charges in the fluid in which case the net balance is described by a Yukawa potential

$$V_{ij}(r) = \varepsilon \frac{\exp\left(-\frac{r-d_p}{d_p}\right)}{r-d_p}. \tag{6.5}$$

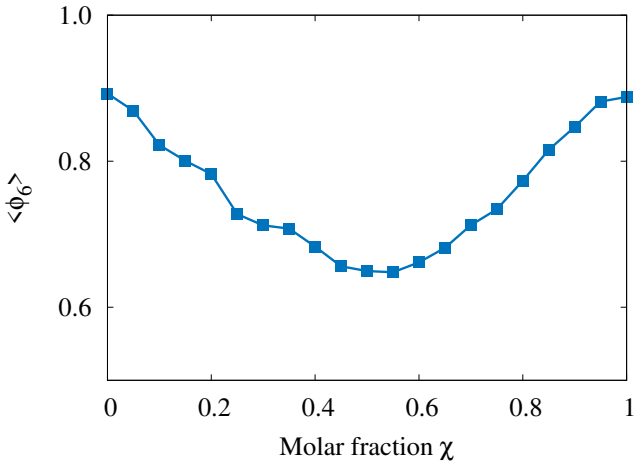

FIGURE 6.5: Bond order parameter at higher densities also displays a minimum. Parameters: $\sigma = 0.5$, $V = 11.3$ and $V_G/V = 0.67$.

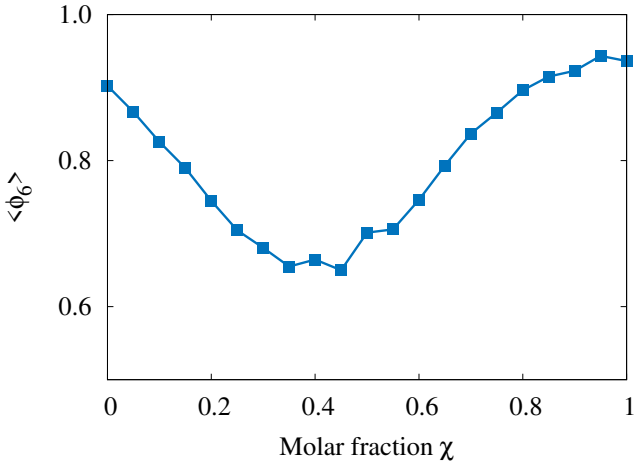

FIGURE 6.6: Bond order parameter in a system where particle-particle interactions are modeled by a Yukawa potential. Parameters: $\sigma = 0.5$, $V = 11.3$ and $V_G/V = 2$.

To show that the non-monotonic dependence of the bond order parameter on the molar fraction of strong particles is a robust result that does not depend on the details of the interactions between particles we performed additional simulations where we modeled the particle-particle interaction with a Yukawa potential. As shown in the Fig. 6.6, we obtained the same qualitative result. Note that in these simulations the ratio of the response to the external potentials of the strong and weak particles is four.

6.4 Effects of the local dynamics

In order to elucidate the microscopic mechanisms underlying this behavior, we employ trajectories obtained by BD simulations to study the effective interactions between the two particle species and the local minima of the speckle potential. Figure 6.7(a) shows some trajectories of weak (light gray) and strong (dark gray) particles at various χ. We performed these simulations using a random potential without the Gaussian envelope to highlight the effective interactions between the particles and the local minima of the speckle.

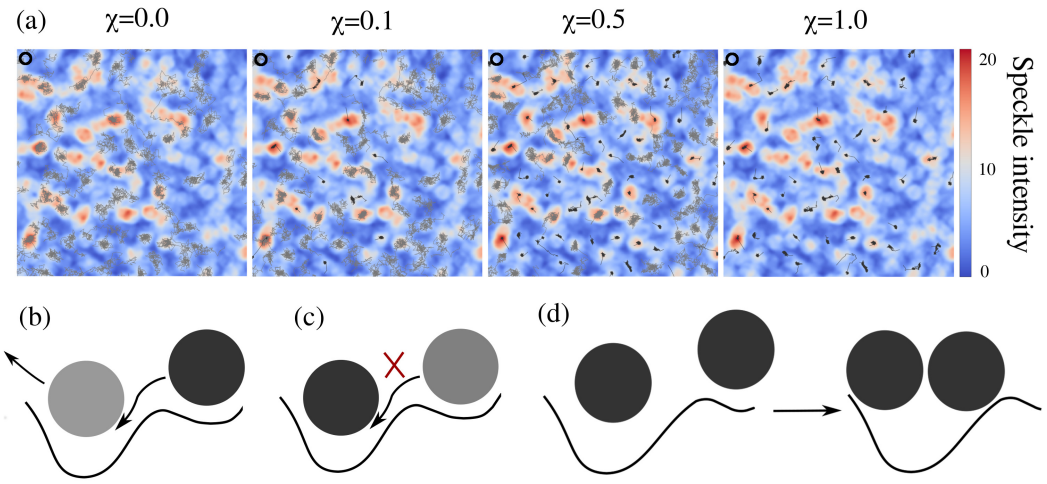

FIGURE 6.7: Local dynamics of the effective interaction between the particles and minima of the random potential. (a) Examples of trajectories of weak (light gray) and strong (dark gray) particles in the presence of a speckle obtained numerically for different values of the molar fraction χ. The particle density is $10\times$ lower than that of maximal packing and the Gaussian envelope is absent. The four simulations were preformed under exactly the same conditions, including the same sequence of random numbers for the thermostat. The black circles on the top left corner indicate the particle size. The random potential intensities are in units of $k_B T$ and σ is one particle diameter. (b) When a weak particle (light gray) is located at a potential minimum and a strong particle (dark gray) is in its vicinity, it is energetically favorable to exchange the two, but the opposite process (c) is not. (d) The free energy may be significantly reduced when two particles of the same species share the same potential minimum.

In all cases, the weak particles can hop between minima, while the strong particles get readily trapped in them; in fact, the effective diffusion coefficient of the strong particles is significantly lower than that of the weak particles as shown in Fig. 6.8 where we measured the particle's mean square displacement at late times in the simulations ($t > 1.5 \times 10^3 \tau$) and estimated the diffusion coefficient, D, from a linear fit of the time dependence of the mean square displacement.

At low χ in fig. 6.7a, the strong particles quickly populate the minima that are sufficiently deep to prevent their escape and remain there for the entire simulation time, as this configuration is

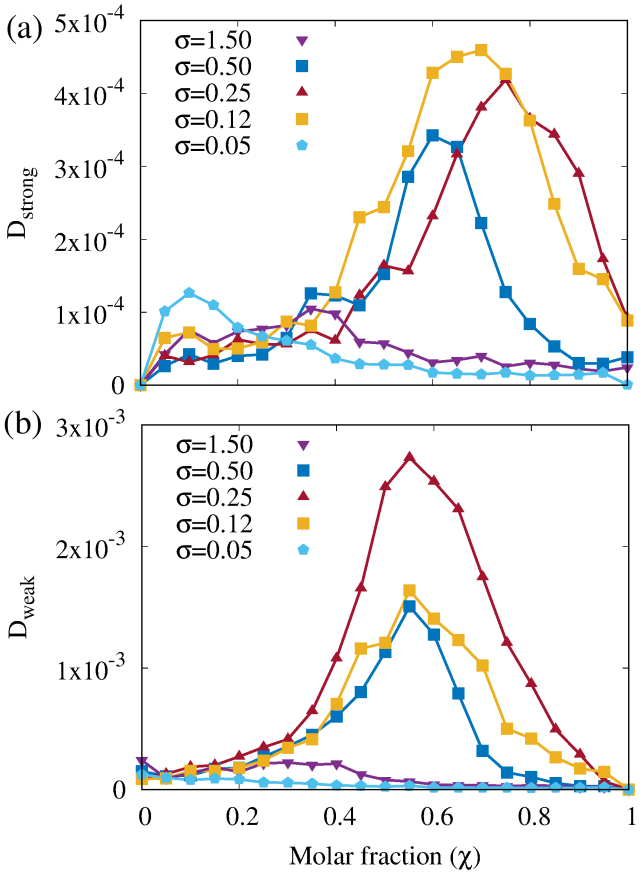

FIGURE 6.8: (a) Strong and (b) weak particle diffusivity at late times in the same simulations as those shown in Fig. 6.10. The diffusivity is in units of $d_p^2\tau^{-1}$.

energetically favorable (Figs. 6.7b and 6.7c); therefore, the number of spatial defects increases monotonically with the number of trapped strong particles, leading to a decrease of $\langle\phi_6\rangle$ with increasing χ. At large χ, the number of strong particles is greater than the number of potential minima and thus it becomes energetically favorable to have more than one strong particle in one minimum (Figs. 6.7d). This allows the spatial rearrangement of the particles. Since the energy of the interaction with the speckle is no longer strong enough to localize the particles, a large scale crystalline structure is favorable, consistent with the increase in $\langle\phi_6\rangle$ observed in Fig. 6.13. When $\chi = 1$, all particles are strong and thus the hexagonal crystalline structure is recovered. We counted also the number of strong and weak particles located in minima of the random potential as a function of χ. As shown in Fig. 6.9, the minima are mainly populated by strong particles and the average number of particles in each minimum is larger than one for values of χ above that where the six-fold bond order parameter is minimal. To compute this calculation, we set a threshold to define the boundaries of the speckle minima at 15% of the maximum intensity.

Note that since the intensities are exponentially distributed the total area of the regions we are correspond to $\sim 20\%$ of the area of the system (we tried different thresholds and the results are qualitatively the same). The total number of particles averaged over 100 samples remains constant as a function of the molar fraction and there are, on average, more than one particle in the regions defined by the threshold.

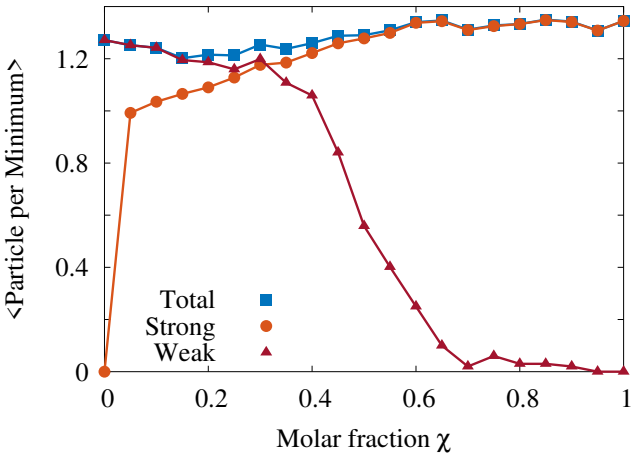

FIGURE 6.9: Number of particles per speckle peak as a function of the molar fraction in simulations. The total number of particles is represented by the blues line, the strong particles by the orange line and the weak by the red line. These results were obtained from the simulations shown in Fig. 6.4.

6.5 Tuning the parameters of the speckle

In order to investigate the robustness of the non-monotonic dependence of $\langle\phi_6\rangle$ on χ, we studied numerically its dependence on the properties of the underlying speckle pattern. The speckle is characterized by a strength V corresponding to the average potential depth (in units of $k_B T$, where k_B is the Boltzmann constant and T is the absolute temperature of the sample) and by a spatial correlation σ (in units of the particle diameter), which corresponds to the average grain size. Figure 6.10(a) shows $\langle\phi_6\rangle$ for different V. Although the curves in the range $1.51 < V \leqslant 18.8$ feature one minimum, its position and intensity vary with V: the number of minima that can trap particles is expected to increase with V. Thus, the fraction of particles that can be trapped also increases and the corresponding value of $\chi_{\min}$ shifts to the right while the minimum becomes deeper. For $V > 18.8$, the behaviour seems to become independent of the molar fraction (and always disordered), because the weak particles are also effectively trapped.

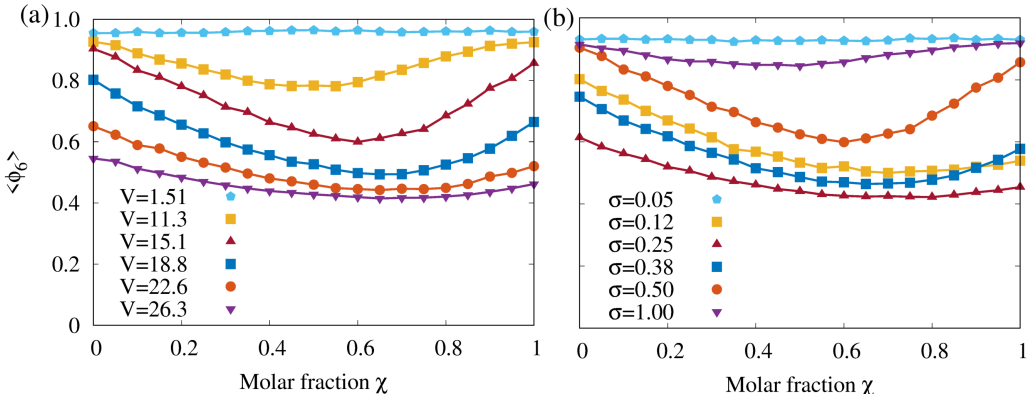

FIGURE 6.10: Dependence of the order parameter on the speckle properties. Six-fold bond order parameter as a function of the molar fraction (χ) obtained numerically, for different values of the speckle (a) strength and (b) spatial correlation σ. Results in (a) were obtained for $\sigma = 0.5$ and in (b) for $V = 15.1$, and are averages over 100 samples.

Figure 6.10(b) shows $\langle\phi_6\rangle$ for different values of σ. A pronounced minimum is only observed for intermediate values of σ, close to unity (particle diameter). If $\sigma \gg 0.5$ or $\sigma \ll 0.5$, the optical forces are negligible for different reasons: for $\sigma \gg 0.5$, the gradient of the optical potential is very small on the scale of the particle; and for $\sigma \ll 0.5$, the optical potential varies on a length scale smaller than the particle size and thus its gradient averages to zero over the particle cross-section (see Fig. 6.1). In the latter case, the optical force on a particle is the sum of the contributions over the particle's cross-section, which can be described by the effective random potential that differs from the one originally applied (see Fig. 6.2 and 6.3).

6.6 Experimental system

The experiments done by our collaborators (S. Velu, I. Kasianiuk, D. Kasyaniuk, A. Callegari, G. Volpe and G. Volpe [38]) were preformed with a binary colloidal suspension of equally-sized polystyrene (refractive index $n_{ps} \approx 1.59$) and silica ($n_{si} \approx 1.42$) spherical particles with diameters $d_{PS} = 6.24 \pm 0.22\,\mu$m and $d_{Si} = 6.73 \pm 0.22\,\mu$m, respectively (see appendix B.1 for details on the sample preparation and appendix B.2 on the experimental setup). To characterize the composition of the mixture, we use the molar fraction of polystyrene particles defined as $\chi = N_{ps}/N_t$ where N_{ps} is the number of polystyrene particles and N_t is the total number of particles. We let these particles sediment at the bottom surface of a homemade sample chamber so that they are effectively confined in a quasi-2D space (see appendix B.3 for more details).

A speckle pattern is generated by mode-mixing a laser beam in a multimode optical fibre (see Fig. B.1) [51, 129, 130]. Speckle patterns form rough, disordered optical potentials characterized by wells whose depths are exponentially distributed and whose average width is given by diffraction (here, average grain size $\sigma = 2.7 \pm 0.2$ μm).
Furthermore, the fibre imposes a Gaussian envelope (beam waist $\sigma_G = 72.5 \pm 0.2$ μm) to the speckle pattern, which attracts the particles towards the center of the speckle pattern effectively confining them in space. Since the optical forces acting on the particles increase for larger mismatches between their refractive index and that of the surrounding medium (here water, $n_w \approx 1.33$) [131], the optical forces acting on the polystyrene (strong) particles are about $2\times$ higher than those exerted on silica (weak) particles as we show in the appendix B.6).

6.7 Particle-particle interactions

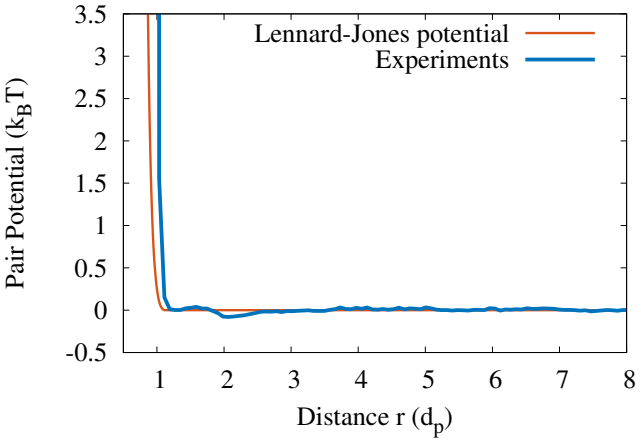

FIGURE 6.11: Effective interaction potential between pairs of particles in experiments (blue) and the Lennard-Jones potential used in the simulations. The potential is in units of k_BT and the distance r in units of the particle diameter.

We followed the procedure to calculate the pairwise potential between particles in experiments based on the two-point correlation function described in Ref. [132]. As shown in Fig. 6.11, the interactions are essentially repulsive and the potential decays rapidly with the distance, being negligible for values of the distance close to the diameter of the particle. This suggest that, for particles of the size considered here, the interactions are well described by hard-sphere potentials. To avoid the classical numerical problems of dealing with hard spheres (and discontinuous forces) in the simulations, we considered a Lennard-Jones potential that also decays rapidly as described in section 6.1.

6.8 Comparison between theory and experiments

The results in Figs. 6.12 show that both simulations and experiments are in good qualitative agreement. Strong particles act as defects in the crystalline structure of the weak ones, compromising global order for low molar fractions. In the experiments, the deformation of the structure was not caused by particle bidispersity since when subject only to a Gaussian envelope the particles formed a crystalline structure independently of the number of strong particles present (see appendix B.5).

Figure 6.13 shows $\langle\phi_6\rangle$ obtained numerically (blue squares) and experimentally (orange circles) as a function of the molar fraction χ. The $\langle\phi_6\rangle$ also displays a minimum in the experiments as predicted in our simulations, with the recovery of the crystalline structure for $\chi = 1$. Although we do not consider all the fine details from the physical system in our simulations, we were able to predict the correct $\langle\phi_6\rangle$ dependence showing that this is a robust result.

The snapshots in the top rows of Fig. 6.13 show the final configurations (first row), the corresponding Voronoi tessellations (second row), and the spatial Fourier transform (third row), for different values of χ. The results from the simulations are corroborated by the Voronoi tessellation of the final configurations and by the respective spatial Fourier transforms. From this analysis, we can see that the number of Voronoi cells with a number of neighbors different from six becomes higher near the minimum of $\langle\phi_6\rangle$, even though the Voronoi-cell size in both experiments and simulations does not vary significantly compared with the particle size (see

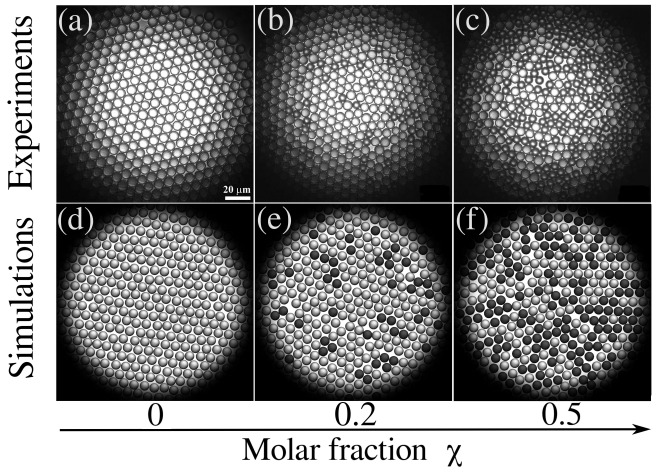

FIGURE 6.12: Colloidal crystals with tunable degree of disorder. Final configurations obtained in (a-c) experiments and (d-f) simulations, for different molar fractions χ of strong particles. The weak (silica) particles are light gray, and the strong (polystyrene) particles are dark gray. The illumination for the images is delivered by an optical fibre which produces the vignetting effect observed in the experimental images.

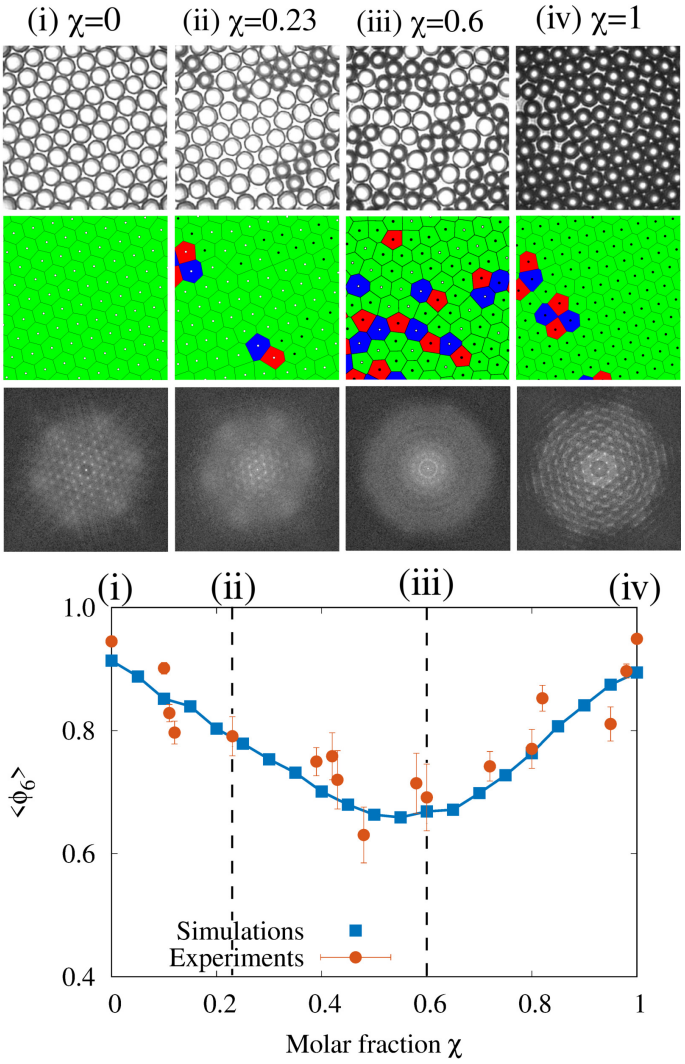

FIGURE 6.13: Crystalline order for different molar fractions of strong particles. Six-fold bond order parameter $\langle\phi_6\rangle$ as a function of the molar fraction χ obtained experimentally (circles) and numerically (squares; the blue line connects the symbols for visual guidance). The error bars show the standard deviation of ϕ_6 over 500 frames in the stationary state of the experiments (i.e., after 30 minutes from the start of the experiments). The numerical results are averages over 100 samples. The top snapshots show the final configurations in the experiments (first row), the Voronoi tessellation (second row), and the spatial Fourier transform (third row) for $\chi = 0$, 0.23, 0.6, and 1. The filled (empty) circles at the center of the Voronoi cells indicate strong (weak) particles. The cells are colored by the number of nearest neighbors, namely, equal (green), lower (red), greater (blue) than six.

Fig. 6.14). Also, The Fourier transforms display dimmer intensity peaks near the minimum of $\langle\phi_6\rangle$.

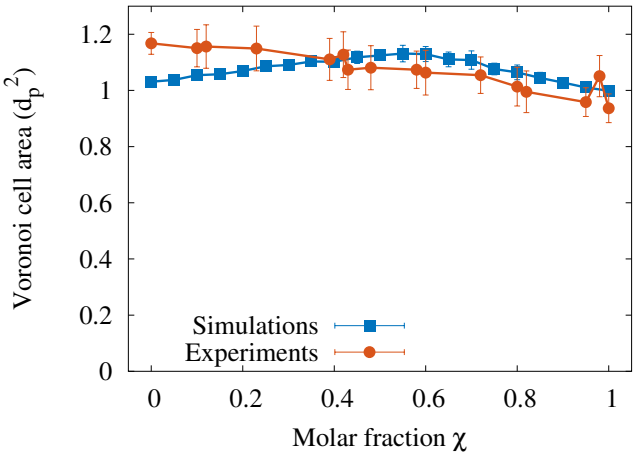

FIGURE 6.14: Average Voronoi cell area from the experiments (orange circles) and the simulations (blue squares) in Fig. 6.13.

6.9 Orientational correlations and the hexatic phase

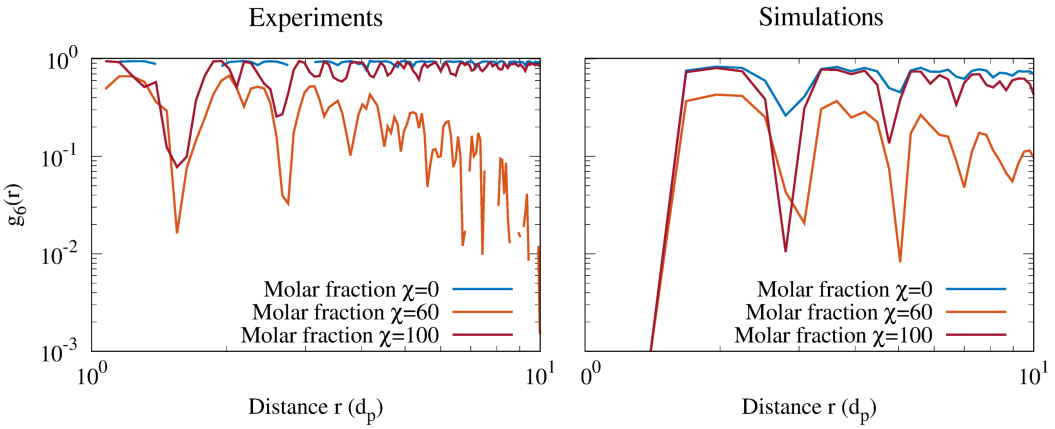

FIGURE 6.15: Orientation correlations, $g_6(r)$, in experiments (left panel) and simulations (right panel) for different fractions of strong particles.

According to Kosterlitz, Thouless, Halperin, Nelson and Young (KTHNY) theory [133–136], two-dimensional colloidal solid phases are characterized by long-range orientational order and quasi-long-range positional order, characterized by a constant bond orientation correlation function, $g_6(r) = \langle \phi_6^*(r_i)\phi_6(r_j)\delta(r-r_{ij})\rangle$ (with r_i the position of particle i and r_{ij} the distance between particles i and j), and a radial pair correlation function, $g(r) = \langle \delta(r-r_{ij})\rangle$, that decays as a power law with the distance [137, 138]. In this phase dislocations are bound in pairs. By contrast, the hexatic phase is characterized by quasi-long-range orientation order and short-range positional order, with an orientation correlation function that decays as a power law and

a pair correlation function that decays exponentially. In the solid-hexatic transition, the unbinding of dislocations occurs. The melting is complete with a second phase transition where the dislocations decompose into free disclinations forming an isotropic liquid with short-range orientational and positional order.
To study the phase behavior of our system, we computed the bond orientation correlation function, $g_6(r)$ shown in Fig.e 6.15. Both the experimental and numerical results suggest an hexatic phase close to the minimum of the six-fold bond order parameter and a solid phase at lower and higher values of the molar fraction. Note that, the spatial range considered here is limited by the confining potential to a maximum distance of $10\times$ times the particle diameter. We cannot discard the possibility of quasi-long-range orientation order for values of the distance larger than this value, as reported in Ref. [138].

6.10 Remarks

In conclusion, we have shown that the order in a two-dimensional binary colloidal crystal can be controlled by an underlying random optical potential, while previous studies [127, 128] have shown how freezing and melting are influenced by the intensity of the laser field and the particle density. We employ a disordered potential and a binary mixture where some particles interact strongly with the substrate and others weakly. This permits us to study a system where disorder and impurities are present, which is highly relevant for applications. Since the intensity of the optical forces depends on the mismatch of the indices of refraction of the particles and the surrounding medium, the particles with the larger index mismatch are more responsive (strong particles) than those with the lower mismatch (weak particles). For the parameters of the optical potential that were considered, only the strong particles respond significantly to the potential. Thus, strong particles tend to occupy the minima of the potential and nucleate structural defects in the, otherwise, periodic hexagonal structure of the weak particles. The density of defects is controlled by the fraction of strong particles and the statistical properties of the underlying potential. When the number of strong particles increases beyond the number of local minima that can trap them, the trapping mechanism becomes less effective and the hexagonal order is recovered as the fraction of strong particles increases. Here, we have considered a random optical potential with Gaussian spatial correlations and with a characteristic length given by the standard deviation σ. However, it is technically possible to generate other optical potentials, e.g. periodic [131] or with different spatial correlations [139, 140]. Thus, one can control not only the density of defects, but also their spatial distribution. Time-varying optical potentials

could also be employed to change the position of strong particles and defects in time, affecting the overall dynamics [126, 129, 141]. Understanding how the spatial distribution of defects influences the physical properties of materials is a question of both scientific curiosity and technological interest that can now be addressed in a systematic way.

Chapter 7

Conclusions

The dynamics of colloidal particles in solution results from a balance between the interactions with other particles (and external fields) and the resistance of the suspending medium to the motion of the particle (described by the Stokes coefficient). In mixtures of colloidal particles, each species will respond differently to these fields, leading to a rich dynamics between them. To shed light on the dynamics of mixtures, we considered two types of system: two particle species that differ in their 1) Stokes coefficient and 2) response to external fields. We showed that the kinetic pathways determine the final configurations, which are not always the equilibrium ones. In fact, binary mixtures with many particles get easily trapped in kinetically arrested states for long periods of time. This opens the way to use the dynamics to control the self-assembly.

In the first type of system the equilibrium configuration is characterized by a completely mixed state since the energy landscape is the same for both species. However, the degree of mixing present in the system can be tuned with the ratio between the Stokes coefficients, which in effect controls the ratio between the hydrodynamic radii of the particles and the velocity at which they travel. The dynamics can be explored as a means to achieve segregated states that are transient. It is possible to extend the life time of these transient states by decreasing the temperature and allowing the crystallization. This represents an opportunity to demix mixtures but can also become a nuisance if the goal is to reach equilibrium, in which case understanding the mechanisms at play is essential to avoid the arrested states.

We studied the effects this type of segregation in the sedimentation of mixtures under a gravitational field. The fact that the species have different sedimentation velocities affects the particle distribution in the deposit. It is not only possible to control the dynamics but also the level of segregation with the ratio between the velocities. Moreover, the shape of the clusters of particles in the deposit is also affected by the laning of particles as they fall under gravity.

By contrast, the equilibrium state in second type of system is completely demixed when subject to a inverted Gaussian potential. The energy landscape differs for each species which induces the assembly of a central cluster of strong particles surrounded by a ring of weak particles. We find that there are two mechanisms for the segregation: one is compositional and induced by the fact that particles travel at different velocities; and the other is thermal diffusion and occurs in the regions of low density. However, we are also faced here with the formation of arrested states characterized by the presence of weak particles trapped in the central cluster of strong particles. We are able to improve the efficiency to which the equilibrium state is reached by dynamically changing the shape of the external potential with the effect of increasing the annealing time-scale.

We devised a method to systematically control the number of structural defects in a system with strong and weak particles using random potentials. This effort was done in collaboration with a group performing experiments and the theoretical results that guided the experiments were shown to describe them quantitatively. We consider an initially uniformly distributed mixture evolve subject to a confining and to a random potential. We showed that the deformation of the crystalline structure depends non-trivially on the number of strong particles present in the system. We found that there is an intermediate ratio of strong and weak particles that maximizes the number of defects, when the monodisperse species is crystalline. The intensity of the random potential as well as the average width of the randomly distributed minima can also be used to control the presence of structural defects. The regime that enhances the deformation the most is when the minima of the random potential are deep enough to trap strong particles but not weak ones.

We have identified key features that drive the dynamics in binary mixtures of colloids that, at the collective scale, give origin to emergent order or disorder. We showed that, through the dynamics, it is possible to control the properties of structures such as the level of mixing or the number of structural defects. Our results are robust and do not depend on the fine details of the systems which opens the way for comparison of our models with experiments aimed at identifying new non-equilibrium structures.

Bibliography

[1] M. E. Ibele, P. E. Lammert, V. H. Crespi, and A. Sen. Emergent, collective oscillations of self-mobile particles and patterned surfaces under redox conditions. *ACS Nano*, 4: 4845–4851, 2010.

[2] F. Schmidt, B. Liebchen, H. Löwen, and G. Volpe. Light-controlled assembly of active colloidal molecules. *J. Chem. Phys.*, 150:094905, 2019.

[3] G. Falkovich and N. Vladimirova. Turbulence appearance and nonappearance in thin fluid layers. *Phys. Rev. Lett.*, 121:164501, 2018.

[4] R. C. V. Coelho, N. A. M. Araújo, and M. M. Telo da Gama. Active nematic-isotropic interfaces in channels. *Soft Matter*, 15:6819–6829, 2019.

[5] D. Helbing. Self-organization in pedestrian crowds. In *Understanding Complex Systems*, pages 71–99. Springer Berlin Heidelberg, 2012.

[6] A. Wysocki, C. P. Royall, R. G. Winkler, G. Gompper, H. Tanaka, A. van Blaaderen, and H. Löwen. Direct observation of hydrodynamic instabilities in a driven non-uniform colloidal dispersion. *Soft Matter*, 5:1340–1344, 2009.

[7] N. A. M. Araújo, D. A. Zezyulin, V. V. Konotop, and M. M. Telo da Gama. Dynamic design of spatial patterns of colloidal suspensions. *Langmuir*, 33:11698–11702, 2017.

[8] L. Cademartiri and K. J. M. Bishop. Programmable self-assembly. *Nat. Mater.*, 14:2–9, 2014.

[9] V. N. Manoharan. Colloidal matter: Packing, geometry, and entropy. *Science*, 349: 1253751–1253751, 2015.

[10] M. H. Lash, M. V. Fedorchak, J. J. McCarthy, and S. R. Little. Scaling up self-assembly: bottom-up approaches to macroscopic particle organization. *Soft Matter*, 11:5597–5609, 2015.

[11] S. Sacanna, D. J. Pine, and G. R. Yi. Engineering shape: the novel geometries of colloidal self-assembly. *Soft Matter*, 9:8096, 2013.

[12] M. A. Boles, M. Engel, and D. V. Talapin. Self-assembly of colloidal nanocrystals: From intricate structures to functional materials. *Chem. Rev.*, 116:11220–11289, 2016.

[13] A. S. Nunes, A. Gupta, N. A. M. Araújo, and M. M. Telo da Gama. Field-driven dynamical demixing of binary mixtures. *Mol. Phys.*, 116:3224, 2018.

[14] A. M. Georgoulaki, L. V. Ntouros, D. P. Tassios, and A. Z. Panagiotopoulos. Phase equilibria of binary lennard-jones mixtures: simulation and van der waals l-fluid theory. *Fluid Phase Equilib.*, 100:153–170, 1994.

[15] J.V.L. Singer and K. Singer. Monte carlo calculation of thermodynamic properties of binary mixtures of lennard-jones (12-6) liquids. *Mol. Phys.*, 24:357–390, 1972.

[16] S. M. Cattes, S. H. L. Klapp, and M. Schoen. Condensation, demixing, and orientational ordering of magnetic colloidal suspensions. *Phys. Rev. E*, 91:052127, 2015.

[17] M. Rex and H. Löwen. Lane formation in oppositely charged colloids driven by an electric field: Chaining and two-dimensional crystallization. *Phys. Rev. E*, 75:051402, 2007.

[18] J. Dzubiella and H. Löwen. Pattern formation in driven colloidal mixtures: tilted driving forces and re-entrant crystal freezing. *J. Phys. Condens. Matter*, 14:9383–9395, 2002.

[19] T. Vissers, A. van Blaaderen, and A. Imhof. Band formation in mixtures of oppositely charged colloids driven by an ac electric field. *Phys. Rev. Lett.*, 106:228303, 2011.

[20] A. Nikoubashman, N. A. Mahynski, A. H. Pirayandeh, and A. Z. Panagiotopoulos. Flow-induced demixing of polymer-colloid mixtures in microfluidic channels. *J. Chem. Phys.*, 140:094903, 2014.

[21] C. Edington, H. Murata, R. Koepsel, J. Andersen, S. Eom, T. Kanade, A. C. Balazs, G. Kolmakov, C. Kline, D. McKeel, Z. Liron, and A. J. Russell. Tailoring the trajectory of cell rolling with cytotactic surfaces. *Langmuir*, 27:15345–15351, 2011.

[22] C. Wang and Y. Otani. Removal of nanoparticles from gas streams by fibrous filters: A review. *Ind. Eng. Chem. Res.*, 52:5–17, 2012.

[23] M. Auset, A. A. Keller, F. Brissaud, and V. Lazarova. Intermittent filtration of bacteria and colloids in porous media. *Water Resour. Res.*, 41, 2005.

[24] M. E. Warkiani, B. L. Khoo, L. Wu, A. K. P. Tay, A. A. S Bhagat, J. Han, and C. T. Lim. Ultra-fast, label-free isolation of circulating tumor cells from blood using spiral microfluidics. *Nat. Protoc.*, 11:134–148, 2015.

[25] D. Di Carlo, J. F. Edd, K. J. Humphry, H. A. Stone, and M. Toner. Particle segregation and dynamics in confined flows. *Phys. Rev. Lett.*, 102:094503, 2009.

[26] O. Scheibelhofer, N. Balak, P. R. Wahl, D. M. Koller, B. J. Glasser, and J. G. Khinast. Monitoring blending of pharmaceutical powders with multipoint nir spectroscopy. *AAPS PharmSciTech*, 14:234–244, 2013.

[27] A. Z. M. Abouzeid and D. W. Fuerstenau. Mixing–demixing of particulate solids in rotating drums. *Int. J. Miner. Process.*, 95:40–46, 2010.

[28] N. Takeishi and Y. Imai. Capture of microparticles by bolus flow of red blood cells in capillaries. *Sci. Rep.*, 7:5381, 2017.

[29] L. L. Munn and M. M. Dupin. Blood cell interactions and segregation in flow. *Ann. Biomed. Eng.*, 36:534–544, 2008.

[30] E. G. Noya and E. Bianchi. Phase behaviour of inverse patchy colloids: effect of the model parameters. *J. Phys. Condens. Matter*, 27:234103, 2015.

[31] E. Zaccarelli. Colloidal gels: equilibrium and non-equilibrium routes. *J. Phys. Condens. Matter*, 19:323101, 2007.

[32] C. Mayer, E. Zaccarelli, E. Stiakakis, C. N. Likos, F. Sciortino, A. Munam, M. Gauthier, N. Hadjichristidis, H. Iatrou, P. Tartaglia, H. Löwen, and D. Vlassopoulos. Asymmetric caging in soft colloidal mixtures. *Nat. Mater.*, 7:780–784, 2008.

[33] S. M. Ilett, A. Orrock, W. C. K. Poon, and P. N. Pusey. Phase behavior of a model colloid-polymer mixture. *Phys. Rev. E*, 51:1344–1352, 1995.

[34] J. T. Padding and A. A. Louis. Hydrodynamic interactions and brownian forces in colloidal suspensions: Coarse-graining over time and length scales. *Phys. Rev. E*, 74: 031402, 2006.

[35] A. S. Nunes, V. C. Braz, M. M. da Gama, and N. A. M. Araújo. Dynamical demixing of a binary mixture under sedimentation. *arXiv:1807.10265*, 2018.

[36] J.D. Joannopoulos, P. R. Villeneuve, and S. Fan. Photonic crystals. *Solid State Commun.*, 102:165–173, 1997.

[37] Y. Wang, I. C. Jenkins, J. T. McGinley, T. Sinno, and J. C. Crocker. Colloidal crystals with diamond symmetry at optical lengthscales. *Nat. Commun.*, 8:14173, 2017.

[38] A. S. Nunes, S. K. P. Velu, I. Kasianiuk, D. Kasyanyuk, A. Callegari, G. Volpe, M. M. Telo da Gama, G. Volpe, and N. A. M. Araújo. Ordering of binary colloidal crystals by random potentials. *arXiv:1903.01579*, 2019.

[39] A. Satoh. *Introduction to Practice of Molecular Simulation: Molecular Dynamics, Monte Carlo, Brownian Dynamics, Lattice Boltzmann and Dissipative Particle Dynamics.* Elsevier Insights, 2010.

[40] G. K. Batchelor. *An Introduction to Fluid Dynamics.* Cambridge University Press, 2000.

[41] H. Risken. *The Fokker-Planck Equation. Methods of Solution and Applications.* Springer-Verlag, 1996.

[42] M. P. Allen and D. J. Tildesley. *Computer Simulation of Liquids*. Clarendon Press, 1989.

[43] B. Derjaguin and L. Landau. Theory of the stability of strongly charged lyophobic sols and of the adhesion of strongly charged particles in solutions of electrolytes. *Acta Physico Chemica URSS*, 14:30–59, 1941.

[44] E. J. W. Verwey and J. Th. G. Overbeek. *Theory of the stability of lyophobic colloids*. Elsevier, 1948.

[45] A. C. Brańka and D. M. Heyes. Algorithms for brownian dynamics computer simulations: Multivariable case. *Phys. Rev. E*, 60:2381–2387, 1999.

[46] R. Evans. The nature of the liquid-vapour interface and other topics in the statistical mechanics of non-uniform, classical fluids. *Adv. Phys.*, 28:143–200, 1979.

[47] J. F. Lutsko. Recent developments in classical density functional theory. In *Adv. Chem. Phys.*, pages 1–92. John Wiley & Sons, Inc., 2010.

[48] J. Landers, G. Y. Gor, and A. V. Neimark. Density functional theory methods for characterization of porous materials. *Colloid. Surf. A Physicochem. Eng. Asp.*, 437:3–32, 2013.

[49] U. M. B. Marconi and P. Tarazona. Dynamic density functional theory of fluids. *J. Chem. Phys.*, 110:8032–8044, 1999.

[50] M. Rauscher. Ddft for brownian particles and hydrodynamics. *J. Phys. Condens. Matter*, 22:364109, 2010.

[51] G. Volpe, G. Volpe, and S. Gigan. Brownian motion in a speckle light field: tunable anomalous diffusion and selective optical manipulation. *Sci. Rep.*, 4:3936, 2014.

[52] H. A. Makse, S. Havlin, M. Schwartz, and H. E. Stanley. Method for generating long-range correlations for large systems. *Phys. Rev. E*, 53:5445, 1996.

[53] E. A. Oliveira, K. J. Schrenk, N. A. M. Araújo, H. J. Herrmann, and J. S. Andrade. Optimal-path cracks in correlated and uncorrelated lattices. *Phys. Rev. E*, 83:046113, 2011.

[54] H. O. Peitgen and D. Saupe, editors. *The Science of Fractal Images*. Springer-Verlag New York, Inc., 1988.

[55] G. M. Whitesides and B. Grzybowski. Self-assembly at all scales. *Science*, 295:2418–2421, 2002.

[56] P. J. Lu and D. A. Weitz. Colloidal particles: Crystals, glasses, and gels. *Annu. Rev. Condens. Matter Phys.*, 4:217–233, 2013.

[57] J. C. Everts, N. Boon, and R. van Roij. Density-induced reentrant melting of colloidal wigner crystals. *Phys. Chem. Chem. Phys.*, 18:5211–5218, 2016.

[58] Y. L. Wu, D. Derks, A. van Blaaderen, and A. Imhof. Melting and crystallization of colloidal hard-sphere suspensions under shear. *Proc. Natl. Acad. Sci.*, 106:10564–10569, 2009.

[59] T. K. Haxton, L. O. Hedges, and S. Whitelam. Crystallization and arrest mechanisms of model colloids. *Soft Matter*, 11:9307–9320, 2015.

[60] H. W. Hatch, W. P. Krekelberg, S. D. Hudson, and V. K. Shen. Depletion-driven crystallization of cubic colloids sedimented on a surface. *J. Chem. Phys.*, 144:194902, 2016.

[61] A. van Blaaderen, R. Ruel, and P. Wiltzius. Template-directed colloidal crystallization. *Nature*, 385:321, 1997.

[62] A. Cadilhe, N. A. M. Araújo, and V. Privman. Random sequential adsorption: from continuum to lattice and pre-patterned substrates. *J. Phys. Condens. Matter*, 19:065124, 2007.

[63] I. B. Ramsteiner, K. E. Jensen, D. A. Weitz, and F. Spaepen. Experimental observation of the crystallization of hard-sphere colloidal particles by sedimentation onto flat and patterned surfaces. *Phys. Rev. E*, 79:011403, 2009.

[64] D. Joshi, D. Bargteil, A. Caciagli, J. Burelbach, Z. Xing, A. S. Nunes, D. E. P. Pinto, N. A. M. Araújo, J. Brujic, and E. Eiser. Kinetic control of the coverage of oil droplets by dna-functionalized colloids. *Sci. Adv.*, 2:e1600881, 2016.

[65] Y. Wang, Y. Wang, D. R. Breed, V. N. Manoharan, L. Feng, A. D. Hollingsworth, M. Weck, and D. J. Pine. Colloids with valence and specific directional bonding. *Nature*, 491:51, 2012.

[66] R. Bianchi, E.and Blaak and C. N. Likos. Patchy colloids: state of the art and perspectives. *Phys. Chem. Chem. Phys.*, 13:6397–6410, 2011.

[67] N. A. M. Araújo, C. S. Dias, and M. M. Telo da Gama. Nonequilibrium self-organization of colloidal particles on substrates: adsorption, relaxation, and annealing. *J. Phys.: Condens. Matter*, 29:014001, 2017.

[68] A. S. Nunes, N. A. M. Araújo, and M. M. Telo da Gama. Self-assembly of colloidal bands driven by a periodic external field. *J. Chem. Phys.*, 144:034902, 2016.

[69] H. L owen. Colloidal dispersions in external fields: recent developments. *J. Phys. Condens. Matter*, 20:404201, 2008.

[70] C. S. Dias, N. A. M Araújo, and M. M. Telo da Gama. Mixtures of functionalized colloids on substrates. *J. Chem. Phys.*, 139:154903, 2013.

[71] C. Bechinger, R. Di Leonardo, H. Löwen, C. Reichhardt, and G. Volpe, G.and Volpe. Active particles in complex and crowded environments. *Rev. Mod. Phys.*, 88:045006, 2016.

[72] S. N. Weber, C. A. Weber, and E. Frey. Binary mixtures of particles with different diffusivities demix. *Phys. Rev. Lett.*, 116:058301, 2016.

[73] S. Kumari, A. S. Nunes, N. A. M. Araújo, and M. M. Telo da Gama. Demixing of active particles in the presence of external fields. *J. Chem. Phys.*, 147:174702, 2017.

[74] A. F. Demirörs, P. P. Pillai, B. Kowalczyk, and B. A. Grzybowski. Colloidal assembly directed by virtual magnetic moulds. *Nature*, 503:99–103, 2013.

[75] COMSOL Multiphysics Software is used to implement the FEM.

[76] R. Piazza. Settled and unsettled issues in particle settling. *Rep. Prog. Phys.*, 77:056602, 2014.

[77] E. C. Cho, Q. Zhang, and Y. Xia. The effect of sedimentation and diffusion on cellular uptake of gold nanoparticles. *Nat. Nanotechnol.*, 6:385, 2011.

[78] J. M. Park, J. Y Lee, J. G. Lee, H. Jeong, J. M. Oh, Y. J. Kim, D. Park, M. S. Kim, H. J. Lee, J. H. Oh, S. S. Lee, W. Y. Lee, and N. Huh. Highly efficient assay of circulating tumor cells by selective sedimentation with a density gradient medium and microfiltration from whole blood. *Anal. Chem.*, 84:7400, 2012.

[79] T. L. Yoder, H. Zheng, P. Todd, and L. A. Staehelin. Amyloplast sedimentation dynamics in maize columella cells support a new model for the gravity-sensing apparatus of roots. *Plant Physiol.*, 125:1045, 2001.

[80] Peter S. On the analysis of protein self-association by sedimentation velocity analytical ultracentrifugation. *Anal. Biochem.*, 320:104 – 124, 2003.

[81] C. R. Smith, P. A. Jumars, and D. J. DeMaster. In situ studies of megafaunal mounds indicate rapid sediment turnover and community response at the deep-sea floor. *Nature*, 323:251, 1986.

[82] J. C. Knox. Floodplain sedimentation in the upper mississippi valley: Natural versus human accelerated. *Geomorphology*, 79:286, 2006.

[83] C. Holz, J. W. Stuut, and R. Henrich. Terrigenous sedimentation processes along the continental margin off nw africa: implications from grain-size analysis of seabed sediments. *Sedimentology*, 51:1145, 2004.

[84] J. L. Cole, J. W. Lary, T. Moody, and T. M. Laue. Analytical ultracentrifugation: Sedimentation velocity and sedimentation equilibrium. *Methods Cell Biol.*, 84:143, 2008.

[85] J. Lebowitz, M. S. Lewis, and P. Schuck. Modern analytical ultracentrifugation in protein science: A tutorial review. *Protein Sci.*, 11:2067, 2002.

[86] R. Piazza, T. Bellini, and V. Degiorgio. Equilibrium sedimentation profiles of screened charged colloids: A test of the hard-sphere equation of state. *Phys. Rev. Lett.*, 71:4267, 1993.

[87] S. Buzzaccaro, A. Tripodi, R. Rusconi, D. Vigolo, and R. Piazza. Kinetics of sedimentation in colloidal suspensions. *J. Phys.: Condens. Matter*, 20:494219, 2008.

[88] G. K. Batchelor and R. W. Janse Van Rensburg. Structure formation in bidisperse sedimentation. *J. Fluid Mech.*, 166:379, 1986.

[89] D. de las Heras and M. Schmidt. The phase stacking diagram of colloidal mixtures under gravity. *Soft Matter*, 9:8636, 2013.

[90] M. Rasa and A. P. Philipse. Evidence for a macroscopic electric field in the sedimentation profiles of charged colloids. *Nature*, 429:857, 2004.

[91] D. de las Heras, J. M. Tavares, and M. M. Telo da Gama. Bicontinuous and mixed gels in binary mixtures of patchy colloidal particles. *Soft Matter*, 8:1785, 2012.

[92] J. M. Kleshchanok, D.and Meijer, A. V. Petukhov, G. Portale, and H. N. W. Lekkerkerker. Sedimentation and depletion attraction directing glass and liquid crystal formation in aqueous platelet/sphere mixtures. *Soft Matter*, 8:191, 2012.

[93] C. S. Dias, N. A. M. Araújo, and M. M. Telo da Gama. Kinetic roughening of aggregates of patchy colloids with strong and weak bonds. *Europhys. Lett.*, 107:56002, 2014.

[94] H. J. Wilson and R. H. Davis. Shear stress of a monolayer of rough spheres. *J. Fluid Mech.*, 452:425–441, 2002.

[95] B. Ilhan, C. Annink, D. V. Nguyen, F. Mugele, I. Siretanu, and M. H. G. Duits. A method for reversible control over nano-roughness of colloidal particles. *Colloid Surface A*, 560: 50 – 58, 2019.

[96] J. M. Nitche and G. K. Batchelor. Break-up of a falling drop containing dispersed particles. *Journal of Fluid Mechanics*, 340:161, 1997.

[97] H. Löwen. Particle-resolved instabilities in colloidal dispersions. *Soft Matter*, 6:3133, 2010.

[98] K. Milinković, J. T. Padding, and M. Dijkstra. Hydrodynamic rayleigh-taylor-like instabilities in sedimenting colloidal mixtures. *Soft Matter*, 7:11177–11186, 2011.

[99] D. Huh, J. H. Bahng, Y. Ling, H. H. Wei, O. D. Kripfgans, J. B. Fowlkes, J. B. Grotberg, and S. Takayama. Gravity-driven microfluidic particle sorting device with hydrodynamic separation amplification. *Anal. Chem.*, 79:1369–1376, 2007.

[100] B. Li, D. Zhou, and Y. Han. Assembly and phase transitions within colloidal crystals. *Nat. Rev. Mat.*, 1:15011, 2016.

[101] M. S. Reddy, R. Vijaya, I. D. Rukhlenko, and M. Premaratne. Spatial and spectral distributions of emission from dye-doped photonic crystals in reflection and transmission geometries. *J. Nanophotonics*, 6:063526–063526, 2012.

[102] N. V. Dziomkina and G. J. Vancso. Colloidal crystal assembly on topologically patterned templates. *Soft Matter*, 1:265–279, 2005.

[103] S. Sacanna and D. J. Pine. Shape-anisotropic colloids: Building blocks for complex assemblies. *Curr. Opin. Colloid In.*, 16:96–105, 2011.

[104] N. M. Silvestre, P. Patricio, M. M. Telo da Gama, A. Pattanaporkratana, C. S. Park, J. E. Maclennan, and N. A. Clark. Modeling dipolar and quadrupolar defect structures generated by chiral islands in freely suspended liquid crystal films. *Phys. Rev. E*, 80: 041708, 2009.

[105] D. Babič, C. Schmitt, and C. Bechinger. Colloids as model systems for problems in statistical physics. *Chaos*, 15:026114, 2005.

[106] H. Löwen. Introduction to colloidal dispersions in external fields. *Eur. Phys. J. Spec. Top.*, 222:2727–2737, 2013.

[107] S. C. Martin, B. B. Laird, R. Roth, and H. Hansen-Goos. Thermodynamics of the hard-disk fluid at a planar hard wall: Generalized scaled-particle theory and monte carlo simulation. *J. Chem. Phys.*, 149:084701, 2018.

[108] S. C. Lin and M. Oettel. Phase diagrams and crystal-fluid surface tensions in additive and nonadditive two-dimensional binary hard-disk mixtures. *Phys. Rev. E*, 98:012608, 2018.

[109] J. K. Percus. Equilibrium state of a classical fluid of hard rods in an external field. *J. Stat. Phys.*, 15:505–511, 1976.

[110] W. Bollmann. *Crystal defects and crystalline interfaces*. Springer Science & Business Media, 2012.

[111] K. Pyka, J. Keller, H. L. Partner, R. Nigmatullin, T. Burgermeister, D. M. Meier, K. Kuhlmann, A. Retzker, M. B. Plenio, W. H. Zurek, A. del Campo, and T. E. Mehlstäubler. Topological defect formation and spontaneous symmetry breaking in ion coulomb crystals. *Nat. Commun.*, 4:2291, 2013.

[112] W. H. Zurek. Causality in condensates: Gray solitons as relics of BEC formation. *Phys. Rev. Lett.*, 102:105702, 2009.

[113] A. del Campo, G. De Chiara, G. Morigi, M. B. Plenio, and A. Retzker. Structural defects in ion chains by quenching the external potential: The inhomogeneous kibble-zurek mechanism. *Phys. Rev. Lett.*, 105:075701, 2010.

[114] I. M. Lifshitz and A. M. Kosevich. The dynamics of a crystal lattice with defects. *Rep. Prog. Phys.*, 29:217, 1966.

[115] D. T. J. Hurle and P. Rudolph. A brief history of defect formation, segregation, faceting, and twinning in melt-grown semiconductors. *J. Cryst. Growth*, 264:550, 2004.

[116] K. Chen, R. Kapadia, A. Harker, S. Desai, J. S. Kang, S. Chuang, M. Tosun, C. M. Sutter-Fella, M. Tsang, Y. Zeng, D. Kiriya, J. Hazra, S. R. Madhvapathy, M. Hettick, Y.-Z. Chen, J. Mastandrea, M. Amani, S. Cabrini, Y.-L. Chueh, J. W. Ager III, Chrzan D. C., and A. Javey. Direct growth of single-crystalline III-V semiconductors on amorphous substrates. *Nat. Commun.*, 7:10502, 2016.

[117] T. Boeck, F. Ringleb, and R. Bansen. Growth of crystalline semiconductor structures on amorphous substrates for photovoltaic applications. *Crystal Res. Technol.*, 52:1600239, 2017.

[118] M. Heyde. Structure and motion of a 2D glass. *Science*, 342:201, 2013.

[119] S. Kulkarni, M. A selective review of the quantification of defect dynamics in growing Czochralski silicon crystals. *Ind. Eng. Chem. Res.*, 44:6246, 2005.

[120] M. J. Kramer, M. I. Mendelev, and R. E. Napolitano. In situ observation of antisite defect formation during crystal growth. *Phys. Rev. Lett.*, 105:245501, 2010.

[121] N. Faleev, N. Sustersic, N. Bhargava, J. Kolodzey, S. Magonov, D. J. Smith, and C. Honsberg. Structural investigations of SiGe epitaxial layers grown by molecular beam epitaxy on Si (001) and Ge (001) substrates: Ii – Transmission electron microscopy and atomic force microscopy. *J. Cryst. Growth*, 365:35, 2013.

[122] S. Wang, A. Robertson, and J. H. Warner. Atomic structure of defects and dopants in 2d layered transition metal dichalcogenides. *Chem. Soc. Rev.*, 47:6764, 2018.

[123] S. Deutschländer, P. Dillmann, G. Maret, and P. Keim. Kibble–zurek mechanism in colloidal monolayers. *Proc. Natl. Acad. Sci. U.S.A.*, 112:6925, 2015.

[124] W. T. M. Irvine, M. J. Bowick, and P. M. Chaikin. Fractionalization of interstitials in curved colloidal crystals. *Nat. Mater.*, 11:948, 2012.

[125] A. T. Pham, R. Seto, J. Schönke, D. Y. Joh, A. Chilkoti, E. Fried, and B. B. Yellen. Crystallization kinetics of binary colloidal monolayers. *Soft Matter*, 12:7735, 2016.

[126] T. Brazda, C. July, and C. Bechinger. Experimental observation of Shapiro-steps in colloidal monolayers driven across time-dependent substrate potentials. *Soft Matter*, 13: 4024, 2017.

[127] C. Bechinger, M. Brunner, and P. Leiderer. Phase behavior of two-dimensional colloidal systems in the presence of periodic light fields. *Phys. Rev. Lett.*, 86:930–933, 2001.

[128] A. Chowdhury, B. J. Ackerson, and N. A. Clark. Laser-induced freezing. *Phys. Rev. Lett.*, 55:833–836, 1985.

[129] G. Volpe, L. Kurz, A. Callegari, G. Volpe, and S. Gigan. Speckle optical tweezers: Micromanipulation with random light fields. *Opt. Express*, 22:18159, 2014.

[130] E. Pinçe, S. K. Velu, A. Callegari, P. Elahi, S. Gigan, G. Volpe, and G. Volpe. Disorder-mediated crowd control in an active matter system. *Nat. Commun.*, 7:10907, 2016.

[131] P. H. Jones, O. M. Maragò, and G. Volpe. *Optical tweezers: Principles and applications*. Cambridge University Press, 2015.

[132] S. H. Behrens and D. G. Grier. Pair interaction of charged colloidal spheres near a charged wall. *Phys. Rev. E*, 64:050401, 2001.

[133] J M Kosterlitz and D J Thouless. Ordering, metastability and phase transitions in two-dimensional systems. *J. Phys. C Solid. State. Phys.*, 6:1181–1203, 1973.

[134] B. I. Halperin and D. R. Nelson. Theory of two-dimensional melting. *Phys. Rev. Lett.*, 41:121–124, 1978.

[135] D. R. Nelson and B. I. Halperin. Dislocation-mediated melting in two dimensions. *Phys. Rev. B*, 19:2457–2484, 1979.

[136] A. P. Young. Melting and the vector Coulomb gas in two dimensions. *Phys. Rev. B*, 19: 1855–1866, 1979.

[137] S. C. Kapfer and W. Krauth. Two-dimensional melting: From liquid-hexatic coexistence to continuous transitions. *Phys. Rev. Lett.*, 114:035702, 2015.

[138] U. Gasser, C. Eisenmann, G. Maret, and P. Keim. Melting of crystals in two dimensions. *Chem. Phys. Chem.*, 11:963–970, 2010.

[139] Y. Bromberg and H. Cao. Generating non-rayleigh speckles with tailored intensity statistics. *Phys. Rev. Lett.*, 112:213904, 2014.

[140] N. Bender, H. Yilmaz, Y. Bromberg, and H. Cao. Customizing speckle intensity statistics. *Optica*, 5:595, 2018.

[141] D. G. Grier. A revolution in optical manipulation. *Nature*, 424:810, 2003.

[142] J. C. Crocker and D. G. Grier. Methods of digital video microscopy for colloidal studies. *J. Colloid Interfac. Sci.*, 179:298, 1996.

[143] A. P. Mosk, A. Lagendijk, G. Lerosey, and M. Fink. Controlling waves in space and time for imaging and focusing in complex media. *Nat. Photon.*, 6:283, 2012.

[144] T. L. Alexander, J. E. Harvey, and A. R. Weeks. Average speckle size as a function of intensity threshold level: comparison of experimental measurements with theory. *Appl. Opt.*, 33:8240–8250, 1994.

[145] H. Lin and P. Yu. Speckle mechanism in holographic optical imaging. *Opt. Express*, 15: 16322–16327, 2007.

[146] J N. Israelachvili. *Intermolecular and Surface Forces*. Academic Press, third edition edition, 2011.

[147] S. Paladugu, A. Callegari, Y. Tuna, L. Barth, S. Dietrich, A. Gambassi, and G. Volpe. Nonadditivity of critical Casimir forces. *Nat. Commun.*, 7:11403, 2016.

[148] L. P. García, J. D. Pérez, G. Volpe, A. V. Arzola, and G. Volpe. High-performance reconstruction of microscopic force fields from brownian trajectories. *Nat. Commun.*, 9: 5166, 2018.

[149] A. Callegari, M. Mijalkov, A. B. Gököz, and G. Volpe. Computational toolbox for optical tweezers in geometrical optics. *J. Opt. Soc. Am. B*, 32:B11, 2015.

Appendix A

Density functional theory of hard rods

Figure A.1 shows the evolution of the densities in a one dimensional system using the free energy functional of Eq. 5.11. The left panel is the initial configuration, both densities are equal and we introduced a sinusoidal perturbation to the uniform density to decrease the computation time. The parameter r in the figures is the distance to the center of the domain. The center panel shows an increase of the density of strong particles at small r while the density of weak ones decreases and develops a peak at the edge of the central strong cluster. In the right panel we show the equilibrium state. The system is completely segregated and the density curves display the ripples that suggest layering as what remains of crystallization in 1D.

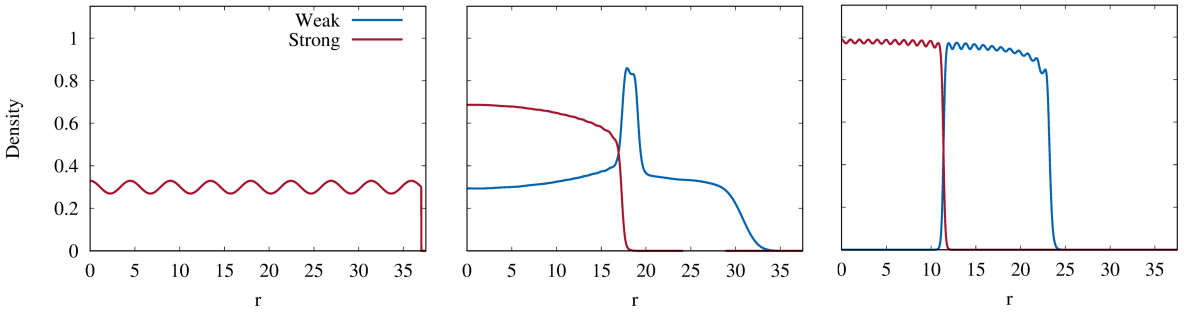

FIGURE A.1: Evolution of the densities of strong and weak particles computed with DDFT in 1D. The parameter r is the distance to the center of the system.

Note that this method does not capture the kinetically trapped states predicted by the Brownian simulations even though we are integrating the density equations in time.

Appendix B

Details of the experiments

We describe here the details of the experiments preformed by our collaborators along our theoretical work described in chapter 6 [38].

B.1 Sample preparation

Diluted aqueous stock solutions of polystyrene and silica colloidal spheres (Microparticles GmbH, diameter $d_{\mathrm{PS}} = 6.24 \pm 0.22\,\mu$m and $d_{\mathrm{Si}} = 6.73 \pm 0.22\,\mu$m, respectively) were used to prepare binary solutions with different molar fractions of polystyrene particles from $\chi = 0$ to $\chi = 1$. The total density of particles was kept constant at $1.4 \cdot 10^7\,\mathrm{ml}^{-1}$. These colloidal solutions were confined in a homemade sample chamber (internal thickness $200\,\mu$m), built between a bottom glass slide (made hydrophilic by treatment in a 0.25 M NaOH solution) and a top flat-terminated fibre coupler (Thorlabs, SM1SMA) held apart by two layers of a thermoplastic spacer, which at the same time was also used for sealing the chamber. The fibre coupler was used to connect the output end of a multimode optical fiber (core diameter $105\,\mu$m, NA $= 0.22$, length 51 m) . See also Fig. B.1.

B.2 Experimental setup

A homemade inverted optical microscope setup was used for carrying out the experimental investigations of structural defects in colloidal crystals formed under random optical potentials, as schematically shown in Fig. B.1 [130]. An image of the sample with colloidal particles was projected by a microscope objective (Nikon Plan Fluorite Imaging Objective, $20\times$, NA $= 0.5$, WD $= 2.1$ mm) onto a monochrome charge-coupled device (CCD) camera with an acquisition

rate between 1 and 8 frames per second (fps). The incoherent illumination was provided by a LED lamp at $\lambda = 625\,\text{nm}$ coupled into the optical fiber using a dichroic mirror (Thorlabs, DMLP650). The particles were tracked by digital video microscopy [142].

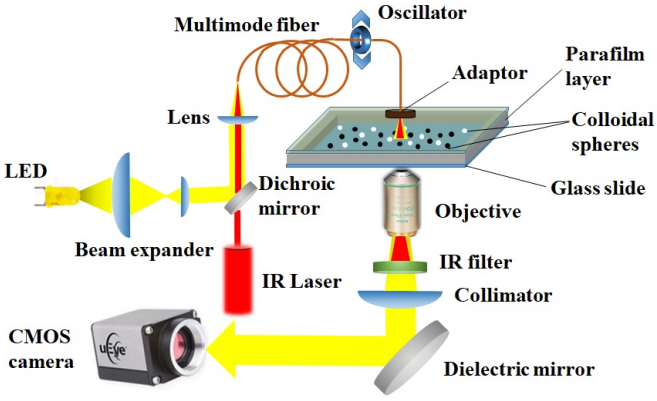

FIGURE B.1: Schematic representation of the experimental setup and sample chamber.

The static speckle light pattern with a Gaussian envelope was generated by focusing a laser beam (wavelength $\lambda = 976\,\text{nm}$, output power $P = 90\,\text{mW}$) into a multimode optical fiber using a plano-convex lens (focal distance $f = 25.4\,\text{mm}$). The output speckle pattern is the result of the multipath interference of the optical waves carrying random phases within the multimode optical fiber [129, 130, 143]. The length of the optical path between the fiber tip and the imaging plane where the colloidal particles lay (i.e., the bottom of the sample chamber) determines the final speckle grain size. The typical duration of an experiment is about 90 minutes.

As proposed in Ref. [144], to characterize the strength and correlation length of the optically generated random field, we first identify the "bright spots"and then fit a Gaussian to each spot, using the code in Ref. [145].

The smooth optical potential was obtained by the speckle suppression using a high frequency mechanical oscillator connected to the stretched interval of the optical fiber. The vibrational frequency was adjusted with DC voltage up to 12000 rpm.

B.3 Particle heights in the experiments

To calculate the gravitational height of each colloidal species, we need to account for the balance of four different forces: weight, buoyancy, optical forces, and electrostatic forces. The net force should vanish, so the electrostatic repulsive interaction with the glass substrate (pre-cleaned with NaOH to make it hydrophilic) should balance the sum of weight, buoyancy, and optical forces. We express the electrostatic force as [146]

$$F_{es}(d) = -\nabla U_{es}(d) = \frac{k_B T}{l_D} \exp\left(-\frac{d - l_{es}}{l_D}\right), \tag{B.1}$$

where d is the distance between the surface of the particle and the substrate, l_D is the Debye length, and l_{es} is a characteristic length. In our case we can assume that the value of l_D is in the range 30 to 60 nm, as estimated from an experiment with silica particles in distilled water. Thus, the pre-factor $k_B T / l_D \approx 0.14 - 0.07$ pN. We also assume that the value of $l_{es} \approx 100 - 200$ nm, slightly bigger than the value found for water-lutidine for silica (90 nm) [147], as distilled water is more polar.

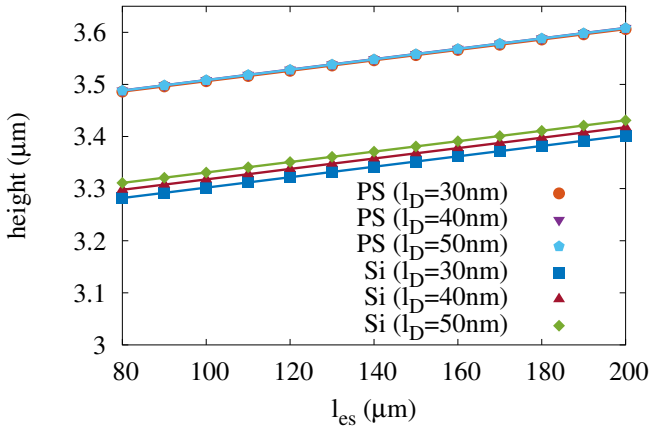

FIGURE B.2: Gravitational height of both species calculated with different parameters from Eq. B.1.

	Characteristics of PS particles	Characteristics of Si particles
Surface charge	anionic	anionic
Refractive index	1.59	1.4
Density	1.05 g/cm^3	1.85 g/cm^3
Diameter	6.24 μm	6.73 μm
F optical (ray optics)	35×10^{-3} pN	9×10^{-3} pN

TABLE B.1: Parameters of the particles in the experiments.

The parameters for the two particle species are summarized in Table B.1. Figure B.2 shows the estimated gravitational height as a function of l_{es}, in the range $80 - 220$ nm, for four different values of l_D, considering a water refractive index of 1.33 and density of 1.00 g/cm^3. In all cases, we find that the gravitational heights for both particle species differ by less than 3% of the particle diameter, suggesting that bidispersity effects resulting from differences in gravitational height are negligible. With such a small difference in gravitational height is very

unlikely that one particle would go on top of another and the system can be considered purely two dimensional.

B.4 Measurement of the optical strength in the experiments

The analysis was performed only to the particle trajectories that displayed in the initial part of the experimental acquisition an "accumulation point", i.e., each particle in its trajectory spend a few minutes by staying in approximately the same position, without being stuck. Those points were selected manually and a quantitative analysis was performed with the FORMA method [148] which is a method based on a maximum-likelihood-estimator analysis, and it is able to estimates accurately the conservative and non-conservative components of a force field acting on a Brownian particle from the analysis of its displacements.

B.5 Comment on particle bidispersity

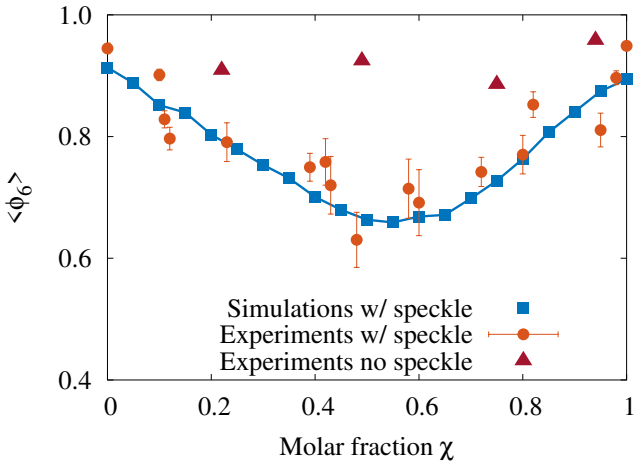

FIGURE B.3: Six-fold bond order parameter $\langle\phi_6\rangle$ as a function of the molar fraction χ obtained experimentally with the particles subject only to a Gaussian envelope (triangles) and with the speckle for the experiments (circles) and the simulations (squares).

We preformed a set of experiments with binary solutions that were carried out to determine if bidispersity influences the measurements of the bond order parameter. We modified the setup by attaching a mechanical oscillator to a part of the multimode fiber. The vibrational frequency could be adjusted with DC voltage and increased up to 12000 rpm. By turning the oscillator on, we were able to generate a smooth speckle pattern and create an optical field where the statistical

properties of the speckle are averaged out. This way, we were able to create a smoothed pattern. The bond order parameter depends strongly on the presence of strong particles under the speckle field, as seen in Fig.2. However, with a smooth potential we observed the formation of a crystal-like structures with bond order parameter in the range $0.9-0.97$, for all χ values (see Fig. B.3). As such, we can confidently conclude that bidispersity does not affect our measurements.

B.6 Strength of the optical potential acting on the particles

Importantly, both in simulations and experiments, we are operating in the regime in which the optical forces at the deepest local minima of the speckle potential are strong enough to trap the strong particles, but not the weak ones. To verify this, experimentally, the trajectories of individual particles were analyzed in the dilute regime (estimated using the FORMA method [148], see details on how this data was obtained from the experiments in appendix B.4).

The stiffness constants associated with the interactions with the optical potential obtained for Silica particles (weak) and PS particles (strong) are $k_{\text{weak}} = 5fN/\mu m$ and $k_{\text{strong}} = 11fN/\mu m$, respectively. This result suggests that the stiffness of the strong particles in the minima is approximately two times higher than that of the weak particles in the experiments.

We also measured the average modulus of the force acting on each particle due to the speckle, over the entire domain. It was calculated using geometrical optics in the experimental speckle profile [149] $F_{\text{weak}} = (9.36 \pm 4.75)fN$ and $F_{\text{strong}} = (18.87 \pm 9.63)fN$, and in the simulations, $F_{\text{weak}} = (5.81 \pm 4.21)fN$ and $F_{\text{strong}} = (11.61 \pm 8.44)fN$. Thus, we obtain the same order of magnitude of the forces and, more importantly, a similar $2\times$ ratio between the average forces for strong and weak particles.